

Master thesis

Designing of the cavity for muonium HFS at J-PARC/MLF

J-PARC/MLF でのミュオニウム超微細構造測定に向けたキャビティ製作

東京大学大学院総合文化研究科
広域科学専攻相関基礎科学系

31-106919

田中 香津生

March 16, 2012

Abstract

Measurement of the ground state hyperfine structure of muonium (muonium HFS) is planned at J-PARC/MLF. Muonium is a hydrogen-like bound state of leptons, and its HFS is a good probe for testing QED theory. The muon mass m_μ and magnetic moment μ_μ which are fundamental constants of muon are determined from the muonium HFS experiment at LAMPF. Those constants are also required in the new measurement of anomalous magnetic moment at the J-PARC. Accuracy one digit higher than that of the latest experiment is expected mainly because of high intensity beam line at J-PARC. We aim to start this experiment within a few years.

Transition frequency of muonium HFS is determined indirectly by Zeeman Effect in strong field. By driving the transitions with an applied microwave magnetic field perpendicular to the static magnetic field, the muon spin could be flipped and the angular distribution of high momentum positrons changed from predominantly upstream to downstream with a respect to the beam direction.

In this experiment, the structure of a gas chamber and a cavity play important roles for the precise measurement. A purity and a pressure of the Kr gas, a stability of the RF power, an uniformity of the resonance magnetic field and a temperature in the cavity cause to add a uncertainty to the result of the measurement.

Since the transition frequencies of muonium measured in a gas vary with the gas pressure, the transition frequencies in vacuum are determined by extrapolating the measured frequencies at several different gas pressures. The axial length of the cavity is long to stop muons in the cavity at a low gas pressure. Also the cavity has a stable RF system and a mechanism of tuning resonance frequencies in to the transition frequencies. Measurements of frequency characteristics of the cavity and performance evaluations of the mechanism of tuning resonance frequencies are held at RIKEN Nishina Center.

Contents

1	Introduction	15
1.1	Measurement HFS transition of Hydrogen-like atoms	15
1.1.1	HFS transition of hydrogen	15
1.1.2	HFS transition of positronium	17
1.1.3	HFS transition of muonium	17
1.2	Experimental background	18
1.3	Theoretical background	20
1.4	Motivation	21
1.4.1	Determination of fundamental constants of the muon	21
1.4.2	Testing QED theory	22
1.4.3	$g-2$ experiment	24
1.4.4	Testing CPT and Lorentz invariance	26
2	Experimental strategy	28
2.1	How to produce muon	28
2.2	How to produce muonium	29
2.2.1	Beam foil	29
2.2.2	Silica powder	29
2.2.3	Gas target	29
2.3	How to measure muonium HFS	30
2.4	Experimental apparatus and procedure	34
2.4.1	General overview	34
2.4.2	Magnet	34
2.4.3	Positron Detector	36

2.4.4	Profile Monitor	40
2.5	Reduce of uncertainties	40
2.5.1	statistical uncertainty	41
2.5.2	Uncertainty of the magnetic field	41
2.5.3	Other uncertainties	43
3	Designing of the cavity and the gas chamber	45
3.1	Cavity	45
3.1.1	Resonance modes	46
3.1.2	Diameter of the cavity	48
3.1.3	Tuning bar	48
3.1.4	Axial length	60
3.1.5	Foils of the cavity	67
3.1.6	Summary of designing the cavity	67
3.2	RF transport	70
3.2.1	Coaxial pipe	70
3.2.2	Feedthrough	73
3.2.3	Antenna	73
3.2.4	RF source	73
3.2.5	Network analyzer	73
3.3	Temperature control	73
3.3.1	Temperature shifts in the transition frequencies	73
3.3.2	Thermometer	74
3.3.3	Cooling tube	74
3.3.4	Control of room temperature	74
3.4	NMR probe	74
3.5	Gas chamber	74
3.5.1	Purity	76
4	Measurement	78
4.1	RF system for the measurement	78
4.1.1	Network Analyzer	78

4.1.2	RF ports	84
4.2	Frequency character of the cavity	85
4.3	Performance evaluation of tuning bars	86
4.3.1	Q factor of the cavity with tuning bars	86
4.3.2	Relationship between displacement of tuning bars and resonance frequencies	91
4.3.3	Difference between several types of tuning bars	91
5	Discussion	99
5.1	Improvement of the uniformity of RF fields	99
5.1.1	Widen inner diameter of the cavity	99
5.1.2	Optimization of the shape of tuning bars	102
5.2	Schedule of development of the cavity	103
5.3	Schedule of muonium HFS experiment	103
A	Drawings	105
B	Muon beamline	110
B.1	How to provide a muon beam	110
B.2	Muon beam lines	112
C	RF fields of the TM₁₁₀ mode and the TM₂₁₀ mode	115
D	Evaluation of a input RF power	116

List of Figures

1.1	Developments of spectroscopy of hydrogen atom. Energy splitting between the red lines is ground state hyperfine splitting.	16
1.2	(a) Values of muonium HFS at several past experiments since 1970. A blue area is a range of the theoretical value from Equation 1.6. (b) An accuracy of those values. The accuracy of the muonium HFS measurement have been exponentially increase.	19
1.3	Values of fine structure constant publication of the CODATA 2006 [1]	23
1.4	A result of $g-2$ measurement at BNL. The significance of the deviation is 2.6 standard deviations from the existing theory [2].	25
1.5	A conceptual drawing of the experimental setup of the $g-2$ experiment.	26
1.6	Two years of data on ν_{12} and ν_{34} at the LAMPF experiment are shown binned versus sidereal time and fit for a possible sinusoidal variation. The amplitudes are consistent with zero [3].	27
2.1	A comparison of the methods of muonium production. Gas stop is the most suitable method for the muonium HFS experiment from the aspect of a production rate and a rate of polarization.	30
2.2	Energy levels of the muonium in ground state as a function of external magnetic field. F is the quantum number of the total angular momentum and $M_F = M_s + M_I$	33
2.3	A schematic overview of the experimental setup of the muonium HFS experiment.	35

2.4	An isometric view and a cross-sectional drawing of the magnet. The magnet consist of main coils and shim coils. Error fields are corrected by shim coils and iron shims. A high field uniformity better than 1 ppm with in the spheroid region of 20 cm in diameter and 30 cm in length is necessary accurate.	36
2.5	A spectrum of decay positron momentum for events within $0, 70 < \cos \theta < 0.84$ measured at TWIST [4].	38
2.6	An angular distribution of decay positron at several y values expressed in polar coordinates. The direction of muon magnetic moment is rightward.	39
2.7	A schematic view of the FBPM and the TBPM. The FBPM is using for taking 2-dimensional muon distribution during the experiment. The TBPM is using for taking 3-dimensional muon distribution in the gas chamber before taking data.	41
2.8	Uncertainties of LAMPF experiments and improvements of each of them at our experiment. upper bar is represented $\delta(\mu_\mu/\mu_p)$ obtained by sweeping the magnetic field and another one is by sweeping the microwave frequency.	42
2.9	A cross-sectional image of uniformity of the magnetic field in the cavity. z is a axial direction of the cavity and r is a radial direction. A field homogeneity of our new magnet under designing is less than 0.5 ppm in simulation using OPERA [5].	44
3.1	A relation between a ratio of the ν_{12} and the nu_{34} transition frequencies and a ratio of resonance frequencies of the TM110 mode and the TM210 mode. Since the ratio of the TM110 mode and the TM210 mode is constant at a cylindrical cavity, there only two solutions to be tuned in to both transitions.	47
3.2	RF fields of the TM110 mode and the TM210 mode. The red arrow shows the electric field vector and the green one shows the magnetic field vector.	48
3.3	A cross-sectional view of the cavity with the TM110 mode and the TM210 mode. The red arrows indicate the electric field and the green arrows indicate the magnetic field. The positions of the input ports for the TM110 (TM210) mode are chosen not to couple the TM210 (TM110) mode. The position of the output port is chosen couple to both modes weakly.	49

3.4	An electric field difference between using a tuning bar made of a conductive material and a dielectric material. The conductive tuning bar affects electric field as shrink a diameter of the cavity. On the other hand, The dielectric tuning bar affect as widen it by absorbing RF power.	51
3.5	Electric fields of the TM110 mode using a alumina and a copper tuning bars. Using the copper tuning bars, strong resonance between the tuning bars and the the cavity face is induced. On the other hand, the uniformity of the RF field is better with the alumina tuning bars.	52
3.6	A schematic drawing of the tuning bar.	55
3.7	A diagram of a positioner system. ANC-350 has three channels to operate the positioners. It transmits sawtooth waves to each positioner and displace their stages in proportion to amplitude of waves. Precise displacement is achieved by feedback from a positioner sensors.	56
3.8	A photograph of piezo positioner.	57
3.9	A photograph of piezo controller.	57
3.10	Degenerated modes of the TM110. The left side (TM110-1) of resonance mode is affected by tuning bar for TM110 stronger than the right side (TM110-2). Then this mode is appropriate to using for the resonance frequency sweep. . .	58
3.11	Degenerated modes of TM210. The left side (TM210-1) of resonance mode is affected by tuning bar for TM110 stronger than the right side (TM210-2). Then this mode is appropriate to using resonance frequency sweep.	58
3.12	A relation between resonance frequency of the TM110 mode and the displacement of the tuning bar. This is a result of the simulation using a alumina tuning bars (20 mm × 200 mm × 2.5 mm). Origin points of tuning bars are defined as 5 mm far from the cavity face. The TM110 mode is splitted into two degenerated modes. The red point is the TM110-1 mode and the blue point is the TM110-2 mode. The TM110-1 mode is more sensitive to the displacement.	59
3.13	Muons pass through a profile monitor, a moderator, a foil of chamber and a foil of the cavity and stop in the cavity by Kr gas. Those materials must be thin enough to enable muon passing through.	61

3.14	A relation between the Kr gas pressure and (a) ν_{12} transition frequency and (b) ν_{34} transition frequency at LAMPF experiment. They were measured at 0.7 atm and 1.8 atm and extrapolate to obtain values at 0 atm. To ensure more accurate extrapolation, measurement at lower pressure is needed [6].	62
3.15	A muon stopping distribution in 0.3 atm Kr gas. Trajectories of 100000 muons were simulated by a Monte Carlo simulation program SRIM. The cavity axial length is 159.73 mm designed for the latest experiment at LAMPF. To stop muons in a narrow region, the moderator used had to be thick.	63
3.16	A muon stopping distribution in 0.3 atm Kr gas. The cavity axial length is 304 mm designed for a new experiment at J-PARC. The muon stopping distribution is brought within the cavity.	64
3.17	Other resonance modes around the mode TM110 and the TM210 mode. Resonance frequencies of the mode TM110 and the TM210 mode does not depend on the cavity axial length. On the other hand, resonance frequencies of many other modes which has nodes in axial direction decrease by axial length of the cavity. In case of the cavity whose axial length is 304 mm, many modes are close to the TM110 mode and the TM210 mode.	65
3.18	Resonance modes near the TM110 modes in which case axial length is 300 mm. A TM012 mode is located between splitted the TM110 modes which is undesirable.	66
3.19	Resonance modes near the TM110 modes in which case axial length is 302 mm. Resonance frequency of the TM012 mode is lower than that of a 300 mm cavity. Resonance frequencies of the TM110 modes are not changed because they are independent of cavity length.	66
3.20	Resonance modes near the TM110 modes in which case axial length is 304 mm. Now the TM012 mode is far from the TM110 modes enough to be distinguished.	67
3.21	How to stretch foils of the cavity. At first, foils are temporary jointed between a F2 and a F3 flanges. Then stretch them again and mount to the cavity by a F1 flange.	68

3.22	An isometric view of the cavity. There are three RF ports and two ports for tuning bars. A cooling tube and a support for being strapped to the gas chamber will be installed.	69
3.23	A RF system for applied RF to the cavity and monitoring RF power in the cavity.	71
3.24	A conceptual view of a RF port. the RF power is delivered by coaxial pipes. Kr gas is sealed by feedthrough put between coaxial pipes and antennas. All parts are made of a copper.	72
3.25	A cross-sectional view of a coaxial pipe (WX-20D) and a waveguide (WRI-22). The coaxial pipe is compact compared to the waveguide.	72
3.26	Surface currents of the cavity resonated (a) the TM110 and (b) the TM210 modes. Ideally the surface current is independent to the axial direction; however, there is a nonuniformity of the RF field mainly caused by the tuning bars.	75
3.27	A Conceptual design of a gas chamber. It is made of a aluminum and has ports for RF transports and for tuning bars. A gas handling system is under designing.	77
4.1	A process of TOSM calibration and the measurement of S-parameter using the network analyzer.	83
4.2	A photograph of RF antennas for the measurement.	85
4.3	(a) S_{11} near the TM110 modes by the measurement. The red arrows show resonance frequencies of each mode. (b) S_{21} by the measurement.	87
4.4	A Closeup of Figure 4.3 (a). The red arrows show resonance frequencies of the TM110 modes.	88
4.5	(a) S_{11} near the TM210 modes by the measurement. The red arrows show resonance frequencies of each mode. (b) S_{21} by the measurement.	89
4.6	A photograph of inner view of the cavity. The RF antennas and the tuning bars are installed.	90

4.7	A TM110 resonance frequency sweep by the tuning bar for TM110. Square markers are the values obtained in the measurement and triangle markers are the values obtained in the simulation. Red one is a that of the TM110-1 mode and blue one is a that of the TM110-2 mode.	92
4.8	A TM210 resonance frequency sweep by the tuning bar for TM210. Square markers are the values obtained in the measurement and triangle markers are the values obtained in the simulation. Red one is a that of TM210-1 and blue one is a that of TM210-2.	93
4.9	A TM110 resonance frequency sweep by the tuning bar for TM210. Red one is a that of TM210-1 and blue one is a that of TM210-2.	94
4.10	Three tuning bars are used for this measurement. The sweep range of tuning bar3 is shorter than other bars and the line shape of tuning bar2 is parallel to the that of tuning bar1.	95
4.11	A difference of sweep range of the TM110 mode between several tuningbars. .	96
4.12	A difference of sweep range of TM210 mode between several tuningbars. the parallel relationship of the line shape of tuning bar1 and tuning bar2 is not kept.	97
4.13	A cross-sectional view of the electric fields of the TM210 mode. The RF field is rotates on axis of the cavity by inserting the tuning bar.	98
5.1	A relation between the diameter of the cavity and the resonance frequency of the TM110 mode by simulation. The red line shows a resonance frequency without tuning bars and the blue line shows a with tuning bars put are placed at origin. The green line is the ν_{34} transition frequency.	100
5.2	A relation between the diameter of the cavity and the resonance frequency of the TM210 mode by simulation. The red line shows a resonance frequency without tuning bars and the blue line shows a with tuning bars are placed at origin. The green line is the ν_{34} transition frequency.	101
5.3	A difference of RF field of TM210 mode between tuning bar1 and tuning bar2.	102
5.4	A schedule of a preparation of this experiment. we can start this experiment until the end of 2012.	104
A.1	A drawing of the cavity.	106

LIST OF FIGURES

A.2	A drawing of the tuning bar.	107
A.3	A drawing of the tuning bar support.	107
A.4	A drawing of the tuning bar support port.	108
A.5	A drawing of the flange of tuning bar support port.	108
A.6	A drawing of the SMA connector.	109
A.7	A drawing of the SMA support.	109
B.1	A drawing of a overview of facilities at J-PARC and muon beamline at MLF. MLF has a four muon beamlines including under constructing.	111
B.2	Schemes of providing muons. Pions produced at the carbon target which have some energy distribution guided to a large superconducting solenoid magnet and decay into muons in the magnet (Decay muon). Collect muons which is produced by pions stopped near the surface of the carbon target (Surface muon). ultra slow muons ($0 \sim 30$ KeV) are produced by a ionization of muonium.	113
D.1	A relation between signal ratio of microwaves on to off and amplitude of RF magnetic field. The red line represents that of ν_{12} and the blue line represents that of ν_{34}	117

List of Tables

1.1	Comparison of muonium HFS measurements.	18
1.2	Theoretical calculation of muonium HFS [7].The biggest source of calculation of the Fermi energy (E_F) is mainly limited by the knowledge of the muon magnetic moment or the muon mass in proper units (see the number in the first bracket).To determine the muon magnetic moment and muon mass is essentially the same as the g factor of a free muon is known well enough. A smaller uncertainty in determination of the Fermi energy is due to the fine structure constant (see the number in the second bracket). Major uncertainties are E_F limited by the knowledge of the muon magnetic moment or the muon mass and QED4 have not yet been included either into a non-recoil term or into a recoil term.	21
2.1	Threshold energies for muonium formation [8] and the pressure-independent muonium fractions f_{Mu} [9].	31
2.2	Spec of muon beamline.	43
3.1	Characteristics of materials for the tuning bar.	54
3.2	Spec of ANPz101eXT12/RES	57
3.3	Summary of the dimension of the cavity.	70
3.4	Muonium (M)-molecule cross sections [10, 11].	76
4.1	Q factor of the TM110 mode. Loss of Q is caused by surface current at the cavity face and loss tangent of tuning bar.	82
4.2	Q factor of the TM210 mode. Loss of Q is caused by surface current at the cavity face and loss tangent of tuning bar.	82

LIST OF TABLES

4.3 Comparison of Q factor between in the measurmeent and in the simulation. .	86
B.1 Spec of MLF muon beamline	114

Chapter 1

Introduction

Spectroscopy of hydrogen-like atom has played a great role in scientific developments since the birth of quantum physics. Bohr model of atoms was constructed by from spectroscopic data of hydrogen. In a similar way, current quantum mechanics is based on spectroscopy of hydrogen (e.g. formulation of quantum mechanics by Schrödinger, explaining fine structure by relativistic quantum mechanics and explaining lamb shift by QED). Recent technology upgrades enable all the higher precision spectroscopy. For instance, the accuracy of spectroscopy of the 1s-2s transition in hydrogen is 0.0042 ppt [12] and that of the transition of ground state hyperfine structure (HFS) is 0.6 ppt [13, 14].

1.1 Measurement HFS transition of Hydrogen-like atoms

Hyperfine structure is induced by the interaction between the magnetic moment accompanying the nucleus and the electron spin. Figure 1.1 shows the developments of atomic energy levels induced by different interactions. In this section, comparing of the current measured values and the theoretical calculations of HFS interval of the grand state: hydrogen (see Section 1.1.1), positronium (see Section 1.1.2), muonium (see Section 1.1.3) are described.

1.1.1 HFS transition of hydrogen

The latest result of spectroscopy of ground state HFS transition of hydrogen is

$$\Delta HFS_{\text{H}}^{\text{ex}} = 1.4204057517667(9) \text{ GHz (0.6ppt) [14].} \quad (1.1)$$

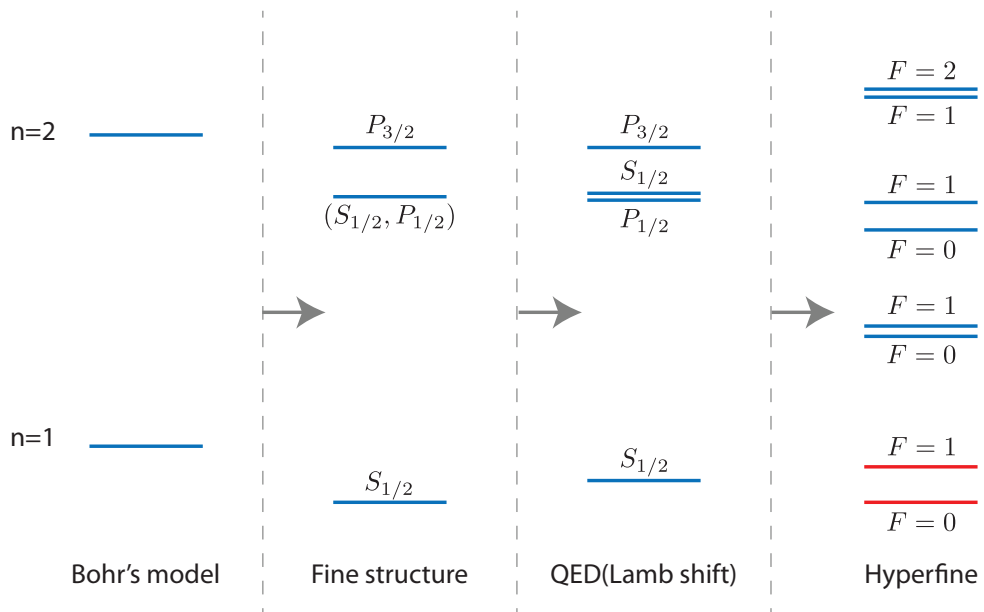


Figure 1.1: Developments of spectroscopy of hydrogen atom. Energy splitting between the red lines is ground state hyperfine splitting.

Theoretical calculation predicts as high as 560 ppb like

$$\Delta HFS_{\text{H}}^{\text{th}} = 1.4204031(8) \text{ GHz (560ppb) [15].} \quad (1.2)$$

Thus the accuracy of the theoretical calculation is far from that of experimental result. The main reason comes from the proton internal structure. Precise test of QED theory using such a structured particle has a difficulty.

1.1.2 HFS transition of positronium

Another example of hydrogen-like atom is positronium. Positronium is a bound state of electron e^- and positron e^+ . Positronium is formed by leptons only like muonium, and the uncertainty of calculation is smaller than hydrogen. The latest value of positronium HFS transition evaluated from the results of two groups is

$$\Delta HFS_{\text{Ps}}^{\text{ex}} = 203.38865(67) \text{ GHz (3.3ppm) [16].} \quad (1.3)$$

The value of theoretical calculation is

$$\Delta HFS_{\text{Ps}}^{\text{th}} = 203.39169(41) \text{ GHz (2.0ppm) [17].} \quad (1.4)$$

The value of theoretical calculation has 3σ deviation from the experimental result. As a matter of course, there are some possibilities of problems of calculation or common systematic errors in the past experiments. However the deviation could be due to new physics beyond Standard Model such as unknown particles. The precise measurement of positronium is underway by Asai laboratory of University of Tokyo.

1.1.3 HFS transition of muonium

Ground state hyperfine transition of muonium is also studied many times in the past. Muonium is a bound state of positive muon μ^+ and electron e^- , it is also a leptonic system as positronium. The latest result by LAMPF is

$$\Delta HFS_{\text{M}}^{\text{ex}} = 4.463302765(53) \text{ GHz (12ppb) [18].} \quad (1.5)$$

The latest theoretical calculation is

$$\Delta HFS_{\text{M}}^{\text{th}} = 4.46330288(55) \text{ GHz (120ppb) [19],} \quad (1.6)$$

which are consistent with each other at the accuracy level of ppm. Since muonium is a pure leptonic atom, the value of muonium HFS transition is able to be calculated with great precision from QED (see Equation 1.6), unlike the case of hydrogen (see Equation 1.2). Moreover, the accuracy of theoretical calculation of muonium HFS will be improved by higher-order QED calculation (see Section 1.3).

1.2 Experimental background

Table 1.1 and Figure 1.2 show previous experimental values. These values are consistent with theoretical calculation nevertheless, more precise measurement and calculation are required for testing QED theory and there are some other motivations described in Section 1.4. There is no experiment since 1999, however, highest intensity pulsed muon beam provided by J-PARC/MLF would enable more precise measurement. Possible improvement of accuracy in this experiment will be discussed in Section 2.5.

Time	Group	$\Delta\nu$	ppm	Ref
1961	Yale-Nevis	5500^{+2900}_{-1500} MHz		[20, 21]
1962	Yale-Nevis	4 461.3(2.0) MHz	450	[22, 23]
1964	Yale-Nevis	4 463.24(12) MHz	27	[24, 25]
1966	Yale-Nevis	4 463.18(12) MHz	27	[26]
1969	Yale-Nevis	4 463.26(4) MHz	9.0	[27]
1969	Chicago	4 463.317(21) MHz	4.7	[23, 28]
1970	Chicago	4 463.302 2(89) MHz	2.0	[29]
1971	Yales-Nevis	4 463.308(11) MHz	2.5	[30]
1971	Chicago	4 463 301.2(23) KHz	0.5	[31]
1973	Chicago-SREL	4 463 304.0(1.8) KHz	0.4	[32]
1975	Yale-Heidelberg-LAMPF	4 463 302.2(1.4) KHz	0.3	[33]
1977	Yale-Heidelberg-LAMPF	4 463 302.35(52) KHz	0.12	[34, 35]
1982	Yale-Heidelberg-LAMPF	4 463 302.88(16) KHz	0.036	[36]
1999	Yale-Heidelberg-LAMPF	4 463 302.765(53) KHz	0.012	[18]

Table 1.1: Comparison of muonium HFS measurements.

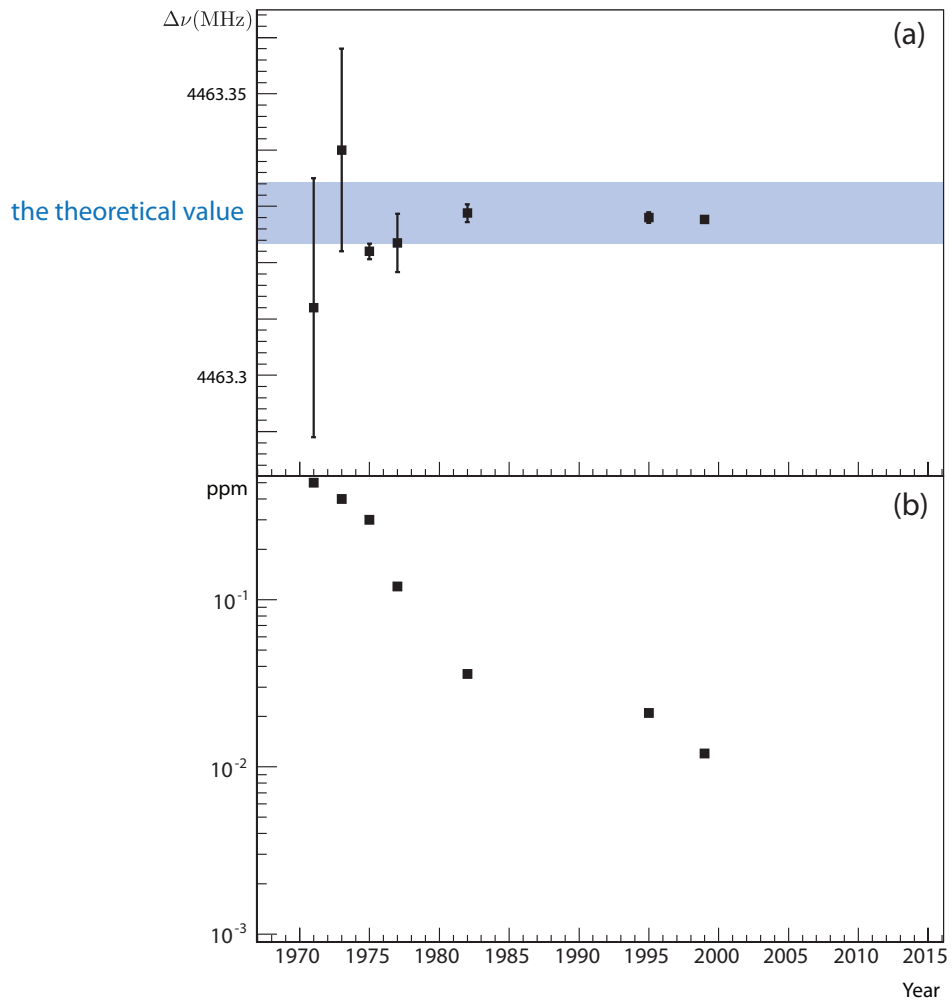


Figure 1.2: (a) Values of muonium HFS at several past experiments since 1970. A blue area is a range of the theoretical value from Equation 1.6. (b) An accuracy of those values. The accuracy of the muonium HFS measurement have been exponentially increase.

1.3 Theoretical background

Following QED theory, ground state hyperfine splitting of muonium is able to be disintegrated into three,

$$\Delta\nu_{HFS} = E_F(1 + \epsilon_{QED}) + \Delta\nu_{strong} + \Delta\nu_{weak}. \quad (1.7)$$

where E_F is Fermi energy given by

$$E_F = \frac{16}{3}(Z\alpha)^2 R_\infty \frac{\mu_\mu}{\mu_B} \left(1 + \frac{m_e}{m_\mu}\right)^{-3}. \quad (1.8)$$

Table 1.2 summarizes fractional contributions to a muonium HFS. QED_i corresponds to i th-order correction of QED calculation. The biggest theoretical uncertainty arises from calculation of the Fermi energy, where the accuracy of the muon magnetic moment and muon mass play theoretical role.

Two fractional contributions beyond QED theory are due to weak and strong interaction. The leading term of weak interaction is induced by the neutral currents given by a Z-boson exchange. The contribution is expressed as [37, 7]

$$\Delta\nu_{weak} = \frac{2G_F}{\sqrt{2}} \frac{(Z\alpha)^3}{\pi n^3} m_r^3 \approx -0.067 \text{ KHz}. \quad (1.9)$$

where G_F is the Fermi constant of the weak interaction. Second largest contributions of weak interaction are 1 % of the leading contribution (see Equation 1.9) and thus negligible [38].

The leading term of hadronic contribution is presented in the form [39, 7]

$$\Delta\nu_{had--vp} = -\frac{Z}{2\pi^3} \frac{m}{M} \nu_F \int_{4m_\pi^2}^{\infty} ds \sigma(s) H(s) = 0.233(3) \text{ KHz}. \quad (1.10)$$

where Z is the nuclear charge.

The problem of the theoretical accuracy of QED effects doesn't neglectible. QED contributions is able to be divided into three parts,

$$\Delta\nu_{QED} = \Delta\nu_{\alpha_e} + \Delta\nu(QED3) + \Delta\nu(QED4). \quad (1.11)$$

The first term arises due to the electron anomalous magnetic moment α_e which is the experimental value [40]. The next term ν_{QED3} includes third order of bound-state QED effect known with good accuracy. However, the fourth-order collections (ν_{QED4}) have large uncertainty because they have not included either a non-recoil term or a recoil term.

Term	Fractional contribution	ΔE (kHz)
E_F	1.000000000	4459031.88(50)(3)
α_e	0.001159652	5170.925(1)
QED2	-0.000195815	-873.145
QED3	-0.000005923	-26.411
QED4	-0.000000123(49)	-0.548(218)
Hadronic	0.000000054(1)	0.241(4)
Weak	-0.000000015	-0.067
Total	1.000957830(49)	4463302.88(55)

Table 1.2: Theoretical calculation of muonium HFS [7]. The biggest source of calculation of the Fermi energy (E_F) is mainly limited by the knowledge of the muon magnetic moment or the muon mass in proper units (see the number in the first bracket). To determine the muon magnetic moment and muon mass is essentially the same as the g factor of a free muon is known well enough. A smaller uncertainty in determination of the Fermi energy is due to the fine structure constant (see the number in the second bracket). Major uncertainties are E_F limited by the knowledge of the muon magnetic moment or the muon mass and QED4 have not yet been included either into a non-recoil term or into a recoil term.

1.4 Motivation

1.4.1 Determination of fundamental constants of the muon

The magnetic moment and mass of muon are fundamental constants of muon. The muon-proton magnetic moment ratio $\frac{\mu_\mu}{\mu_p}$ is obtained by measurement of muonium HFS as

$$\frac{\mu_\mu}{\mu_p} = \frac{\Delta\nu_{\text{Mu}}^2 - \nu^2 (f_p + 2s_e f_p \nu_{f_p})}{4s_e f_p^2 - 2f_p \nu (f_p)} \left(\frac{g_\mu(\text{Mu})}{g_\mu} \right)^{-1}, \quad (1.12)$$

where $\Delta\nu_{\text{Mu}}$ and ν_{f_p} are the sum and difference of two measured transition frequencies, f_p is the free proton NMR reference frequency corresponding to the magnetic flux density used in the experiment, $\frac{g_\mu(\text{Mu})}{g_\mu}$ is the bound-state correction for the muon in muonium and

$$s_c = \frac{\mu_e}{\mu_p} \frac{g_\mu(\text{Mu})}{g_\mu}, \quad (1.13)$$

where $\frac{g_\mu(\text{Mu})}{g_\mu}$ is the bound-state correction for the electron in muonium.

The most precise value for $\frac{\mu_\mu}{\mu_p}$ obtained by the muonium HFS experiment at LAMPF [18] and the recommended value of μ_μ from CODATA [41] are

$$\frac{\mu_\mu}{\mu_{p \text{ HFS}}} = 3.18334524(37), \quad (1.14)$$

$$\frac{\mu_\mu}{\mu_{p \text{ CODATA}}} = 3.183345107(84). \quad (1.15)$$

$\frac{m_\mu}{m_e}$ is also obtained by $\frac{\mu_\mu}{\mu_p}$ and the equation

$$\frac{m_\mu}{m_e} = \frac{g_\mu \mu_p \mu_B^e}{2 \mu_\mu \mu_p}. \quad (1.16)$$

The value from the experiment and the recommended value of $\frac{m_\mu}{m_e}$ from CODATA [41] are

$$\frac{m_\mu}{m_{e \text{ HFS}}} = 206.768276(24), \quad (1.17)$$

$$\frac{m_\mu}{m_{e \text{ CODATA}}} = 206.7682823(52). \quad (1.18)$$

The uncertainty of the value from muonium HFS is about four times the uncertainty of the recommended value of CODATA. The reason is that measurement of muonium HFS determine the value of $\alpha^2 m_\mu / m_c$. The value of the fine structure constant α is determined by other data with an uncertainty significantly smaller than the value from the muonium HFS experiment at LAMPF (see Section 1.4.2).

Thus more accurate measurement of muonium HFS may determine the values of $\frac{\mu_\mu}{\mu_p}$ and $\frac{m_\mu}{m_e}$.

1.4.2 Testing QED theory

As mentioned in Section 1.3, theoretical predictions of muonium HFS can be obtained with high precision since the complications of proton structure are absent. It enables a most sensitive test of two-body bound state QED. One of the fundamental probes of testing QED theory is the fine structure constant α . α is able to measured by many different techniques (see Figure 1.3). The QED calculation of the HFS is expressed in terms of the $\frac{m_\mu}{m_e}$ and α . A value for α may be evaluated by equating the experimental value of muonium HFS to its theoretical expression.

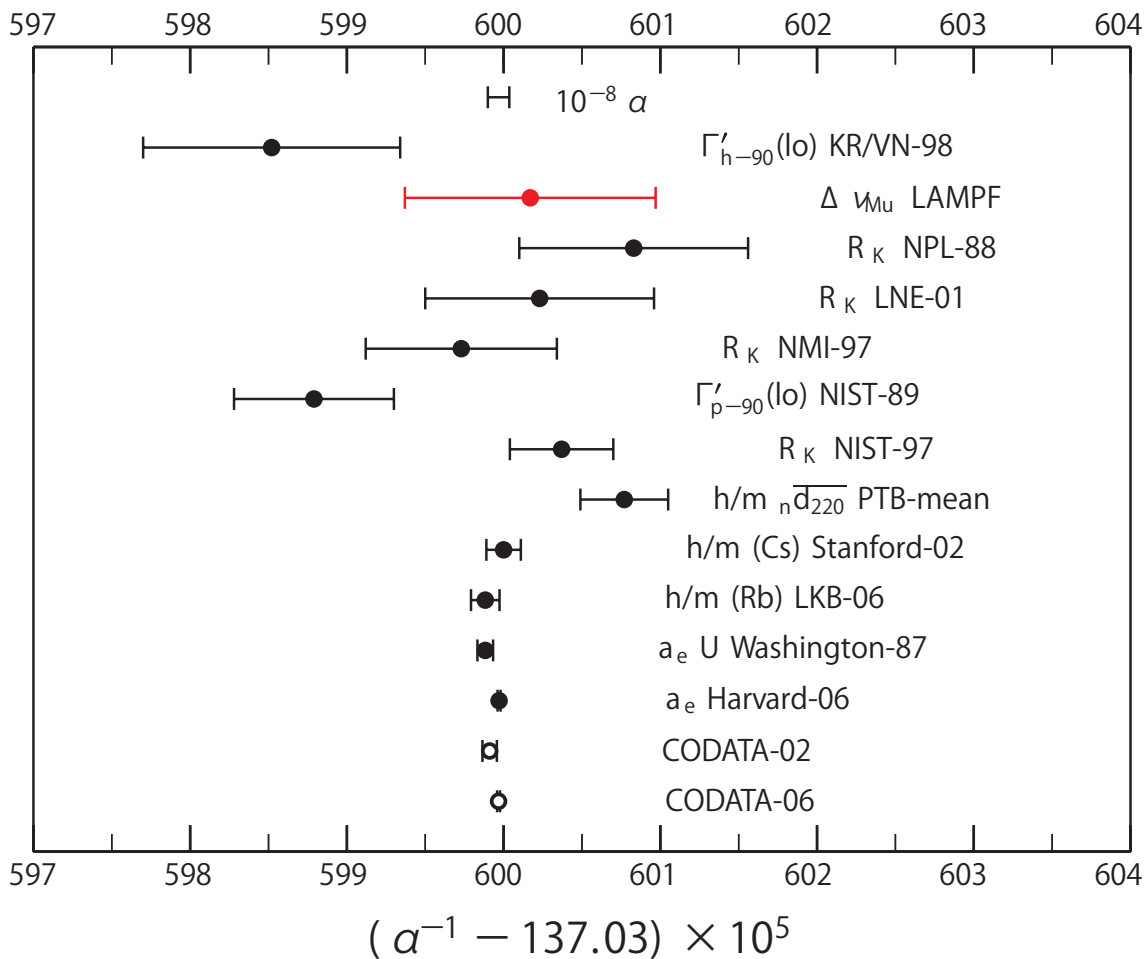


Figure 1.3: Values of fine structure constant publication of the CODATA 2006 [1]

1.4.3 g-2 experiment

One of the contributions of the precise determinations of $\frac{\mu_\mu}{\mu_p}$ and $\frac{m_\mu}{m_e}$ is to the g-2 experiment planned at J-PARC/MLF. The experiment of BNL E821 reported 3σ deviation of anomalous magnetic moment g-2 from Standard Model (see Figure 1.4). It indicates a possibility of new physics beyond the Standard Model. A new muon g-2 measurement is planned at the J-PARC which is able to give factor of 5-10 better than the BNLE821 result. Figure 1.5 shows a conceptual drawing of the experimental setup of g-2 experiment. Polarized muons travel on a circular orbit in a constant magnet field. The muon spin direction is corresponded to muon momentum direction when muons enter the storage ring. By the motion of the muon magnetic moment in the homogeneous magnetic filed the spin axis varies in a particular way as described by the Larmor precession. Larmor angular frequency ω_s is slightly bigger than cyclotron angular frequency ω_c by the difference $\omega_\alpha = \omega_s - \omega_c$ after each cycle.

$$\omega_c = \frac{eB}{2m_\mu}, \quad (1.19)$$

$$\omega_s = \frac{eB}{2m_\mu} + \alpha_\mu \frac{eB}{m_\mu}, \quad (1.20)$$

$$\omega_\alpha = \alpha_\mu \frac{eB}{m_\mu}, \quad (1.21)$$

where $\alpha_\mu = (g-2)/2$ is a anomalous magnetic dipole moment of muon. The magnetic field B is measured by NMR using a standard probe of H_2O at sub-ppm level. This standard probe can be related to the magnetic moment of a free proton by

$$B = \frac{\omega_p}{2\mu_p}. \quad (1.22)$$

where ω_p is the Larmor precession angular velocity of a proton in a water. Therefore, actual value of the measurement is

$$R = \frac{\omega_\alpha}{\omega_p} \quad (1.23)$$

$$= \alpha_\mu \frac{e}{m_\mu} \frac{1}{2\mu_p} \quad (1.24)$$

$$= \alpha_\mu \frac{e}{2m_\mu} \frac{1}{\mu_\mu} \frac{\mu_\mu}{\mu_p} \quad (1.25)$$

$$= \alpha_\mu \frac{1}{g_\mu} \frac{\mu_\mu}{\mu_p} \quad (1.26)$$

$$= \frac{\alpha_\mu}{1+\alpha_\mu} \frac{\mu_\mu}{\mu_p}. \quad (1.27)$$

Thus g-2 value is obtained by both R obtained by g-2 experiment and $\frac{\mu_\mu}{\mu_p}$ determined by muonium HFS, more precise measurement of muonium HFS improves the accuracy of g-2

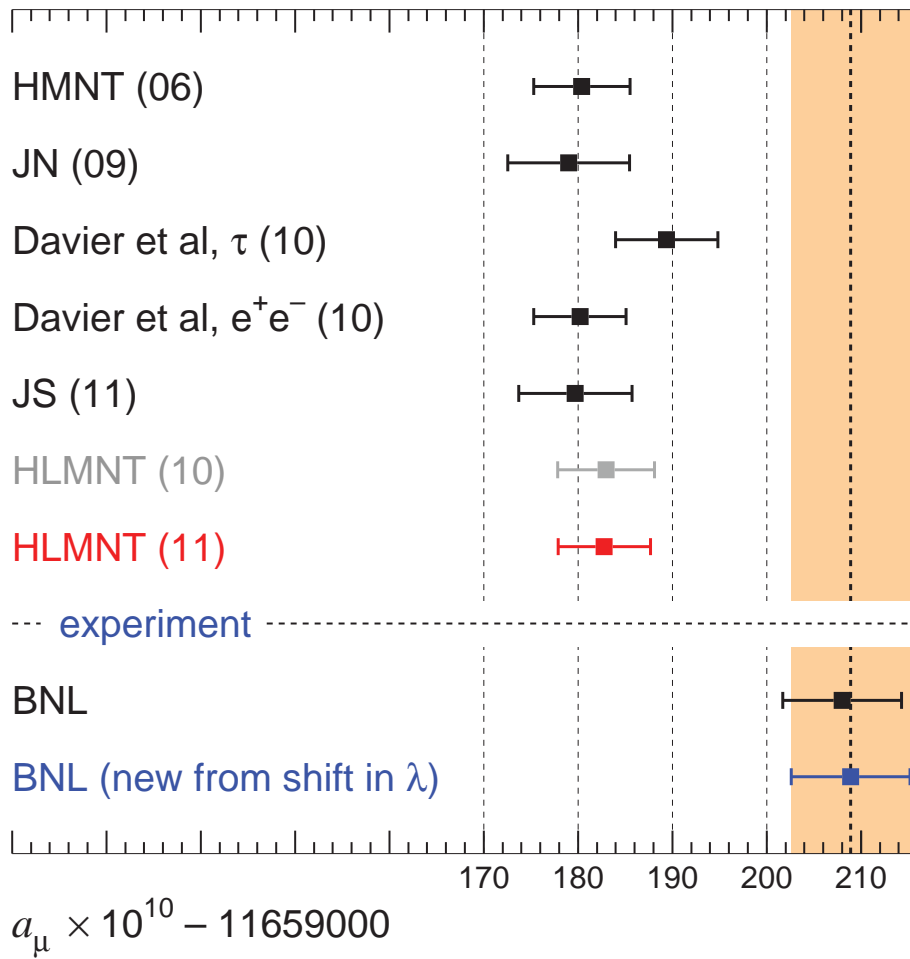


Figure 1.4: A result of $g-2$ measurement at BNL. The significance of the deviation is 2.6 standard deviations from the existing theory [2].

value.

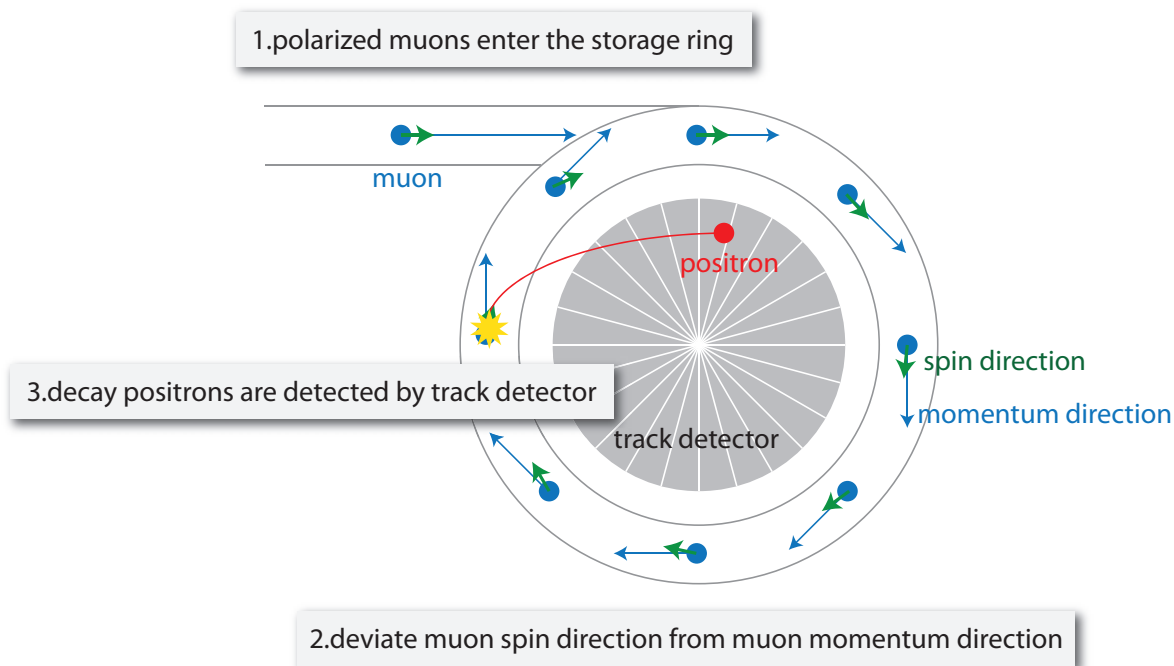


Figure 1.5: A conceptual drawing of the experimental setup of the $g-2$ experiment.

1.4.4 Testing CPT and Lorentz invariance

Hamiltonian terms beyond the standard model violating CPT and Lorentz invariance would contribute frequency shifts of muonium HFS transition. The shifts of muonium HFS would be indicated by anti-correlated oscillations in ν_{12} and ν_{34} at the earth's sidereal frequency. Figure 1.6 shows that no time dependence was found at a level of 20 Hz at the LAMPF experiments [3]. More precise measurement can test the CPT and Lorentz violation.

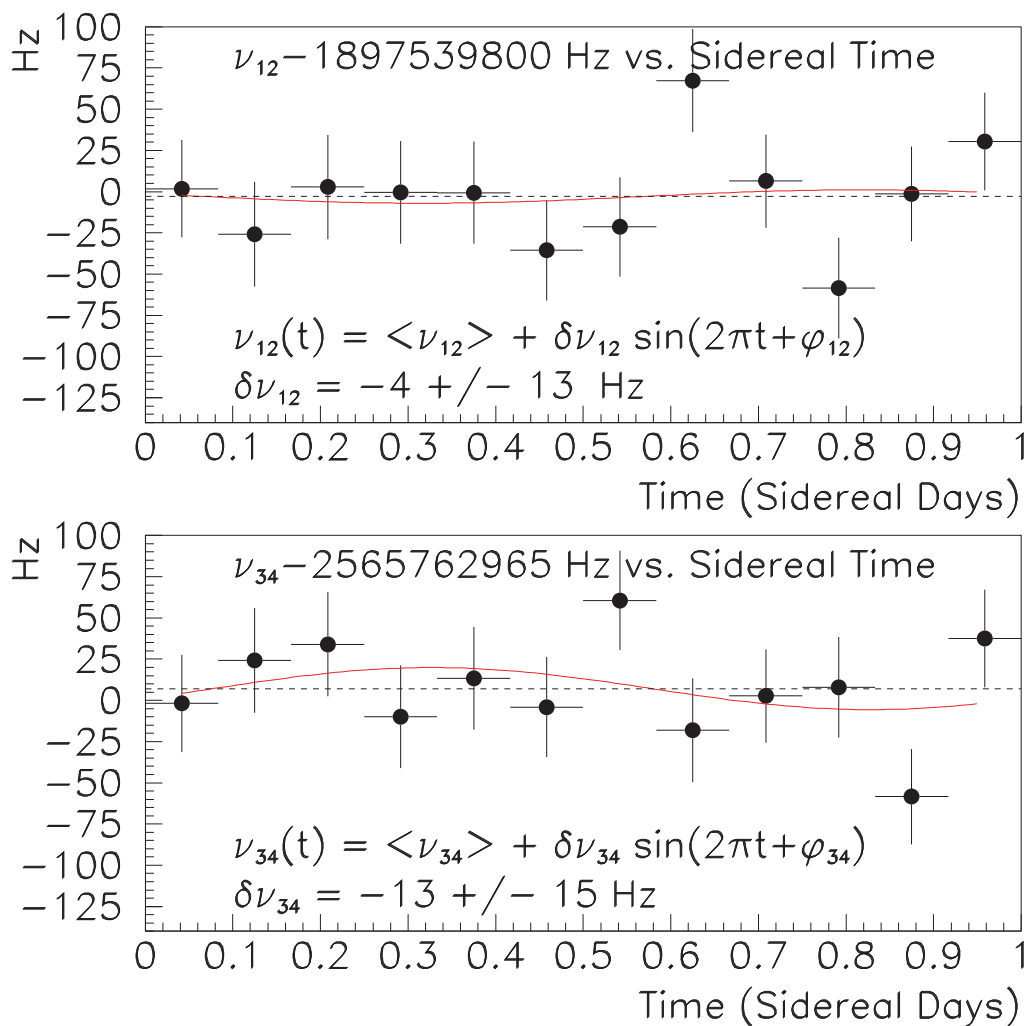


Figure 1.6: Two years of data on ν_{12} and ν_{34} at the LAMPF experiment are shown binned versus sidereal time and fit for a possible sinusoidal variation. The amplitudes are consistent with zero [3].

Chapter 2

Experimental strategy

This chapter describes how to measure muonium HFS. At first, we should prepare polarized muons (see Section 2.1) and produce muonium (see Section 2.2). To prevent an energy shift caused by the Zeeman effect, measurement at zero magnetic field is ideal; nevertheless, it is difficult to keep polarization of muons at zero magnetic field. For this reason, transition frequency of muonium HFS is measured indirectly in a strong field (see Section 2.3).

Components for this experiment is described in Section 2.4.

2.1 How to produce muon

Positive muons are obtained from parity-violating positive pion π^+ decays

$$\pi \rightarrow \mu^+ + \nu_\mu, \quad (2.1)$$

Because of the helicity of neutrino, muons are 100 % polarized in the direction opposite to their momentum.

The lifetime of charged pion is

$$0.26033(5) \text{ ns [42]}. \quad (2.2)$$

A 3 GeV proton beam from the J-PARC Rapid Cycle Synchrotron passes through a carbon target of 2 cm thickness producing pions. Muons are obtained by pion decay. J-PARC/MLF (Material and Life Science Experimental Facility) has four muon beamline, some of which are under construction. Specific performance of MLF muon beam line and candidates for this experiment are described in Appendix B.

2.2 How to produce muonium

Muonium atoms for precision experiments have been produced using three different methods (see Figure 2.1) [43, 44].

2.2.1 Beam foil

Metastable muonium in the 2s state have been produced with a beam foil technique at LAMPF and the TRIUMF [45, 46]. This method is not able to apply our experiment but the measurement of lamb shift transition ($2^2S_{1/2} - 2^2P_{1/2}$).

2.2.2 Silica powder

Muonium obtained by stopping muons near the surface of a SiO₂ powder target. Muons stopped in the silica powder capture electrons and form muonium, some percent of which diffuse to the target surface and then emitted in vacuum [47]. Advantage of this method is that formed in vacuum unlike in the case of gas target. However, this is not appropriate of our experiment because both the production rate and the polarization are low. Moreover, signals of muon decay in vacuum are not able to distinguish from that in a powder target.

2.2.3 Gas target

Muonium is obtained by a electron capture after stopping muon in a suitable noble gas. This technique was employed already in the experiment observed of the muoniums for the first time atom in 1960 in Ar gas. The production rate in this experiment was 65(5) %. In the case of LAMPF HFS experiment, the production rate was 80(10)%. Muon moderation processes involve dominantly electronic interaction and practically no muon depolarization take place in a strong axial magnetic field ($B \gg 0.16$ T) [48]. Thus gas target is a most suitable method for muonium HFS experiments from the aspect of production rate and the rate of polarization.

Comparison of gas targets

In order to avoid chemical reactions and depolarizing collisions, noble gases are candidates for a gas target. Muonium is formed when positive muons are stopped in a gas target by the

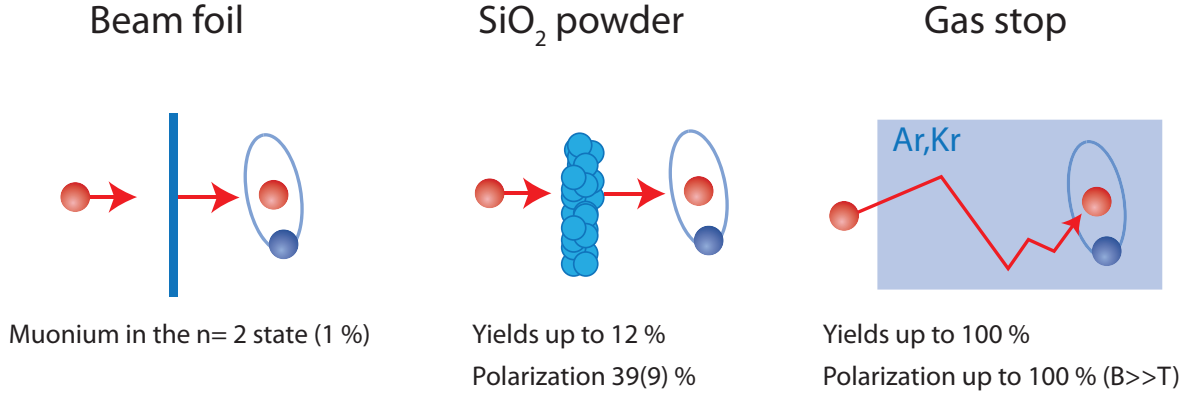


Figure 2.1: A comparison of the methods of muonium production. Gas stop is the most suitable method for the muonium HFS experiment from the aspect of a production rate and a rate of polarization.

following electron capture reaction,



In the case of krypton, the ionization energy of krypton is 14.00 eV and that of muonium is 13.54 eV. A muon can capture an electron from a krypton atom to form muonium in the ground state if the kinetic energy of the muon-krypton system in its center of mass is greater than the threshold value of 0.46 eV and The muonium fractions is about 100 %. Thus krypton is a ideal gas target to form a low energy muonium because of its low threshold value (see Table 2.1).

2.3 How to measure muonium HFS

To prevent an energy shift caused by the Zeeman effect, measurement at zero magnetic field is ideal; nevertheless, strong static magnetic field is required to keep high magnetic field as discussed in Section 2.2. For this reason, transition frequency of muonium HFS at zero magnetic field is measured using the Zeeman Effect in strong field. This section describes how to obtain the value of transition frequency of muonium HFS.

atom or molecule	threshold energy (eV)	pressure (atm)	f_{Mu}
He	+11.04	1.2–3.1	0(1)
Ne	+8.02	1.2	7(5)
Ar	+2.22	1.0–2.8	74(4)
Kr	+0.46	0.4–0.95	100(5)
Xe	-1.41	0.4–0.65	100(4)
N ₂	+2.0	1.0–2.4	84(4)
CH ₄	-0.6	1.2–3.0	87(4)

Table 2.1: Threshold energies for muonium formation [8] and the pressure-independent muonium fractions f_{Mu} [9].

In a magnetic field, the Zeeman Effect splits the energy levels of the muonium ground state. Spin Hamiltonian of muonium is expressed as

$$\hat{H} = \omega_{\mu}\hat{I}_z + \omega_e\hat{S}_z + \omega_0\hat{I}\hat{S}, \quad (2.4)$$

where ω_{μ} is muon Zeeman interaction, ω_e is electron Zeeman interaction and ω_0 is hyperfine interaction, expressed as

$$\omega_{\mu} = -\frac{g_{\mu}}{2} \frac{|e|}{m_{\mu}} B, \quad (2.5)$$

$$\omega_e = -\frac{g_e}{2} \frac{|e|}{m_e} B. \quad (2.6)$$

To determine the energy eigenvalues, we must diagonalize the matrix of the Hamiltonian function H as

$$\hat{H} = \begin{pmatrix} \frac{1}{2}\omega_e - \frac{1}{2}\omega_{\mu} + \frac{1}{4}\omega_0 & 0 & 0 & 0 \\ 0 & \frac{1}{2}\omega_e + \frac{1}{2}\omega_{\mu} + \frac{1}{4}\omega_0 & \frac{1}{2}\omega_0 & 0 \\ 0 & \frac{1}{2}\omega_0 & -\frac{1}{2}\omega_e - \frac{1}{2}\omega_{\mu} - \frac{1}{4}\omega_0 & 0 \\ 0 & 0 & 0 & \frac{1}{2}\omega_e - \frac{1}{2}\omega_{\mu} + \frac{1}{4}\omega_0 \end{pmatrix} \begin{pmatrix} |\alpha\alpha\rangle \\ |\alpha\beta\rangle \\ |\beta\alpha\rangle \\ |\beta\beta\rangle \end{pmatrix}, \quad (2.7)$$

where α and β are eigenfunctions of muon and electron corresponding to spin orientation in

the positive z direction and negative z direction. The spin eigenfunctions are

$$|1\rangle = |\alpha\alpha\rangle, \quad (2.8)$$

$$|2\rangle = c|\alpha\beta\rangle + s|\beta\alpha\rangle, \quad (2.9)$$

$$|3\rangle = c|\beta\alpha\rangle + s|\alpha\beta\rangle, \quad (2.10)$$

$$|4\rangle = |\beta\beta\rangle. \quad (2.11)$$

s and c are

$$s = \frac{1}{\sqrt{2}} \left(1 - \frac{x}{\sqrt{1+x^2}}\right)^{1/2}, \quad (2.12)$$

$$c = \frac{1}{\sqrt{2}} \left(1 + \frac{x}{\sqrt{1+x^2}}\right)^{1/2}, \quad (2.13)$$

where x is

$$x = \frac{(gJ\mu_B^e + g'_\mu\mu_B^\mu)}{\Delta E_{hfs}} B. \quad (2.14)$$

The energy eigenvalues of the Hamiltonian are given in the following Breit-Rabi formula.

$$E_{hfs}^B(F = \frac{1}{2} \pm \frac{1}{2}, m_F) = -\frac{\Delta E_{hfs}^{B=0}}{4} + g'_\mu\mu_B^\mu m_F B \pm \Delta \frac{E_{hfs}^{B=0}}{2} \sqrt{1 + \frac{4m_F x}{2I+1} + x^2}. \quad (2.15)$$

Figure 2.2 is the Breit-Rabi diagram which shows that the ground state splits into four substates in a static magnetic field. ν_{12} and ν_{34} are calculated from Equation 2.15 as

$$\nu_{12} = -\frac{\mu_B^\mu g'_\mu H}{h} + \frac{\Delta\nu}{2} [(1+x) - \sqrt{1+x^2}], \quad (2.16)$$

$$\nu_{34} = +\frac{\mu_B^\mu g'_\mu H}{h} + \frac{\Delta\nu}{2} [(1-x) + \sqrt{1+x^2}]. \quad (2.17)$$

According to Equation 2.16 and 2.17, transition frequency of muonium HFS at zero magnetic field $\Delta\nu$ is obtained by

$$\Delta\nu = \nu_{12} + \nu_{34}. \quad (2.18)$$

Thus muonium HFS transition energy is obtained by summing ν_{12} and ν_{34} .

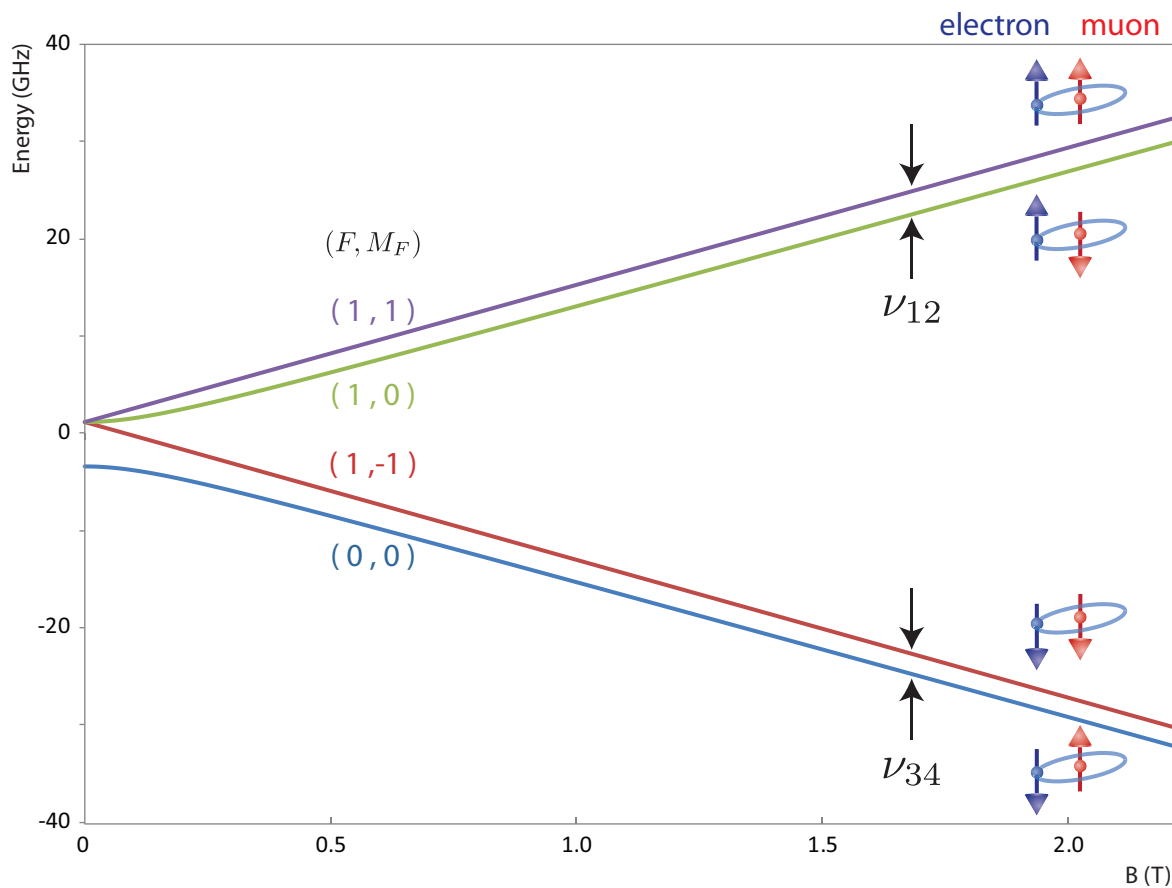


Figure 2.2: Energy levels of the muonium in ground state as a function of external magnetic field. F is the quantum number of the total angular momentum and $M_F = M_s + M_I$.

2.4 Experimental apparatus and procedure

2.4.1 General overview

Figure 2.3 shows a process of muonium HFS measurement.

1. Muons polarized to upstream (see Section 2.1) enter the bore of large superconducting solenoid magnet from J-PARC/MLF muon beam line.
2. RF cavity located in a center of the magnet containing pure Kr gas. Muons stop by collisions in the gas and polarized muonium is formed by electron capture process (see Section 2.2).
3. High momentum decay positrons are emitted preferentially in the direction of the muon spin (see Section 2.4.3). By driving the transitions with an applied microwave magnetic field perpendicular to the static magnetic field, the muon spin could be flipped and the angular distribution of high momentum positrons changed from predominantly upstream to downstream with a respect to the beam direction.

This section described details of apparatus: magnet, detector, profile monitor. Designing of the cavity and the gas chamber are described in Chapter 3. The most important thing for this experiment is to exceed the precision of the LAMPF experiment. It is intended to improve accuracy by a factor of 10. Details of improvement are described in Section 2.5.

2.4.2 Magnet

The superconducting magnet is designed for high homogeneity magnetic field. The maximum magnetic field is 3.4 T for using both this experiment and $g-2$ /EDM experiment at the J-PARC (see Section 1.4.3). A high field uniformity better than 1 ppm with in the spheroid region of 20 cm in diameter and 30 cm in length is necessary accurate (see Section 2.5.2). The magnet consists of main coils and shim coils.

Main magnet

A NbTi superconductor will be used for the coil stand. The strand diameter and Cu/Sc ratio are 2.0 mm and 6. The coil is immersed in a liquid helium of 4.2 K, and the re-condensation cryocoolers will be used for a long term operation. The magnet will be operated in the

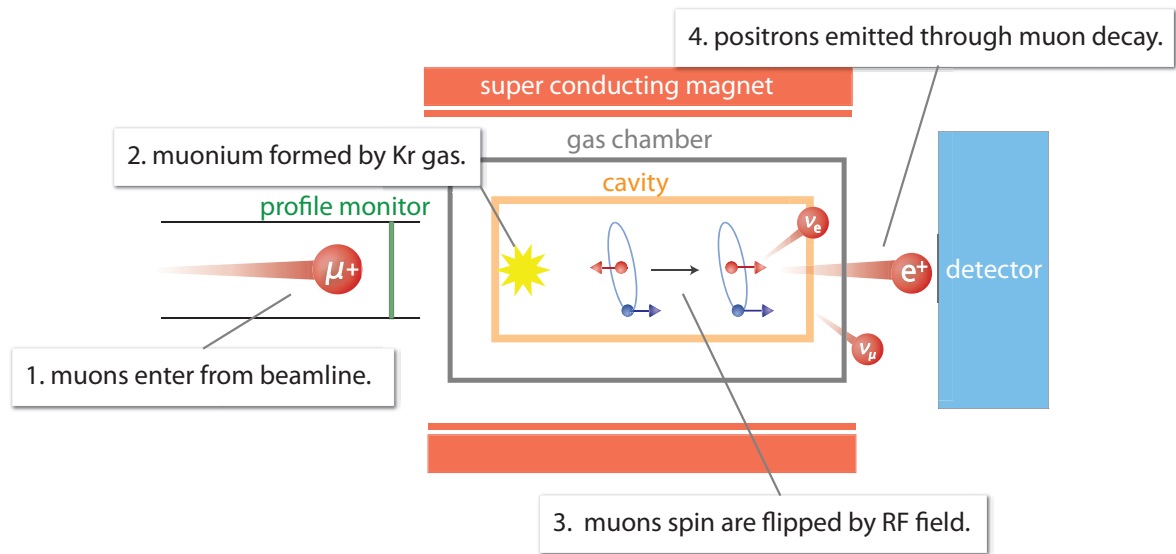


Figure 2.3: A schematic overview of the experimental setup of the muonium HFS experiment.

persistent current mode to remove the field fluctuation due to the ripples of the power supply ($0.01 \sim 0.1$ ppm/h).

Shim coil and iron shim

Main coils alone are not able to realize uniformity of 1 ppm. The error field due to the coil misalignments is expected about 190 ppm. Error fields caused by the main coil misalignment are corrected by shim coils and iron shims.

Iron shim

Iron shims mounted on the surface of the magnet bore will be prepared for a rough correction. The error field would be roughly compensated to several ppm.

Shim coil

For precise correction, 2 or 4 superconducting shim coils are located outer main coils.

NMR system

The magnetic field uniformity is monitored by two different ways.

1. Before beam time, 3 dimensional magnetic field is measured by NMR probe which is mounted 3-axis moving stage.
2. During beam time, magnetic field in the Kr gas chamber is measured by several NMR probe mounted on the outer surface of the cavity constantly.

Reference frequency is obtained from a cesium atomic clock and Rb atomic-clock enhanced stability possible by utilizing GPS as frequency standards.

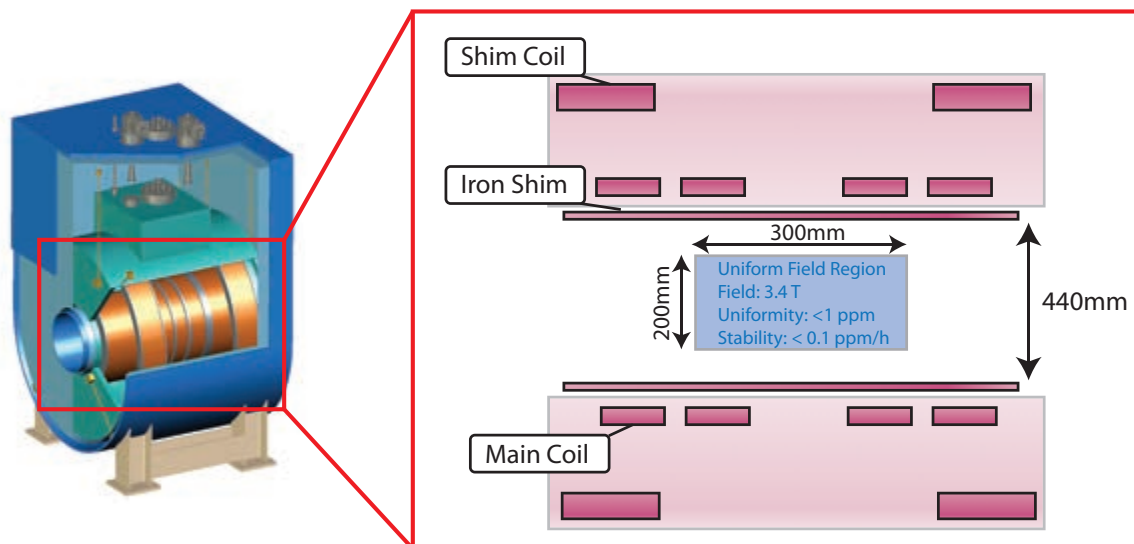


Figure 2.4: An isometric view and a cross-sectional drawing of the magnet. The magnet consist of main coils and shim coils. Error fields are corrected by shim coils and iron shims. A high field uniformity better than 1 ppm with in the spheroid region of 20 cm in diameter and 30 cm in length is necessary accurate.

2.4.3 Positron Detector

Muons decay into positrons in the cavity. Since high momentum decay positrons are emitted preferentially in the direction of the muon spin, by driving the ν_{12} and ν_{34} transition with

an applied RF magnetic field perpendicular to the static magnetic field, the muon spin is flipped and angular distribution of decay positrons changed from upstream to downstream. Positron detectors placed in both upstream and downstream of the chamber to detect the decay muons. Resonance line shapes are obtained from the signal ratio of the upstream detector and the downstream detector.

The fundamental parameters related to muon decay and the development of the positron detector are discussed.

Muon decay

Muons decay via weak interaction like

$$\mu^+ \rightarrow e^+ + \nu_e + \bar{\nu}_\mu \quad (\text{branching ratio} \approx 1) \quad [42] \quad (2.19)$$

Also there are following other processes

$$\mu^+ \rightarrow e^+ + \nu_e + \bar{\nu}_\mu + \gamma \quad (\text{branching ratio} \approx 10^{-2}) \quad [42] \quad (2.20)$$

$$\mu^+ \rightarrow e^+ + \nu_e + \bar{\nu}_\mu + e^+ + e^- \quad (\text{branching ratio} \approx 10^{-5}) \quad [42] \quad (2.21)$$

Equation refection-muon-decay-1 is a dominant process and other processes are rare enough to be neglected.

Muon life time

Muon life time is measured as

$$\tau \equiv 1/\gamma = 2.19703(4) \mu\text{s} \quad (18 \text{ ppm}) \quad [42] \quad (2.22)$$

Spectrum of decay positron momentum

Figure 2.5 shows a spectrum of decay positron's energy so called Michel Spectrum. Maximum momentum of decay positron is below 52.83 MeV/c [4].

Angular distribution of decay positron

The angular distribution of decay positron is described by the following equation and depends on a muon magnetic moment (see Figure 2.6).

$$N(y, \theta) = \frac{\gamma}{2\pi} y^2 [(3 - 2y) + (2y - 1) \cos \theta P_z] \quad (2.23)$$

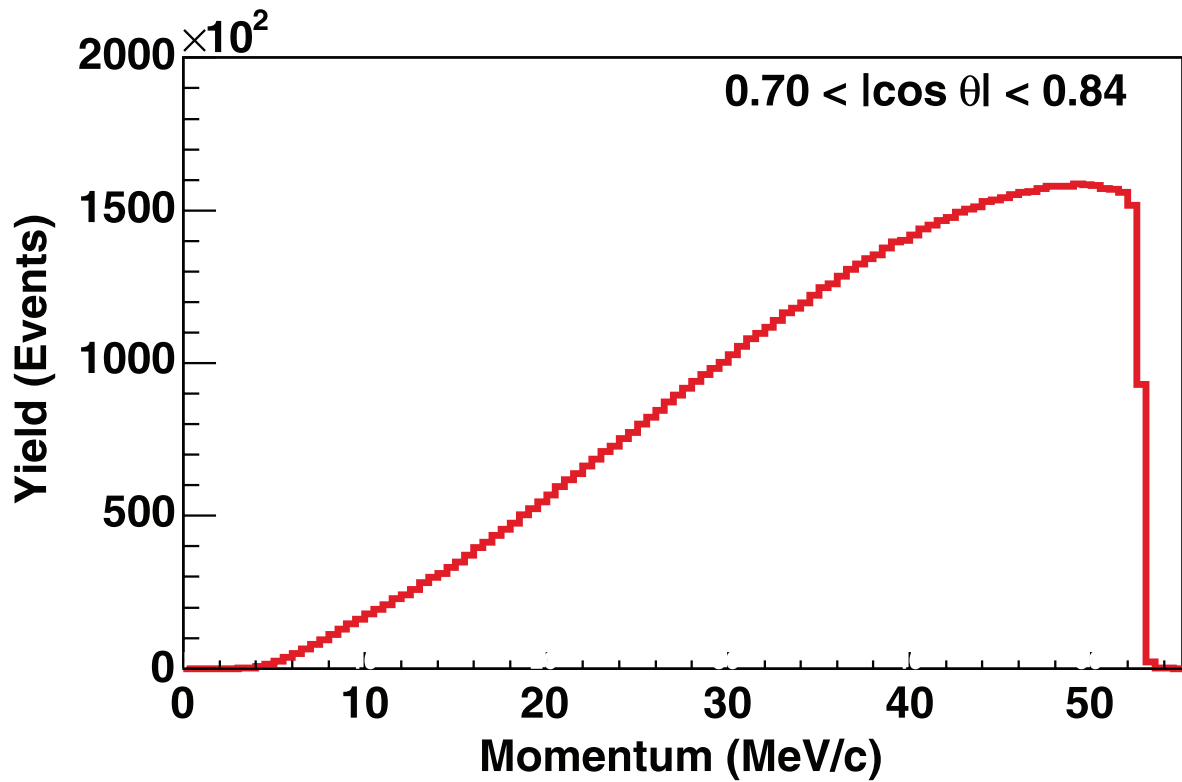


Figure 2.5: A spectrum of decay positron momentum for events within $0.70 < |\cos \theta| < 0.84$ measured at TWIST [4].

in which y is the positron momentum in units of $\frac{1}{2}m_\mu c$; θ is the angle between the muon spin direction and the positron momentum.

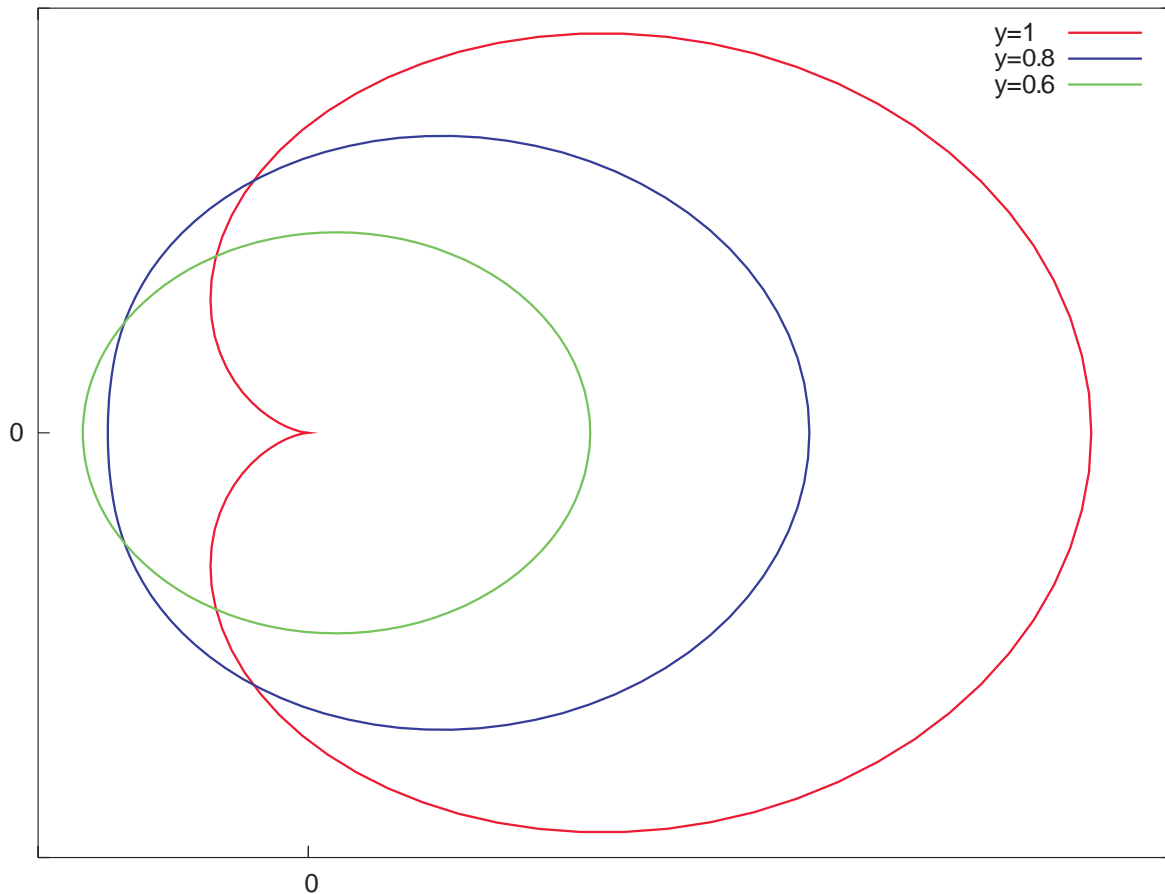


Figure 2.6: An angular distribution of decay positron at several y values expressed in polar coordinates. The direction of muon magnetic moment is rightward.

Since the angular distribution depends on the energy of decay positrons, detection threshold of kinetic energy is set for optimize the signal ratio of the upstream detector and the downstream detector. Preliminary estimation by simulation, the best energy threshold is about 35 MeV.

Designing of the positron detector

Because of the high intensity beam from J-PARC muon beam line, the rate of muon decay is very high. For instance, the muon beam intensity of H-line is $4 \times 10^6 \mu^+ / pulse$. Detection solid angle of the positron detector is about 20 %. In this case, the event rate in first 20 ns is about 3.6×10^{11} Hz.

We use “old muonium” method which we consider the time dependence of the signal observed over time interval t_1 t_2 . This method narrow the linewidth of the resonance line (see Appendix evaluation-of-a-input-RF-power). In case of $t_1 = 3 \tau$, the event rate is about 1.8×10^{10} Hz which is still high. For avoiding pile up problem, highly segmented and fast detector is needed. One of candidates is a highly segmented plastic scintillator and read out by a MPPC (Multi-pixel Photon Counter) which is photon-counting device made up of multi APD (avalanche photodiode) pixels operated in Geiger mode.

2.4.4 Profile Monitor

Monitoring muon stopping distribution is one of the important parameters of this experiment. Magnetic field is not completely homogeneous, so muon stopping distribution is needs to be taken account to calculate average static magnetic field seen by muonium and oscillating magnetic field to calculate transition probability. We use two methods to monitoring muon stopping distribution (see Figure 2.7).

1. Before taking data, 3-dimensional muon stopping distribution in the gas chamber is measured by a target beam profile monitor (TBPM).
2. 2-dimensional muon distribution is measured by a front beam profile monitor (FBPM) simultaneously for calibration during every data taking time.

2.5 Reduce of uncertainties

Figure 2.8 shows uncertainties of the LAMPF experiment and how to improve in our experiment.

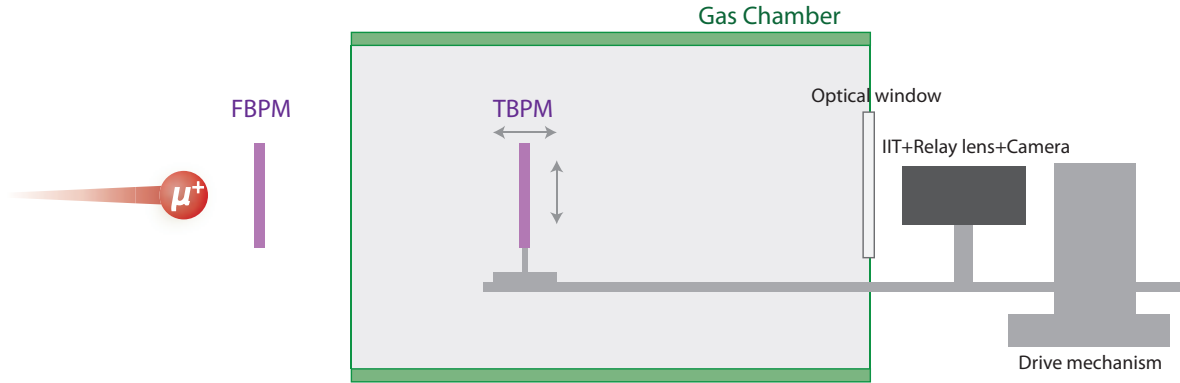


Figure 2.7: A schematic view of the FBPM and the TBPM. The FBPM is used for taking 2-dimensional muon distribution during the experiment. The TBPM is used for taking 3-dimensional muon distribution in the gas chamber before taking data.

2.5.1 statistical uncertainty

The largest uncertainty is statistical uncertainty. It can be improved by high intensity of J-PARC muon beam. The muon intensity at LAMPF muon beam line is a few $\times 10^7 \mu^+/\text{s}$. Nevertheless, the effective muon intensity is $10^7 \mu^+/\text{s}$ because they used muon beam of $3.9 \mu\text{s}$ pulses separated by $9.9 \mu\text{s}$. Total run was 1270 runs, so total muons using this experiment was around 10^{13} .

Our experiment is expected to improve the statistics drastically. At first, the structure of muon beam at J-PARC MLF is pulsed, we can use all muons delivered. In addition to this, the muon intensity is one order of magnitude higher than LAMPF when U line or H line is used (see Table 2.2). For instance if we operate 100 days at U line, total number of muons is 3×10^{15} , which is 300 times as many as that of LAMPF.

2.5.2 Uncertainty of the magnetic field

The second largest uncertainty is caused by magnetic field. It contains uniformity and stability of magnetic field and NMR probe.

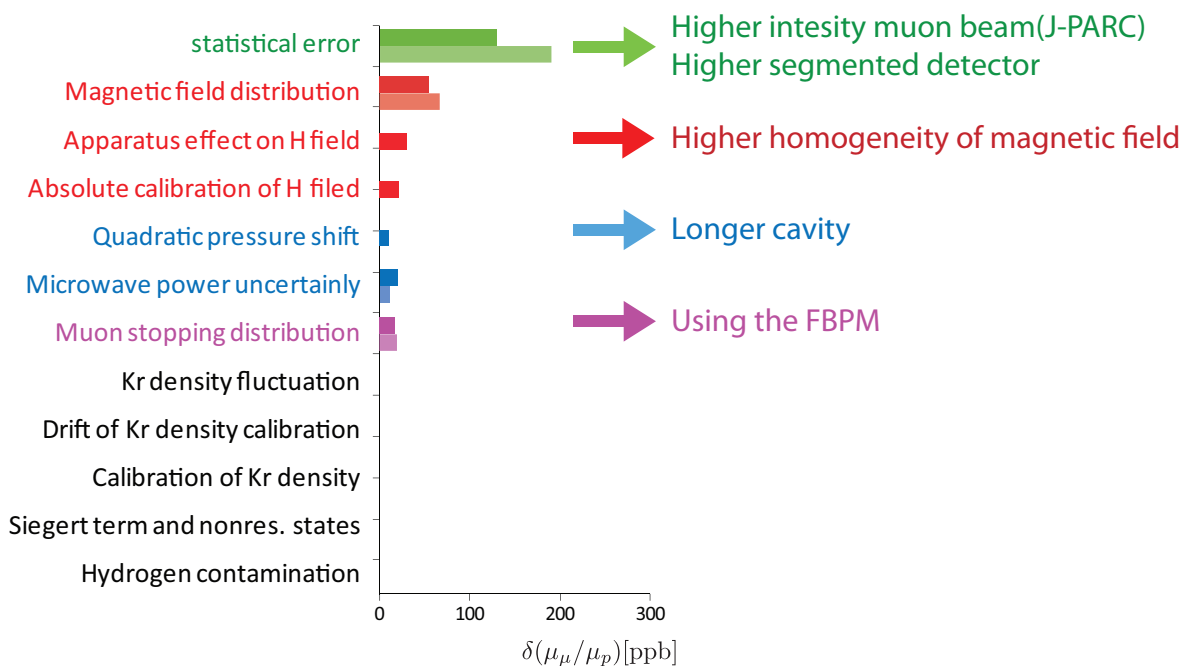


Figure 2.8: Uncertainties of LAMPF experiments and improvements of each of them at our experiment. upper bar is represented $\delta(\mu_\mu/\mu_p)$ obtained by sweeping the magnetic field and another one is by sweeping the microwave frequency.

Facility	Beam Structure	Muon Intensity (μ^+ /s)
LAMPF	DC	a few $\times 10^7$
KEK-MSL	Pulsed	2.5×10^4
RAL	Pulsed	1.5×10^6
PSI	DC	$\sim 5 \times 10^8$
J-PARC (D line)	Pulsed	1.5×10^7
J-PARC (U line)	Pulsed	4×10^8
J-PARC (H line)	Pulsed	1×10^8

Table 2.2: Spec of muon beamline.

Uniformity of a magnet field

Nevertheless, the cylindrical volume contains muonium distribution is larger in our experiments (the axial length of the cavity is 304 mm. on the other hand, that of the LAMPF experiment is 15.973 cm), a field homogeneity of our new magnet is under 0.5 ppm in simulation (see Figure 2.9). This field homogeneity is same degree as 0.7 ppm which is in the cylindrical volume where muons stopped at LAMPF.

Stability of the magnet

A stability of magnet at LAMPF is 10^{-7} to 10^{-8} per hour. In our experiment, the magnet will be operated in a persistent current mode. Also magnetic field is monitored during data taking. The RF signal input to the NMR sample stabilized by reference frequency generator with GPS whose stability is 10^{-11} /day.

2.5.3 Other uncertainties

Improvement of quadratic pressure shift is discussed in Section 3.1.4. Stability of microwave power is improved by rigid coaxial pipe is discussed in Section 3.2.1. In the LAMPF experiment, muon stopping distribution is only taken before the experiment. Uncertainty from muon stopping distribution can be improved by using the FBPM during the experiment which is discussed in 2.4.4.

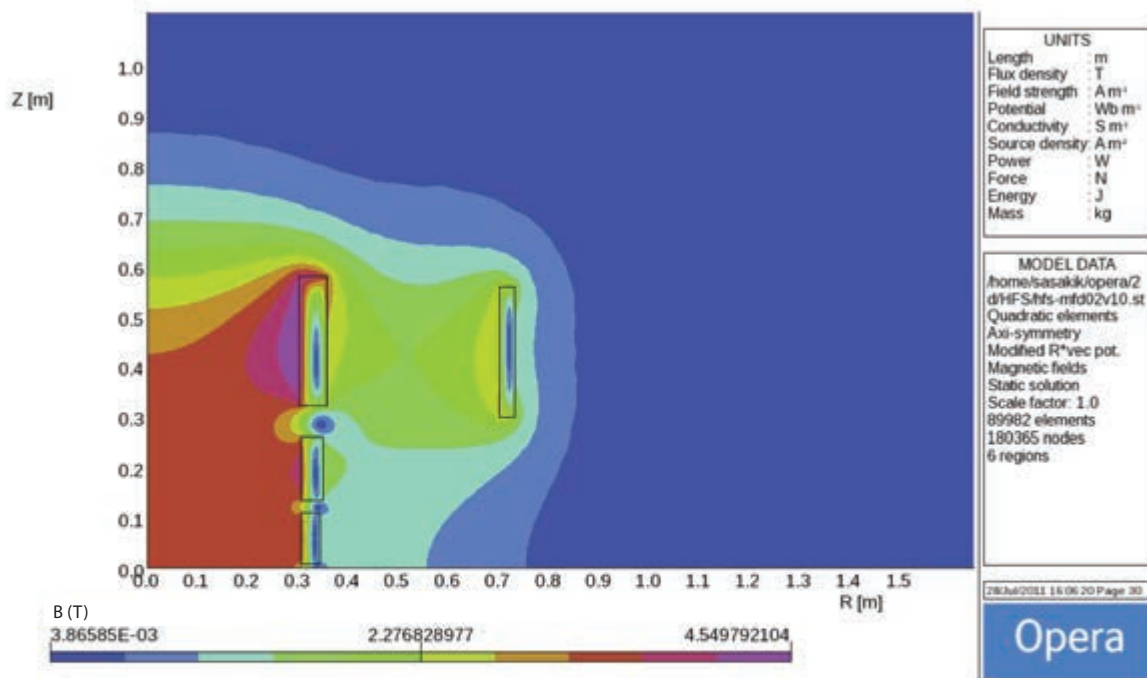


Figure 2.9: A cross-sectional image of uniformity of the magnetic field in the cavity. z is a axial direction of the cavity and r is a radial direction. A field homogeneity of our new magnet under designing is less than 0.5 ppm in simulation using OPERA [5].

Chapter 3

Designing of the cavity and the gas chamber

3.1 Cavity

In this section, a designing of the cavity is described. We choose a cylindrical cavity and it is designed for two resonance modes for driving ν_{12} and ν_{34} transitions. There are following requirements for designing the cavity.

RF ports

Coupling conditions between RF ports and the cavity depend on resonance frequencies so that RF input ports are required for each transition. In addition to this, we should put in a output RF port in order to check a stability of the RF power in the cavity. Therefore, there need to be put in two RF input ports and one RF output port.

Size of the cavity

The cavity is surrounded by the superconducting magnet whose inner diameter is 440 mm. All components of the cavity should set in this area.

Nonmagnetism

For achieving a high uniformity of the static magnetic field in the cavity, magnetism materials are not be able to used at all even austenitic stainless steels.

3.1.1 Resonance modes

The resonance frequencies should be tuned into the ν_{12} and ν_{34} transition frequencies. There are following requirements,

- (a) Static magnetic field and oscillating field are perpendicular to each other,
- (b) The transition efficiencies should be maximized at the center of cavity, that is region muonium formed,
- (c) The oscillating field is constant along the axis.

By the requirement (a), a Transverse Magnetic (TM) resonant modes are more appropriate than a Transverse Electric (TE) mode since a static magnetic field vector is parallel to the axial direction of the cavity. By the requirement (b) and (c), TM_{mn0} which does not have node in the axial direction are candidates. (The TM mnp mode is characterized by three subscripts m , n and p that corresponding to the number of half waves of the electric or magnetic field that fit along the diameter, circumference, and length of the resonator.). Therefore, TM_{110} and TM_{210} modes which are lower-order modes of TM_{mn0} are appropriate from these requirements.

Figure 3.2 shows a electromagnetic field of TM_{110} and TM_{210} modes (see Appendix C). The resonance frequencies for TM modes are

$$f_{mnp} = \frac{c}{n} \sqrt{\left(\frac{x_{mn}}{\pi D}\right)^2 + \left(\frac{q}{2L}\right)^2}. \quad (3.1)$$

Here c is the speed of light, D and L are the diameter and length of the cavity, n is the index of refraction for the medium inside the cavity, and x_{mp} is the p th root of the Bessel function $J_m(x)$.

Figure 3.1 shows a relation between a ratio of the ν_{12} and the ν_{34} transition frequencies and a ratio of the resonance frequencies of the TM_{110} mode and the TM_{210} mode. For measurement of both transitions, static magnetic field is defined so as to equalize these ratios one another. One of a solution is about 0.8 T. However, a stronger magnetic field is desirable from the aspect of a polarization of muons. Therefore, we chose 1.55 T as the static magnetic field.

Figure 3.3 shows positions of RF ports. To accumulate RF power in the cavity, RF ports without one transporting RF power should not be coupled to the cavity. The positions of

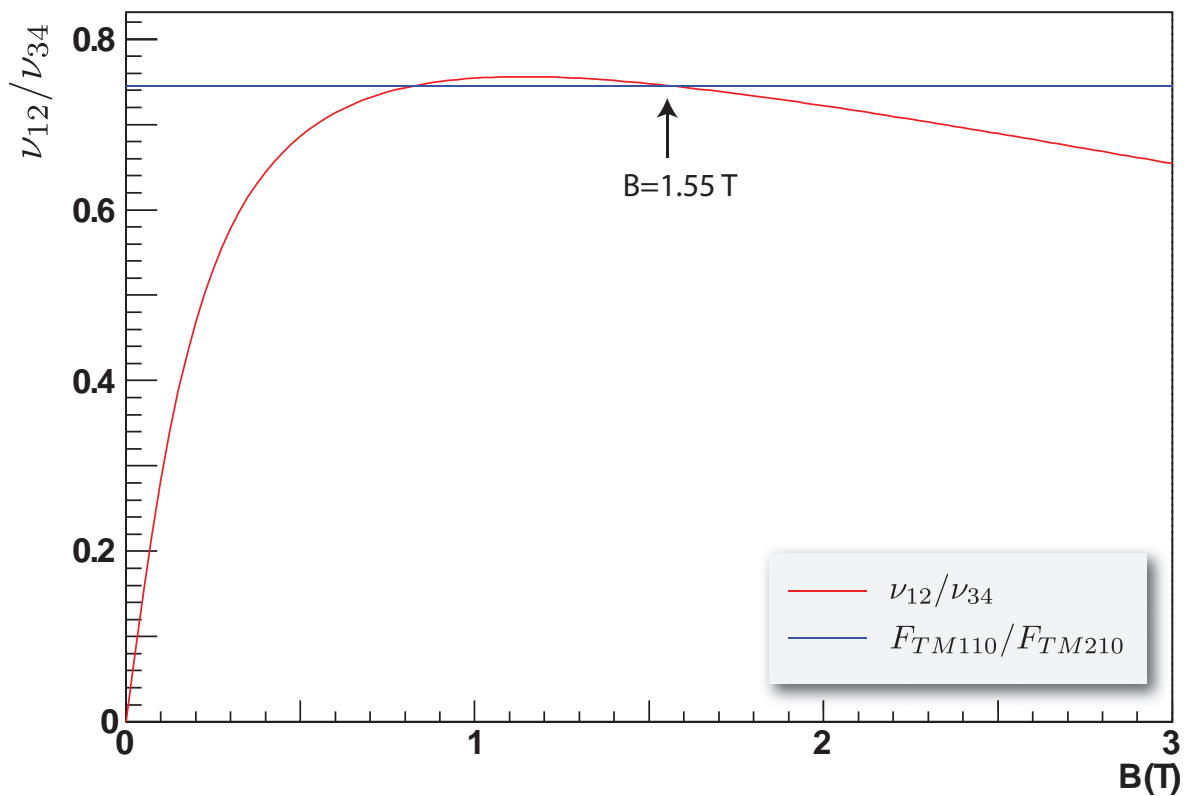


Figure 3.1: A relation between a ratio of the ν_{12} and the ν_{34} transition frequencies and a ratio of resonance frequencies of the TM110 mode and the TM210 mode. Since the ratio of the TM110 mode and the TM210 mode is constant at a cylindrical cavity, there only two solutions to be tuned in to both transitions.

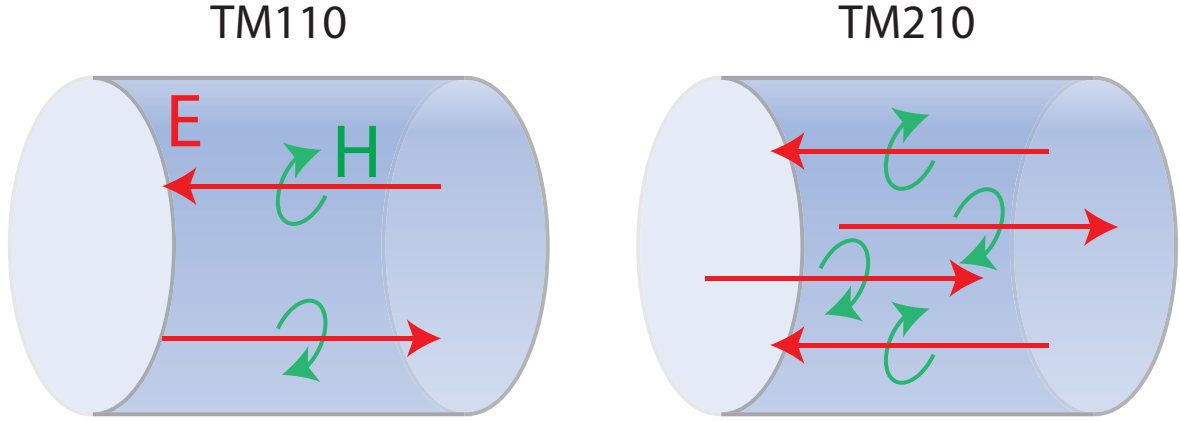


Figure 3.2: RF fields of the TM110 mode and the TM210 mode. The red arrow shows the electric field vector and the green one shows the magnetic field vector.

input ports for TM110 (TM210) mode are chosen not to couple TM210 (TM110) mode. The position of the output port is chosen couple to both modes weakly.

3.1.2 Diameter of the cavity

Transition frequencies of ν_{12} and ν_{34} are obtained by 2.16 and 2.17 as

$$\nu_{12} = 1.906 \text{ GHz}, \quad (3.2)$$

$$\nu_{34} = 2.556 \text{ GHz}. \quad (3.3)$$

The resonance frequencies of the cavity should be a little higher than the transition frequencies since tuning bars in the cavity increase resonance frequencies (see Section 3.1.3). The resonance frequencies of the TM110 mode and the TM210 mode are 1.955 GHz and 2.620 GHz for a diameter of the cavity of 187mm (see Equation 3.1). RF fields of the TM110 mode and the TM210 mode are described in Appendix C.

3.1.3 Tuning bar

Resonance curves are obtained from microwave frequency sweep. Frequency sweep is achieved by tuning bars located inside the cavity. Inserting a tuning bar into the cavity results in a

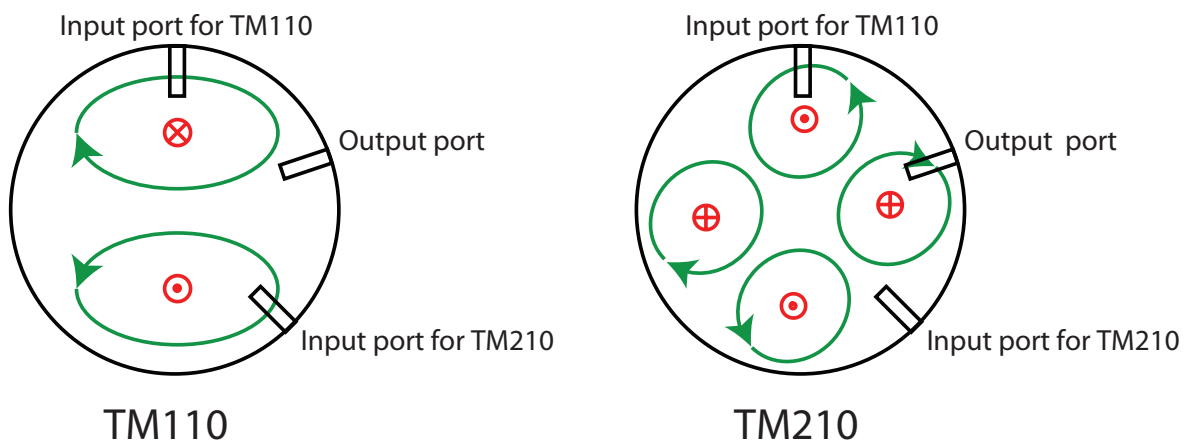


Figure 3.3: A cross-sectional view of the cavity with the TM110 mode and the TM210 mode. The red arrows indicate the electric field and the green arrows indicate the magnetic field. The positions of the input ports for the TM110 (TM210) mode are chosen not to couple the TM210 (TM110) mode. The position of the output port is chosen couple to both modes weakly.

increase in resonant frequencies.

Cavity perturbations

When a dielectric material is inserted into the cavity, resonance frequency is shifted. A corresponding change in resonance frequency is able to be approximated as

$$\frac{\omega - \omega_0}{\omega_0} \approx \frac{\int \int \int_{\Delta V} (\mu |H_0^2 - \epsilon |E_0|^2) dv}{\int \int \int_{\Delta V} (\mu |H_0^2 + \epsilon |E_0|^2) dv} \quad [49], \quad (3.4)$$

where ω_0 is the resonance frequency of the original cavity and ω is one of the perturbed cavity. The perturbed fields are approximated by the original fields E_0 and H_0 . However, analytical evaluation using this equation is not realistic so that a simulation software using a finite element method is used.

CST microwave studio

Unlike an ideal cylindrical cavity, simulation using finite element method is needed to evaluate the cavity considering a structure of RF ports and tuning bars. CST microwave studio [50] is one of such software for the 3D EM simulation of high frequency components. There are several solvers available. Among them, following two solvers are mainly used.

Eigenmode Solver

The Eigenmode Solver is dedicated to the simulation of closed resonant structures. It is for estimating the electromagnetic field of resonance modes and Q factor (see Section 4.1.1).

Frequency Domain Solver

The general purpose Frequency Domain Solver solves the problem for a single frequency at a time, and for a number of adaptively chosen frequency samples in the course of a frequency sweep. The solution comprises the field distribution as well as the S-parameters (see Section 4.1.1) at the given frequency so that it is an appropriate solver for comparison with the line shapes of S-parameter obtained from network analyzer (see Section 3.2.5).

Material for tuning bar

As for the material of the tuning bar, there are critical differences between conductive and dielectric ones. A conductive tuning bar affects the electric field as if it shrinks the diameter of the

cavity. On the other hand, dielectric tuning bar affect as widen it by absorbing RF power (see Figure 3.4). As a result of these characters, conductive tuning bar decrease resonance frequencies and dielectric one increase them.

A next thing to consider is which one is appropriate for the experiments. A conductive material is very sensitive to resonance frequency, but it drastically affect the uniformity of RF electric field (see Figure 3.1). Moreover, whereas sweep range of conductive tuning bar is defined by a position of its surface, that of dielectric tuning bar is defined by its volume so that it is possible to adjust sweep range flexibly. Therefore, dielectric material is a candidate list of material for tuning bar.

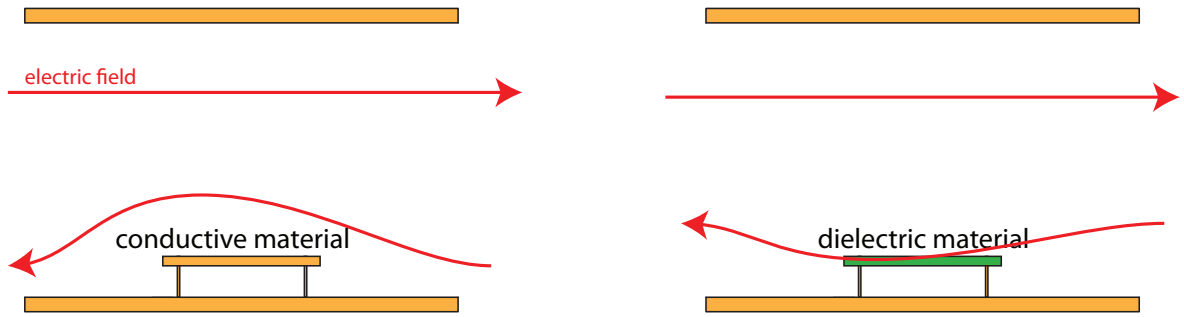


Figure 3.4: An electric field difference between using a tuning bar made of a conductive material and a dielectric material. The conductive tuning bar affects electric field as shrink a diameter of the cavity. On the other hand, The dielectric tuning bar affect as widen it by absorbing RF power.

For choosing better material for tuning bar in dielectric materials, following parameter should be considered.

electric permittivity

Complex dielectric constant is described as

$$\epsilon = \epsilon' - j\epsilon'' \tag{3.5}$$

$$\tan \delta = \frac{\epsilon''}{\epsilon'} \tag{3.6}$$

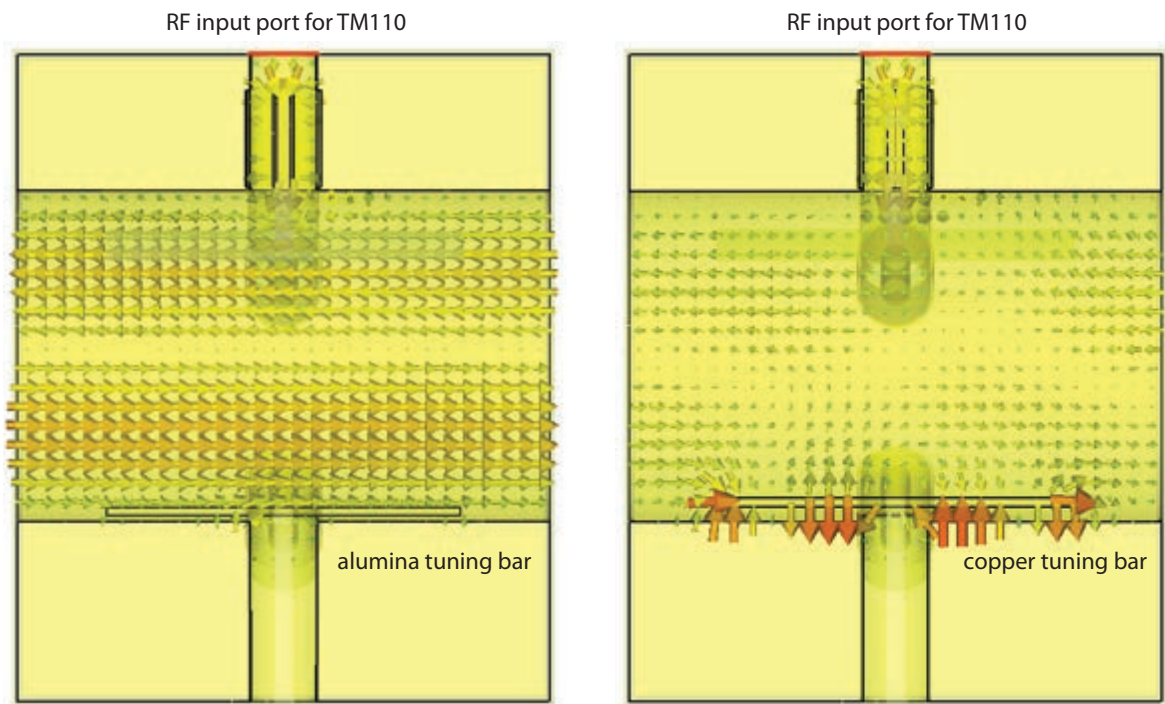


Figure 3.5: Electric fields of the TM₁₁₀ mode using a alumina and a copper tuning bars. Using the copper tuning bars, strong resonance between the tuning bars and the the cavity face is induced. On the other hand, the uniformity of the RF field is better with the alumina tuning bars.

Real part of permittivity (ϵ') is expressed phase difference from oscillation electric field and amplitude of polarization. Wavelength of RF is shorten in the dielectric material. Effective volume of the cavity is expanded by inserting tuning bar made by dielectric material. As a result, the resonance frequency of the cavity is increased.

dielectric tangent

Imaginary part (ϵ'') is expressed dielectric loss. A part of RF power is converted into heat in the dielectric material. It causes reduction of Q factor of the cavity (see Section 4.1.1). In general, dielectric tangent ($\tan \sigma$) is used for estimation of it.

small density

Total weight of tuning bar and support of it must be under 200 g which is the maximum vertical load of the positioner (see Section 3.1.3).

Therefore, a good material for tuning bar should have

1. large electric permittivity
2. small dielectric tangent
3. small density

Tuning bars are supported by tuning bar supports placed on positioners (see Figure 3.6). Unlike in the case of tuning bars, tuning bar supports should not affect resonance frequencies. Therefore, good material for support of tuning bar should have

1. small electric permittivity
2. small dielectric tangent
3. small density

According to this, We choose a alumina for the tuning bar and Teflon to the tuning bar support of the tuning bar with reference to Table 3.1.

Movement mechanism

Piezo positioner

Piezo element converts electrical energy into mechanical energy. Precise movement is achieved

material	electric permittivity	dielectric tangent	density
macor	6.03	0.007 (8.6 GHz)	2.52
alumina	9.5	0.0002 (1 GHz)	3.9
quartz	3.5	0.0002 (100 MHz)	
silicon	12	0.005 (1 GHz)	2.2
Teflon	2.1	0.00028 (3 GHz)	2.2

Table 3.1: Characteristics of materials for the tuning bar.

by piezo positioner ANPz101eXT12/RES/UHV (Attocube Systems) using this character (see Figure 3.8). Positioner is driven by sawtooth pulses from a controller. For precise positioning, feedback from displacement sensor is required since displacement of positioner doesn't bear a proportionate relationship to applied voltage. This positioner using a resistor located in a positioner as displacement sensor. Absolute positioning is enabled by reading a resistance value. Table 3.2 shows a spec of ANPz101eXT12/RES/UHV.

Piezo positioner has following advantages for our experiments.

Simple wiring Since the positioner is driven and read resistance value by only electrical wirings, only simple feed through port at gas chamber is needed. It is ideal for purity of Kr gas in a chamber. Also it is UHV compatible model so that there is no problem in measuring up to 150 °C baking and outgassing rate is below a level of 1×10^{-10} mbar l/s.

Compactness Space between inner surface of superconducting magnet and gas chamber is limited (≈ 80 mm). For example, it is impossible to put in a linear manipulator using bellows. On the other hand, the height of the positioner is only 48 mm which is enough compact to put in.

Nonmagnetism It is made of titanium so that hardly affect to uniformity of the magnetic field.

Piezo controller

Piezo positioners are controlled by piezo controller ANC350/3/RES (attocube systems) (see Figure 3.9). As shown in Figure 3.7, it has 3 channels for manipulating each positioner.



Figure 3.6: A schematic drawing of the tuning bar.

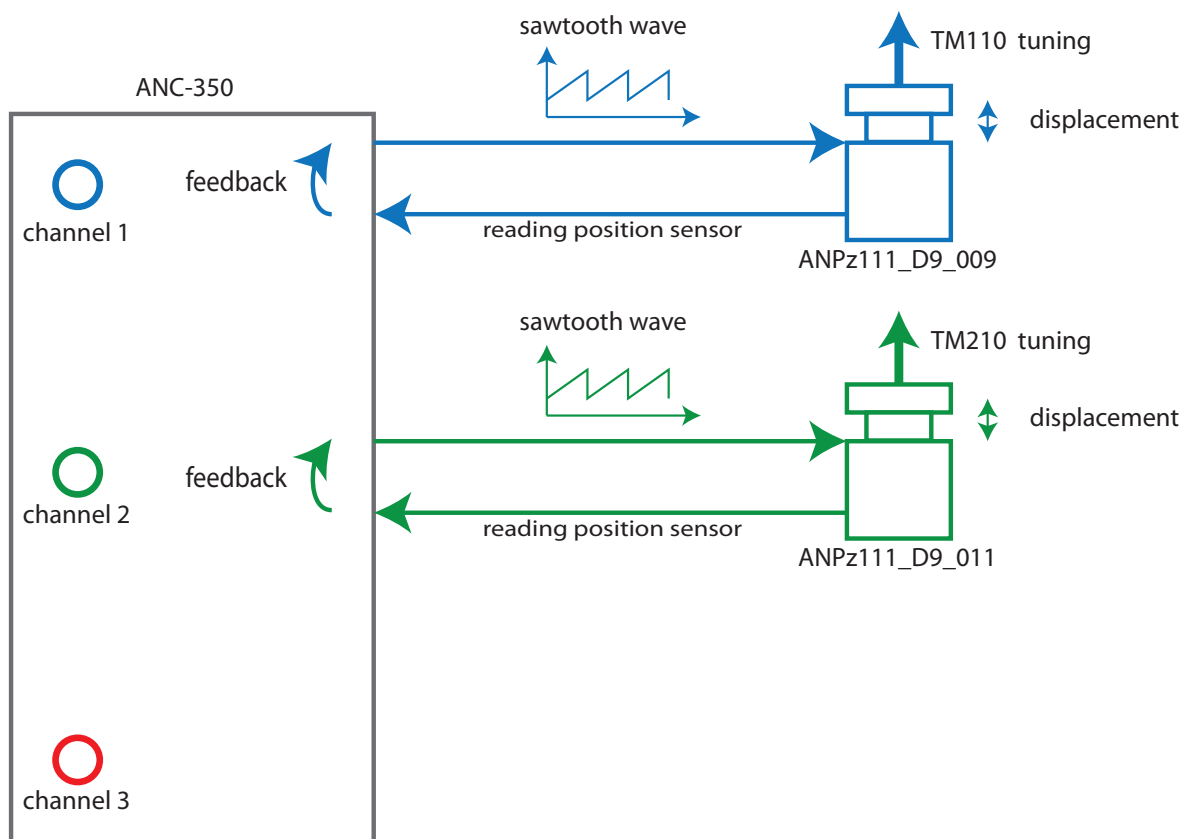


Figure 3.7: A diagram of a positioner system. ANC-350 has three channels to operate the positioners. It transmits sawtooth waves to each positioner and displace their stages in proportion to amplitude of waves. Precise displacement is achieved by feedback from a positioner sensors.

travel (step mode)	12 mm
typical minimum step size	50 nm
maximum vertical load	200 g

Table 3.2: Spec of ANPz101eXT12/RES



Figure 3.8: A photograph of piezo positioner.



Figure 3.9: A photograph of piezo controller.

Sweeping

The TM110 mode and the TM210 mode split into two submodes by tuning bars. One of modes is affected by the tuning bar strongly (TM110-1, TM210-1), and another mode is not affected so much (TM110-2, TM210-2). The resonance frequency of former modes is used for obtaining resonance curves. Figure 3.10 and 3.11 shows the location of tuning bar in a cross section drawing of the cavity. There are two tuning bars for each of the mode. The tuning bars are located to affect RF electric field efficiently. Figure 3.12 shows the relation of frequency sweep and a displacement of tuning bar by the simulation. Using this tuning bar, the range of frequency sweep is about 20 MHz and minimum step size is about 100 Hz.

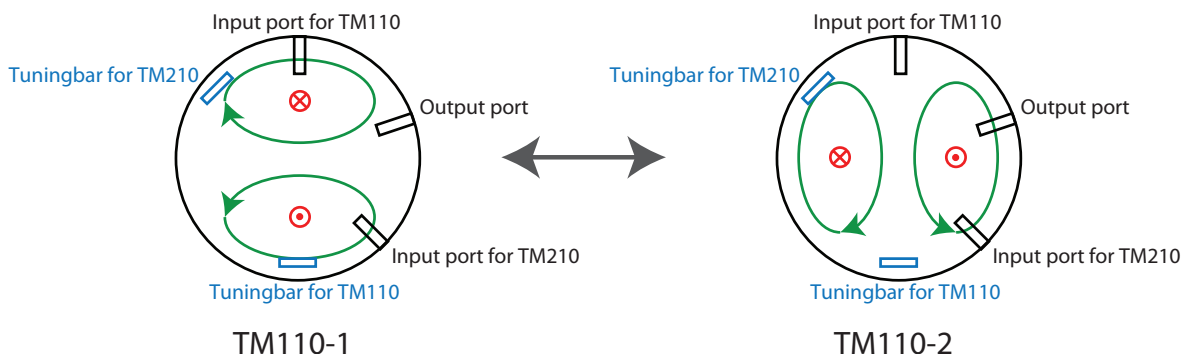


Figure 3.10: Degenerated modes of the TM110. The left side (TM110-1) of resonance mode is affected by tuning bar for TM110 stronger than the right side (TM110-2). Then this mode is appropriate to using for the resonance frequency sweep.

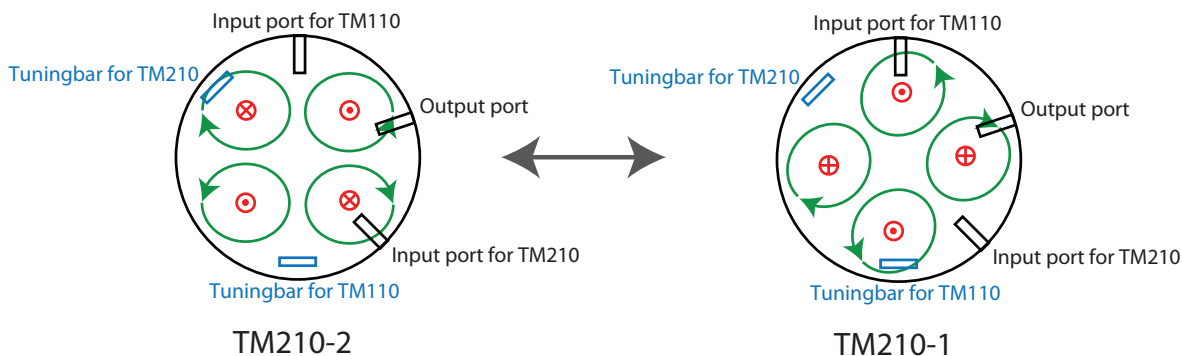


Figure 3.11: Degenerated modes of TM210. The left side (TM210-1) of resonance mode is affected by tuning bar for TM110 stronger than the right side (TM210-2). Then this mode is appropriate to using resonance frequency sweep.

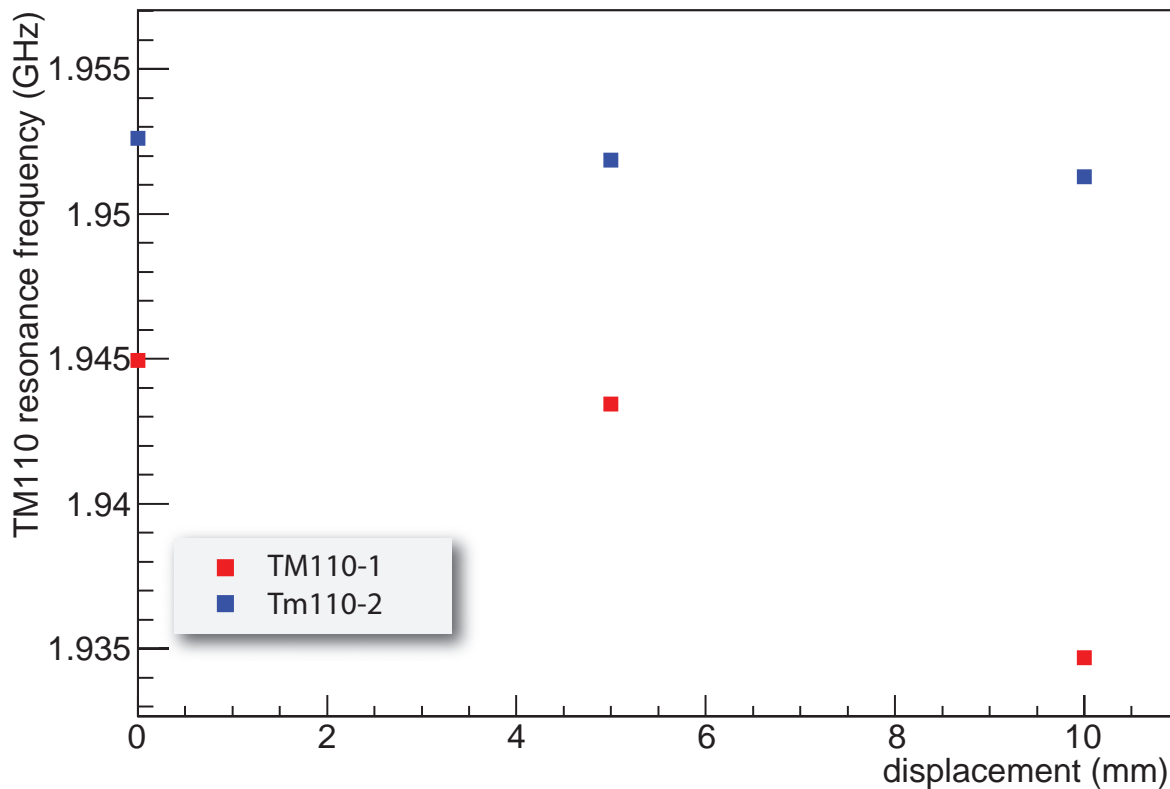


Figure 3.12: A relation between resonance frequency of the TM110 mode and the displacement of the tuning bar. This is a result of the simulation using alumina tuning bars ($20 \text{ mm} \times 200 \text{ mm} \times 2.5 \text{ mm}$). Origin points of tuning bars are defined as 5 mm far from the cavity face. The TM110 mode is splitted into two degenerated modes. The red point is the TM110-1 mode and the blue point is the Tm110-2 mode. The TM110-1 mode is more sensitive to the displacement.

3.1.4 Axial length

Advantage of a long cavity

The transition frequencies of muonium measured in a gas vary with the gas pressure due to the distortion of the muonium wavefunction in collision. At a constant temperature, two-body collisions between a muonium atom and a krypton atom cause a shift which is proportional to the krypton pressure at fixed volume [51]. Also three-body interaction between muonium atom and two krypton atoms yield a shift proportional to the square to the krypton pressure at fixed volume [52]. The shift in the transition frequency is described as

$$\nu_{ij}(P) = \nu_{ij}(0)(1 + a_{ij}P + b_{ij}P^2) \quad (3.7)$$

b is obtained by earlier experiment at LAMPF [53] as

$$b = (9.7 \pm 2.0) \times 10^{-14} \text{ Torr}^{-2} \quad (3.8)$$

So the effect of the quadratic term is so small that difference between b_{12} and b_{34} can be neglected.

a is also obtained by latest experiment at LAMPF [18] as

$$a_{12} = -8.669(26) \times 10^{-6} \text{ atom}^{-1} \quad (3.9)$$

$$a_{34} = -7.665(25) \times 10^{-6} \text{ atom}^{-1} \quad (3.10)$$

The transition frequencies ν_{12} and ν_{34} in vacuum are determined by fitting the measured frequencies at several different gas pressures (see Figure 3.14). To assure accuracy of this fitting, measurement at wide range of Kr gas pressure is necessary. The longitudinal distribution of muonium depends on the Kr gas pressure. Long cavity is preferred for measurement at low pressure Kr gas, because the muonium distribution is wide spread. Figure 3.15 shows the longitudinal distribution at 0.3 atm by Monte Carlo simulation using SRIM [54]. SRIM is a group of programs which calculate the stopping and range of ions into matter using a quantum mechanical treatment of ion-atom collisions. In this simulation, a moderator is put in front of the cavity to stop muons in the region of the cavity whose axial length is 15.973 cm which was used at LAMPF experiment. Only 68 % of muons stop in the cavity.

On the other hand, Figure 3.16 shows the corresponding distribution for the cavity for J-PARC/MLF experiment whose axial length is 304 mm. Because of the length of this cavity,

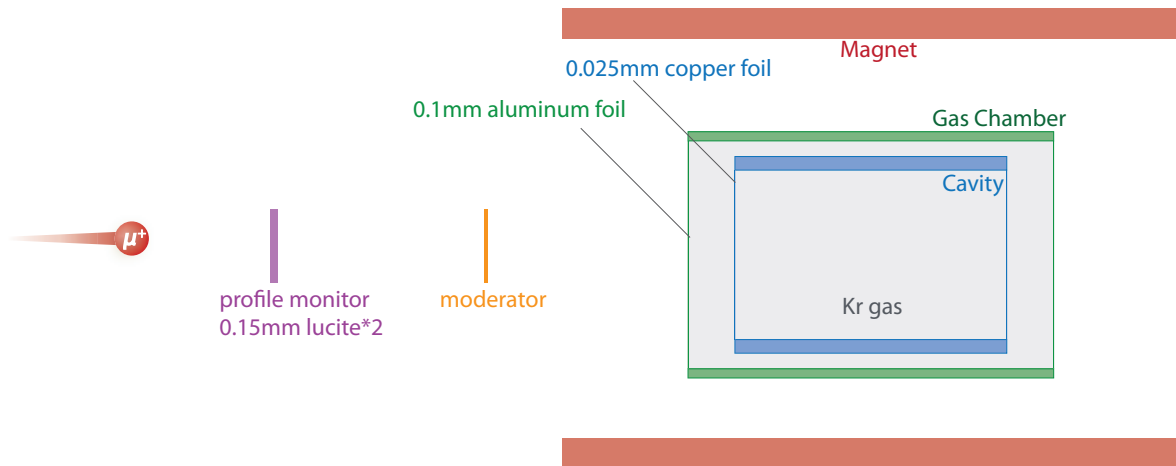


Figure 3.13: Muons pass through a profile monitor, a moderator, a foil of chamber and a foil of the cavity and stop in the cavity by Kr gas. Those materials must be thin enough to enable muon passing through.

the moderator can be thin. Then the muon stopping distribution is brought within the cavity (94 % of muons stop in the cavity). Thus measuring in a lower pressure is possible by using a long cavity and our cavity is available over 0.3 atm by this simulation.

Avoiding other modes

There are many other resonance modes depending on the cavity length (see Figure 3.17). On the other hand, resonance frequencies of the TM110 mode and the TM210 mode do not depend on the cavity length. The cavity length should be chosen carefully to avoid other modes. Figure 3.18, 3.19 and 3.20 show resonance modes nearby the TM110 mode. If the cavity axial length is 300 mm, a TM012 mode is located between splitted the TM110 modes (the TM110-1 mode and TM110-2 mode) which is undesirable. In the case the cavity axial length is 304 mm, resonance frequency of the TM012 mode is low enough to be separated from the TM110 mode.

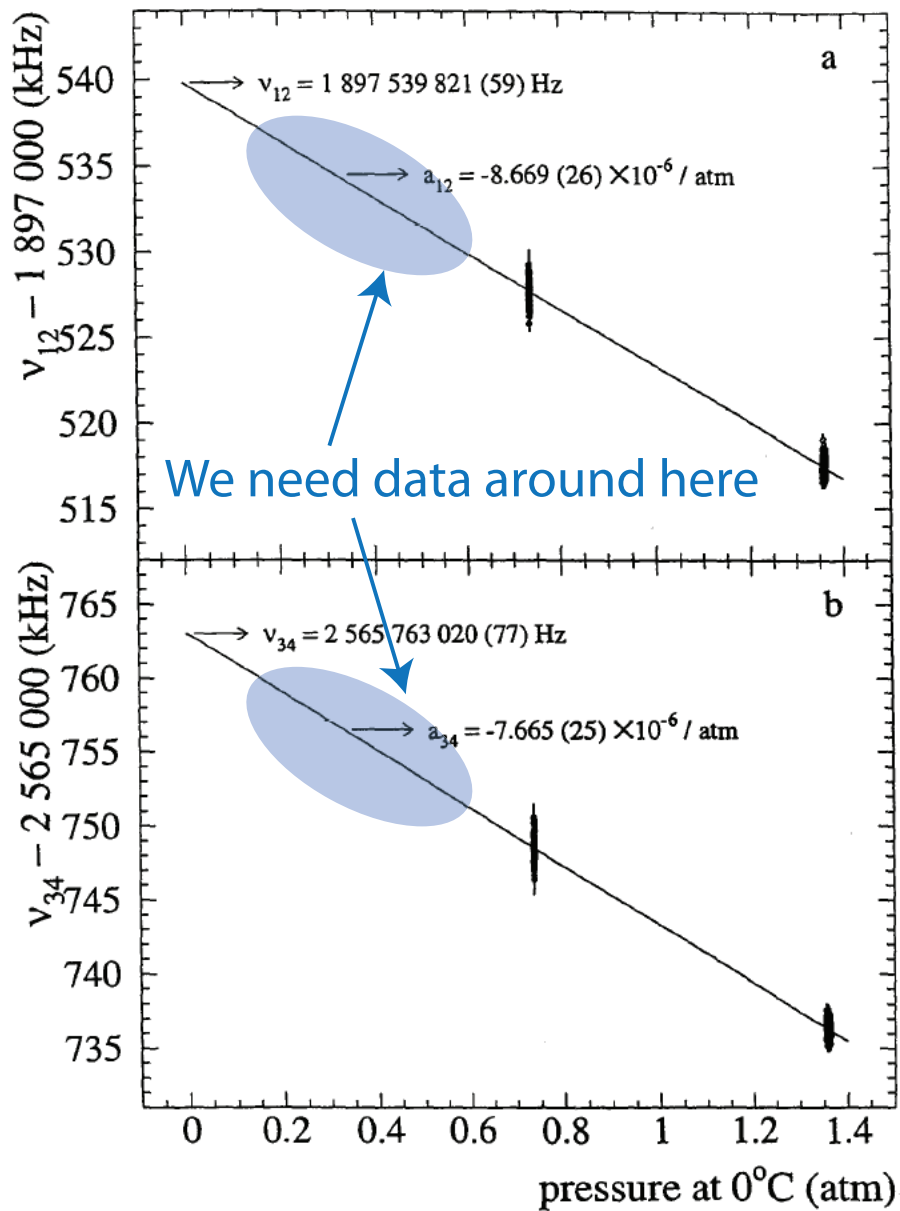


Figure 3.14: A relation between the Kr gas pressure and (a) ν_{12} transition frequency and (b) ν_{34} transition frequency at LAMPF experiment. They were measured at 0.7 atm and 1.8 atm and extrapolate to obtain values at 0 atm. To ensure more accurate extrapolation, measurement at lower pressure is needed [6].

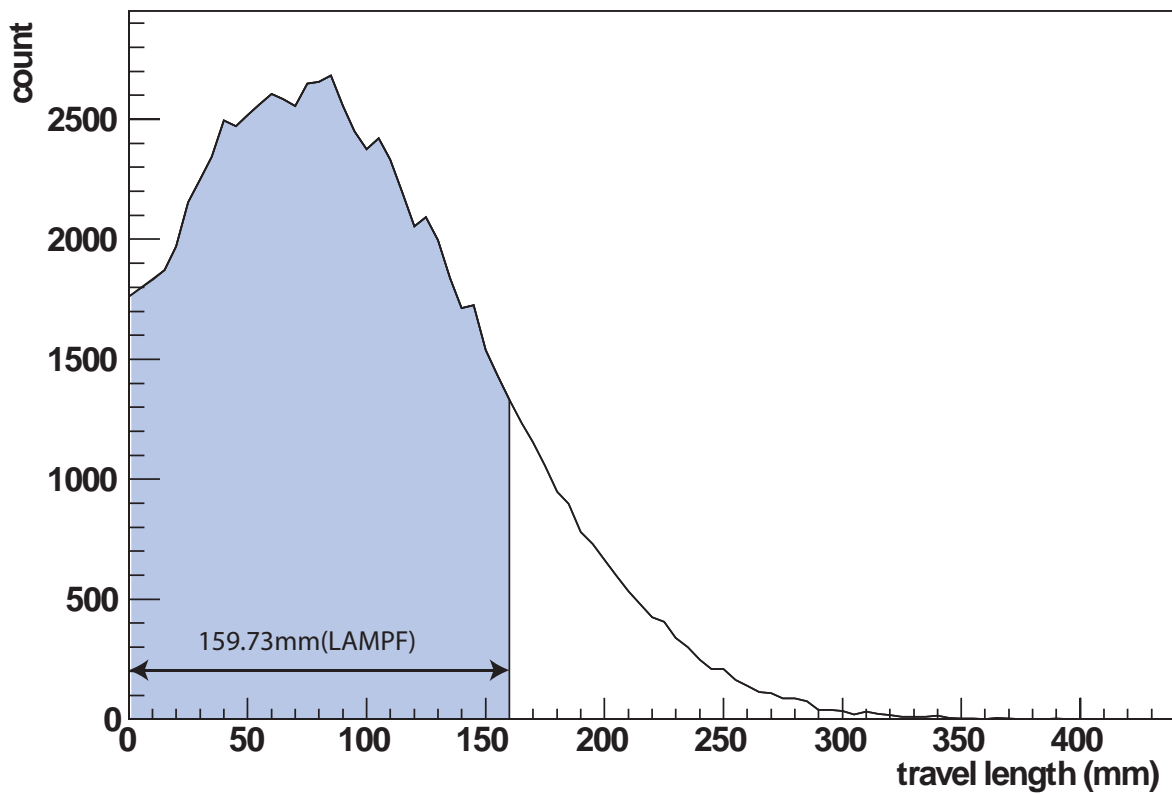


Figure 3.15: A muon stopping distribution in 0.3 atm Kr gas. Trajectories of 100000 muons were simulated by a Monte Carlo simulation program SRIM. The cavity axial length is 159.73 mm designed for the latest experiment at LAMPF. To stop muons in a narrow region, the moderator used had to be thick.

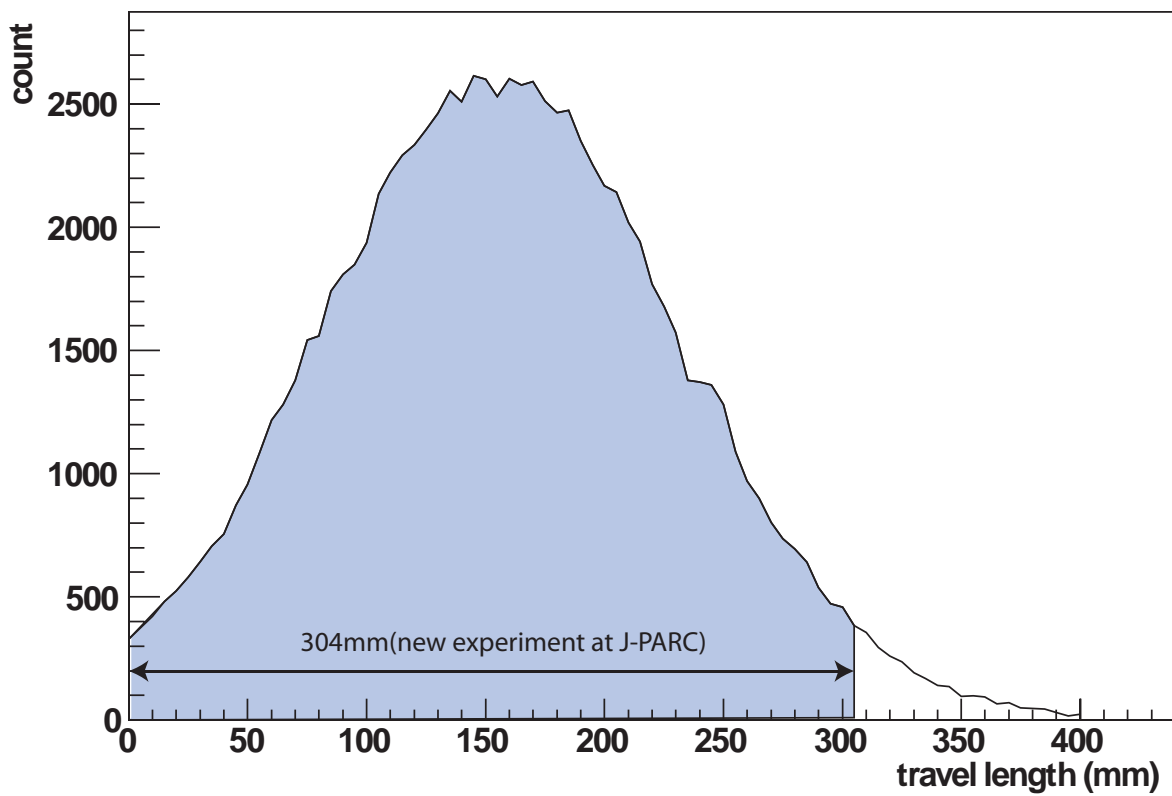


Figure 3.16: A muon stopping distribution in 0.3 atm Kr gas. The cavity axial length is 304 mm designed for a new experiment at J-PARC. The muon stopping distribution is brought within the cavity.

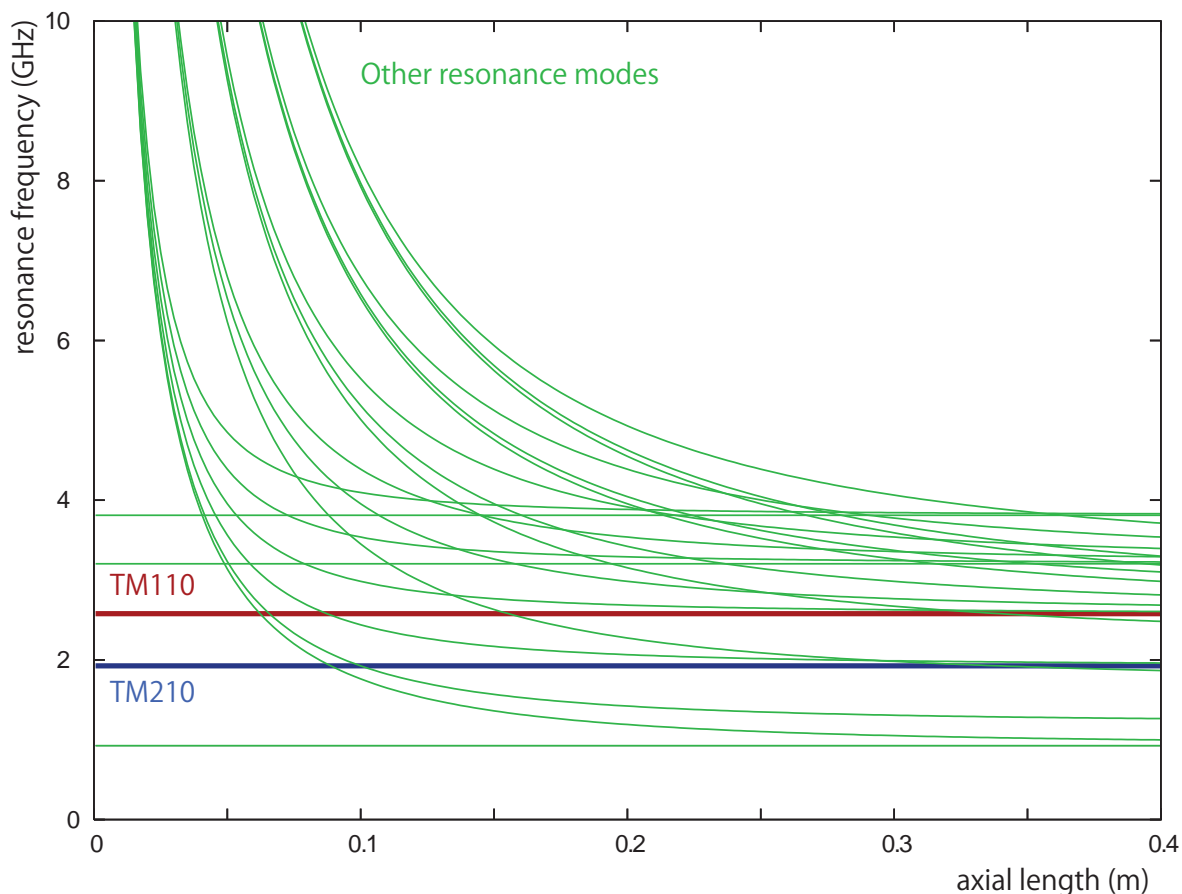


Figure 3.17: Other resonance modes around the mode TM110 and the TM210 mode. Resonance frequencies of the mode TM110 and the TM210 mode does not depend on the cavity axial length. On the other hand, resonance frequencies of many other modes which has nodes in axial direction decrease by axial length of the cavity. In case of the cavity whose axial length is 304 mm, many modes are close to the TM110 mode and the TM210 mode.

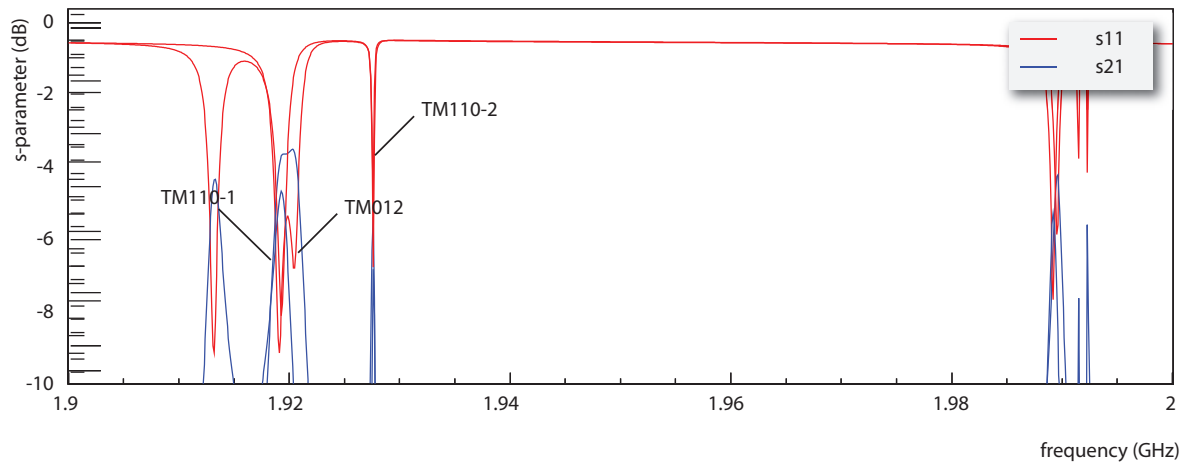


Figure 3.18: Resonance modes near the TM110 modes in which case axial length is 300 mm. A TM012 mode is located between splitted the TM110 modes which is undesirable.

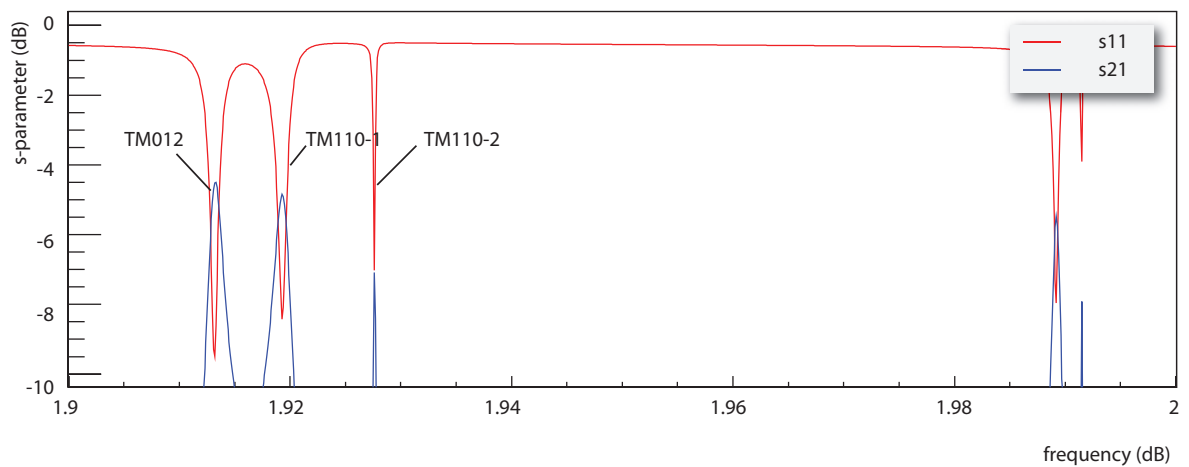


Figure 3.19: Resonance modes near the TM110 modes in which case axial length is 302 mm. Resonance frequency of the TM012 mode is lower than that of a 300 mm cavity. Resonance frequencies of the TM110 modes are not changed because they are independent of cavity length.

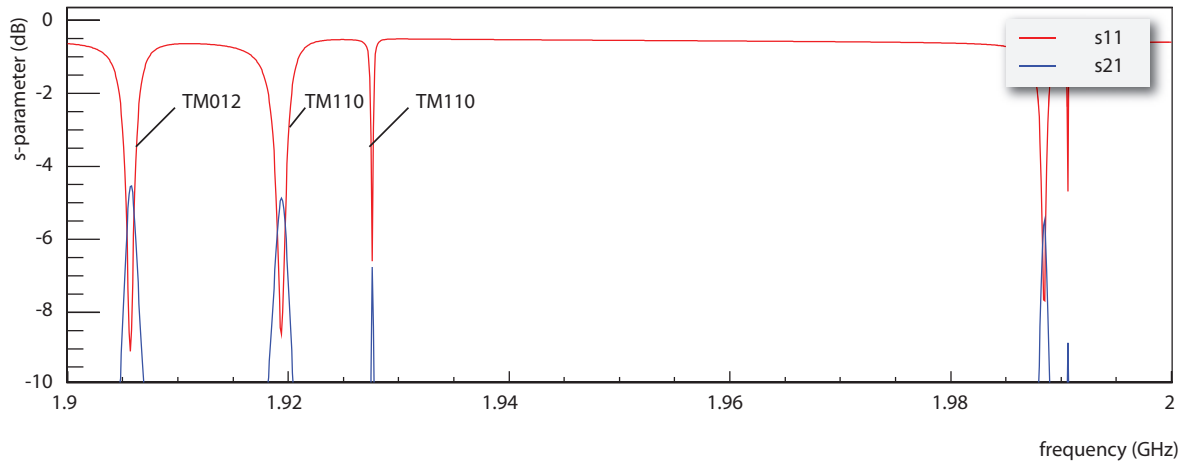


Figure 3.20: Resonance modes near the TM110 modes in which case axial length is 304 mm. Now the TM012 mode is far from the TM110 modes enough to be distinguished.

3.1.5 Foils of the cavity

Muons enter through the front foil of the cavity and the gas chamber, so front foils must be thin not to stop muons. Also back foils must be thin not to stop decay positrons emitted through the back foil. According to Figure 3.21, there are three flanges at the front and back of cavity. Foil is fixed by F2 and F3, and stretched by F1. This foil is a 99.97 % copper, thickness is 25 μm .

3.1.6 Summary of designing the cavity

Figure 3.22 is an outline view of the cavity and Table 3.3 is a summary of the dimension of the cavity. It is situated in the gas chamber and transit muonium by oscillating magnetic field. There are three ports for two RF input loop and one output loop. The resonance frequencies are tuned by two tuning bars. The temperature in the RF cavity is maintained by cooling tube wound around it.

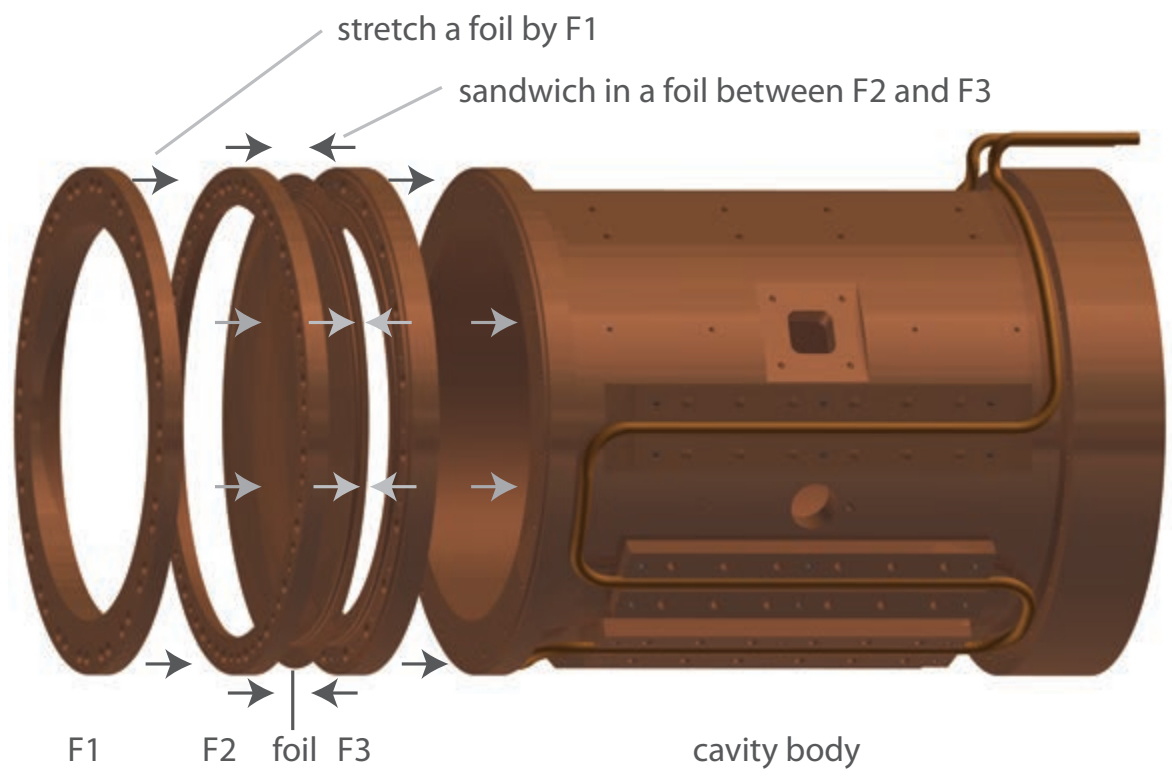


Figure 3.21: How to stretch foils of the cavity. At first, foils are temporary jointed between a F2 and a F3 flanges. Then stretch them again and mount to the cavity by a F1 flange.

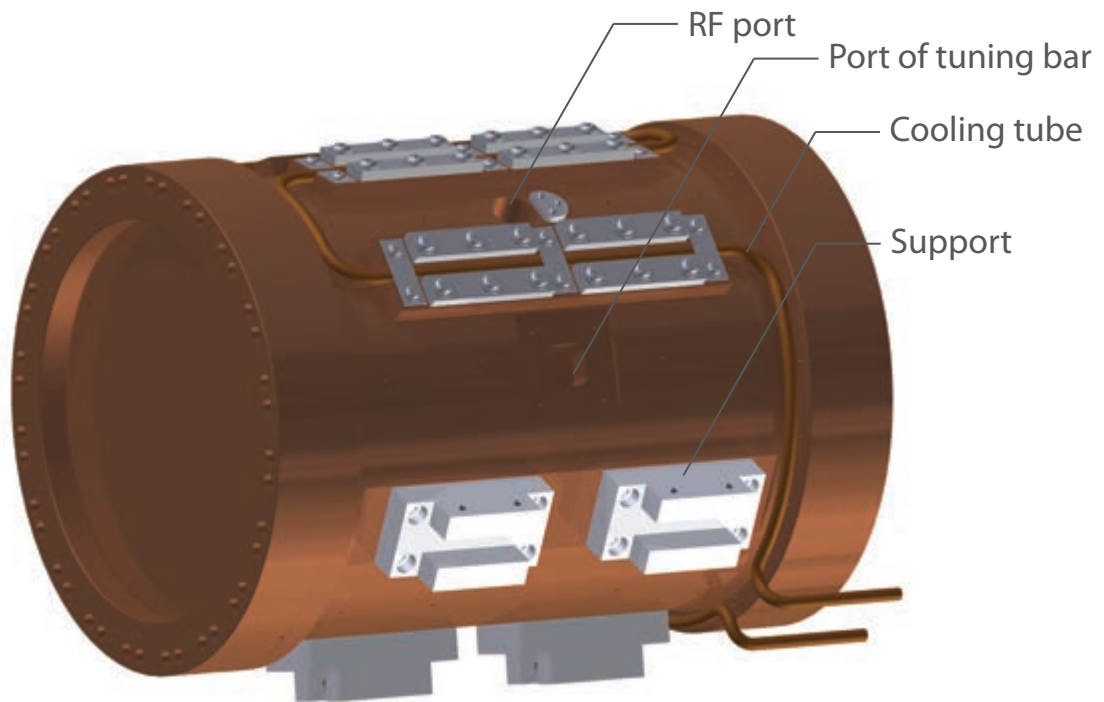


Figure 3.22: An isometric view of the cavity. There are three RF ports and two ports for tuning bars. A cooling tube and a support for being strapped to the gas chamber will be installed.

material	oxygen-free copper
inner diameter	187 mm ϕ
axial length	304 mm
thickness in a radial direction	15 mm
thickness of foil	25 μ m
ports	2 \times for tuning bar
	2 \times for RF input
	1 \times for RF output

Table 3.3: Summary of the dimension of the cavity.

3.2 RF transport

To stabilize the RF power in the cavity is important for designing a RF transport. Figure 3.24 shows a overview of the RF transport under designing. In this section, designing the RF transport: coaxial pipe, feedthrough and antenna is discussed.

3.2.1 Coaxial pipe

WX-20D coaxial pipes are used for delivering RF power. It is made of a oxygen-free copper. TE11 cut off frequency of this pipe is 6.8 GHz which is enough high for our experiments. A coaxial pipe has following advantages.

Rigid

We should care about uncertainty of RF power. To avoid fluctuations of coaxial pipe and antenna, the structure of coaxial pipe and antenna must be rigid.

Compact

Since the space between outer chamber and inner magnet is only ≈ 80 mm, smaller parts for RF transport is required. Figure 3.25 shows a comparison of the dimension between a coaxial pipe and a waveguide. Frequency range of WRI-22 is 1.72–2.61 GHz which is appropriate for the experiment. Since the dimension of a waveguide depends on a wavelength of RF, it is too large to put in the space between outer chamber and inner magnet.

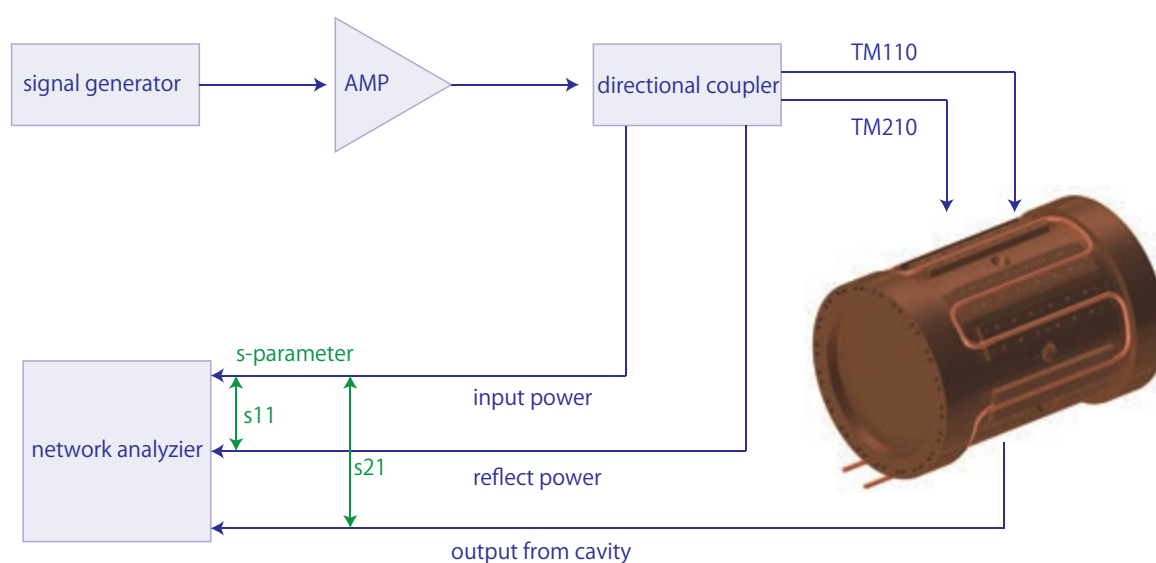


Figure 3.23: A RF system for applied RF to the cavity and monitoring RF power in the cavity.

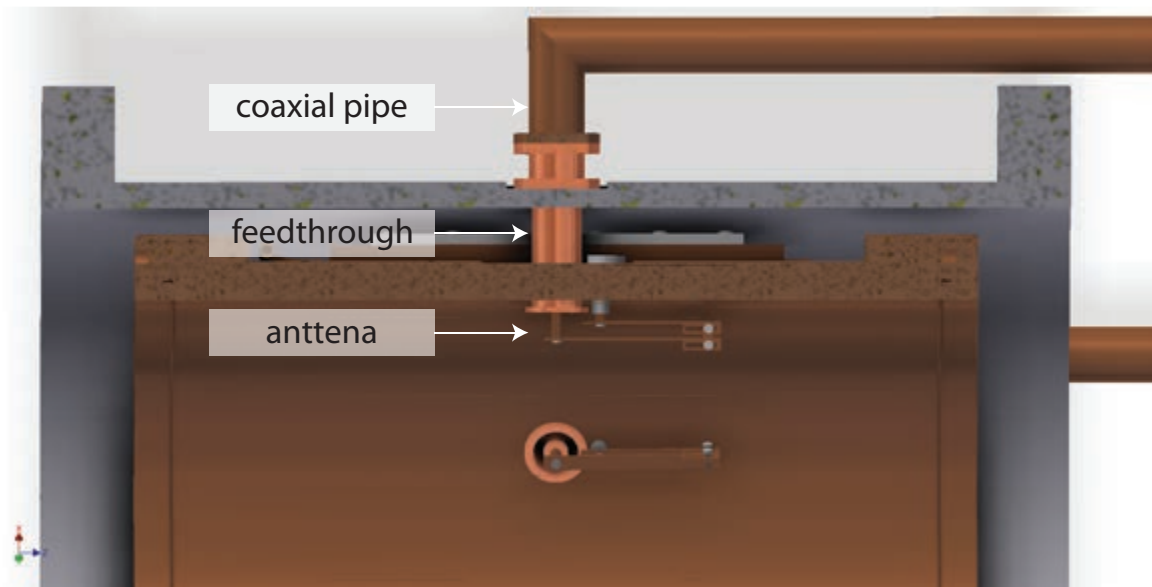


Figure 3.24: A conceptual view of a RF port. the RF power is delivered by coaxial pipes. Kr gas is sealed by feedthrough put between coaxial pipes and antennas. All parts are made of a copper.

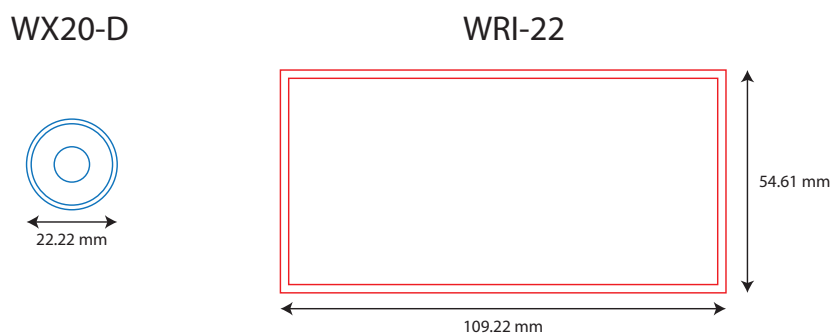


Figure 3.25: A cross-sectional view of a coaxial pipe (WX-20D) and a waveguide (WRI-22). The coaxial pipe is compact compared to the waveguide.

3.2.2 Feedthrough

There are feedthrough windows between coaxial pipe from RF source and gas chamber to seal Kr gas.

3.2.3 Antenna

Antenna is threadably mounted on inner conductor and the inner surface of the cavity. The thickness of the antenna is 7 mm and made of a copper. Coupling with cavity is adjusted by area surrounded by this loop antenna.

3.2.4 RF source

SMF100A Microwave Signal Generator is prepared to transport RF power. A frequency range is 9 KHz to 3 GHz which is enough for requirements of the experiment. A stability of RF frequencies is ensured by Rb oscillation standard. Required RF power is discussed in Appendix D.

3.2.5 Network analyzer

A Network analyzer is used for monitoring a RF power in the cavity. Details of the network analyzer is described in 4.1.1.

3.3 Temperature control

3.3.1 Temperature shifts in the transition frequencies

Temperature shifts in the transition frequencies is caused by collisions with Kr gas. In the case of collision between hydrogen and Argon gas, the shift is expressed as

$$(1/\nu_0)(\delta\nu/\rho) = A + B(T - T_0) \quad (3.11)$$

A and B was obtained at Yale University [55] as

$$A = (-4.800 \pm 0.006) \times 10^{-9} \text{ Torr}^{-1} (0 \text{ }^\circ\text{C}) \quad (3.12)$$

$$B = (+0.956 \pm 0.011) \times 10^{-11} \text{ }^\circ\text{C}^{-1}\text{Torr}^{-1} (0 \text{ }^\circ\text{C}) \quad (3.13)$$

If we can measure the ν_{12} transition at a stable temperature (< 0.1 K), temperature shifts in the transition frequencies will be about a few Hz. Compared to 35 Hz which is uncertainty of ν_{12} transition frequency at LAMPF experiment, it is enough precision. Thus preparing temperature control system with 0.1 K accuracy and stability is needed.

3.3.2 Thermometer

Temperatures in the cavity are measured by type T (Cu-constantan) thermocouples and 4W-RTD (4 wires resistance temperature detector). The accuracy of class AA RTD is $\pm(0.1 + 0.0017|t|)$ K [56], where t °C is a temperature measured. The accuracy of type-T thermocouple is ± 0.35 K.

3.3.3 Cooling tube

One of the matters for the stability of temperature is surface current at the cavity face. Figure 3.26 shows the surface current distribution of the TM110 mode and the TM210 mode. To prevent causing a nonuniformity of gas temperature, temperature of the cavity is stabilized by water flowing around the cavity wall. The water temperature is kept constant within 0.1 K by a water bath. Cooling tube is a 6 mm ϕ copper pipe.

Temperature of water through a cooling tube is kept constant with 0.1 K by water bath.

3.3.4 Control of room temperature

Variation in temperature of a room affects not only the gas temperature but also the stability of magnet. Whole apparatus should be in an environment at a stabilized temperature.

3.4 NMR probe

For monitoring the magnetic field, NMR probes are put in the outer surface of the cavity which will be described in Section 2.4.2.

3.5 Gas chamber

Inner of the cavity should be filled with Kr gas to stop muons and form muonium. Foils at the front and back of the cavity are so thin that it can be bend by pressure difference between

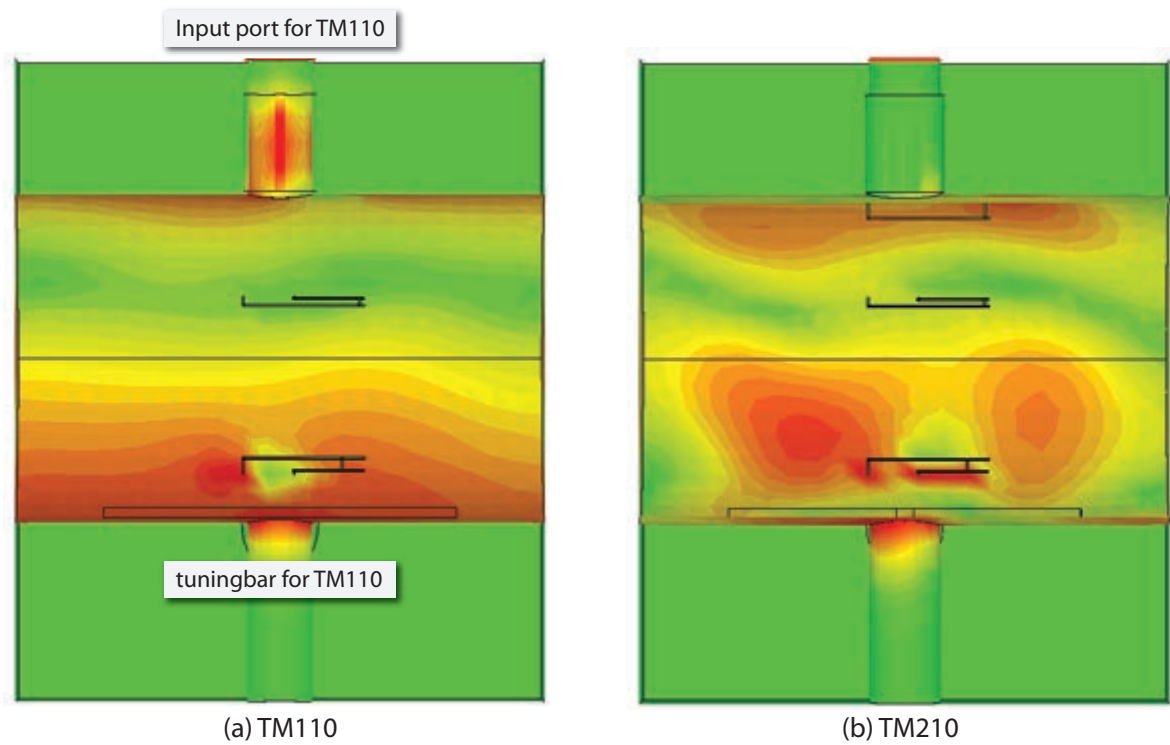


Figure 3.26: Surface currents of the cavity resonated (a) the TM110 and (b) the TM210 modes. Ideally the surface current is independent to the axial direction; however, there is a nonuniformity of the RF field mainly caused by the tuning bars.

pressure inside and outside. It is able to affect RF fields in the cavity. Because of this, the cavity is not able to seal Kr gas and a gas chamber surrounding the cavity is required to keep gas pressure constant.

Figure 3.27 shows a conceptual design of the gas chamber. It is made of a aluminum and has following ports:

- RF inputs and a output,
- cooling tube,
- NMR probes,
- thermometers.

The gas chamber is under designing and will be constructed in 2012.

3.5.1 Purity

In order to avoid chemical reactions and depolarizing collisions, we should carefully take care of the purity of Kr gas. Especially, the cross section for a muonium – O² depolarizing electron spin exchange collision is very large ($\approx 5 \times 10^{-16} \text{ cm}^{-2}$) (see Table 3.4), so O₂ impurity should be 10 ppm or less.

molecule	interaction	σ at 5250G (unit = 10^{-16}cm^2)	σ_{SE} (unit = 10^{-16}cm^2)
NO ₂	NO ₂ + M → NO + OM	≤ 23	...
O ₂	Spin exchange	5.4(3)	5.9(6)
NO	Spin exchange	3.2(2)	7.1(1)
C ₂ H ₄	C ₂ H ₄ + M → C ₂ H ₄ M	0.29(16)	...
H ₂ , N ₂ , SF ₆	...	≥ 0.01	...

Table 3.4: Muonium (M)-molecule cross sections [10, 11].

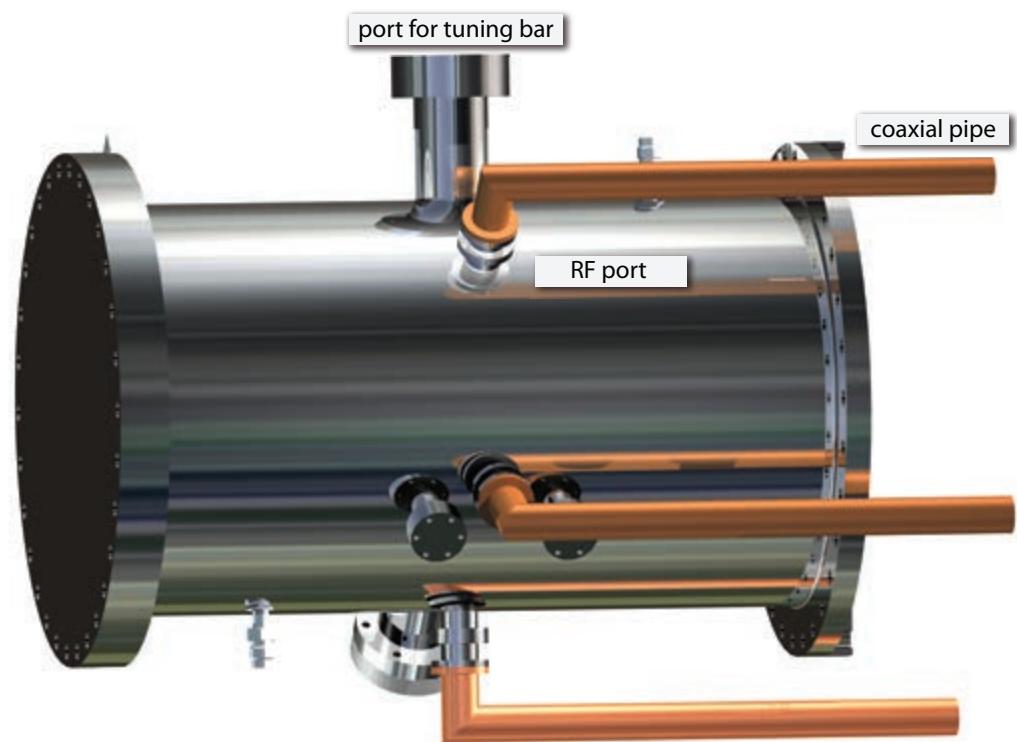


Figure 3.27: A Conceptual design of a gas chamber. It is made of a aluminum and has ports for RF transports and for tuning bars. A gas handling system is under designing.

Chapter 4

Measurement

This chapter describes the measurements of

1. Frequency character of the cavity (Section 4.2),
2. Performance evaluation of tuning bars (Section 4.3).

In this measurement, temperature control system and gas handling system are not installed. Also the RF system is simplified described in Section 4.1.

4.1 RF system for the measurement

4.1.1 Network Analyzer

A network analyzer is used for monitoring RF power in the cavity. It measures a reflecting and transmitting power as S-parameter. We used E5061B Network Analyzer (Agilent Technologies) rent by RIKEN Nishina Center for Accelerator-Based Science. Frequency range of the network analyzer is 5 Hz to 3 GHz which is enough for this measurement. The input power is set to -10 dBm.

S-parameter

The S-parameter of 2-port network is expressed as

$$\begin{pmatrix} b_1 \\ b_2 \end{pmatrix} = \begin{pmatrix} S_{11} & S_{12} \\ S_{21} & S_{22} \end{pmatrix} \begin{pmatrix} a_1 \\ a_2 \end{pmatrix}, \quad (4.1)$$

where a_n is normalized amplitude of incident wave and b_n that of exiting wave defined as

$$a_i = \frac{V_{Ii}}{\sqrt{Z_R}}, \quad (4.2)$$

$$b_i = \frac{V_{Ri}}{\sqrt{Z_R}}. \quad (4.3)$$

where V_{Ii} is a voltage wave incident on each port, V_{Ri} is a voltage wave reflected from each port and Z_R is a reference impedance. In most cases including this network analyzer, the reference impedance is set to 50Ω .

S_{mn} represent

- S_{11} : reflection coefficient of input port,
- S_{12} : reverse voltage gain,
- S_{21} : forward voltage gain,
- S_{22} : reflection coefficient of output port.

The measurement using network analyzer takes two steps. At first, input antennas should be tuned for resonance frequencies. It is taken as synonymous with that an input impedance is equivalent to reference impedance at resonance frequencies. Using Equation 4.1, 4.2 and 4.3, the cavity impedance is described as

$$Z_I = Z_R \frac{1 + S_{11}}{(1 - S_{11})}, \quad (4.4)$$

where Z_I is a input impedance and Z_R is a reference impedance. Thus coupling of input port is able to confirmed by S_{11} .

Secondly, RF power in the cavity is monitored S_{21} by RF input and output ports. RF power in the cavity is usually expressed as a Q factor which is described in Section 4.1.1. When a input port couple to the cavity, the Q factor of the cavity is equivalent to Q_{ext} which is described in Section 4.1.1 [57]. Thus RF power in the cavity can be monitored by S_{21} .

Quality factor

Q factor is defined by two ways: in terms of the ratio of the energy and in terms of bandwidth.

Defined in terms of the ratio of the energy

RF energy stored in the cavity is expressed by a Quality factor (Q factor). It is defined as

$$Q = \frac{\omega_0 W}{P}, \quad (4.5)$$

where ω_0 is the resonance frequency, W is the energy stored in the cavity and P is the energy loss rate per unit time from the cavity. Designing the high Q cavity is same meaning as minimization of power losses in the cavity.

There are several types of Q factors:

- unloaded Q (Q_0),
- conductive Q (Q_c),
- external Q (Q_{ext}),
- dielectric Q (Q_d),
- loaded Q (Q_L).

where Q_c is result from the power loss in the walls which have finite conductivity. The absorbed power due to surface losses is calculated as

$$P_c = \frac{1}{2} \sqrt{\frac{\pi \mu f}{\sigma}} \int |H|^2 \partial S, \quad (4.6)$$

where σ is the surface current density and f is the resonance frequency. Since the dominant part of the P_c is from the surface current flow between the components of the cavity, joint strength of them is important for high Q factor.

Q_{ext} is result from power loss through unclosed surfaces (holes) of the cavity. In case of our cavity, there are RF input and output ports and the ports for tuning bars as unclosed surfaces. To avoid the power loss, coupling of the input port which transports RF power should be strong, but the coupling of other RF ports should be weak and the size of the ports for tuning bars should be small as far as possible.

Q_d is result from the power loss in the lossy dielectric material which is described as

$$P_d = \pi f \tan \delta \epsilon_0 \epsilon_r \int |E|^2 \partial V, \quad (4.7)$$

where ϵ_0 is the vacuum permittivity, ϵ_r is the electric permittivity and $\tan \delta$ is the dielectric tangent (see Section 3.1.3). This equation indicates that the power loss caused by the dielectric

material depends on the dielectric tangent, the electric permittivity and the volume of the material. Since the sweep range of the tuning bar depends electric permittivity and the volume the material but not the dielectric tangent, a material which has low dielectric tangent is good for Q factor.

Unloaded Q (Q_0) which is contained Q_d and Q_c but excluded Q_{ext} can be found as

$$\frac{1}{Q_0} = \frac{1}{Q_c} + \frac{1}{Q_d} \quad [49]. \quad (4.8)$$

Loaded Q (Q_L) contained all parts of Q factor can be found as

$$\frac{1}{Q_L} = \frac{1}{Q_c} + \frac{1}{Q_{ext}} \quad [49]. \quad (4.9)$$

Thus the energy loss in the cavity is caused by the combination of the surface current on the cavity, microwave absorption by the dielectric material and the power loss through unclosed surfaces of the cavity.

Defined in terms of bandwidth

The other common definition of the Q factor is in terms of bandwidth. RF cavity can be regarded as a parallel RLC circuit. A voltage of the parallel RLC circuit is expressed as

$$V(t) = \frac{1}{[R^{-2} + (\omega C - 1/(\omega L))^2]^{1/2}} \exp j(\omega t - \phi). \quad (4.10)$$

P is defined as

$$P = \frac{V^2}{R}. \quad (4.11)$$

According to 4.10 and 4.11,

$$P = \frac{1}{2} \frac{RV^2}{R^2 + (\omega L - 1/(\omega C))^2}. \quad (4.12)$$

When the consumption energy P is equivalent to half of consumption energy at the resonance point, the following equation holds;

$$\frac{RV^2}{2(R^2 + (\omega L - 1/(\omega C))^2)} = \frac{V^2}{4R}. \quad (4.13)$$

FWHM (full width at half maximum) $\Delta\omega$ is calculated by ω_1 and ω_2 satisfy 4.13,

$$\Delta\omega = \omega_2 - \omega_1 \quad (4.14)$$

$$= \sqrt{C/LR}\omega_0 = \frac{\omega_0}{Q}. \quad (4.15)$$

Thus Q factor also expresses a FWHM of a RF cavity. As mentioned Section 4.1.1, Q_L of the cavity is equivalent to Q_{ext} when the cavity and a input port is coupled. The reason is that main part of Q_{ext} is result from the output port, Q_L is able to obtained by a FWHM of a S_{21} .

Table 4.1 and 4.2 show a result of calculation of Q factor of the TM110 mode and the TM210 mode by CST microwave studio. In this simulation, the main part of the power losses is caused by surface current of the cavity.

	Loss/W (peak)	Q
Q_{ext}	1.19×10^5	2.04×10^5
Q_c	7.19×10^5	3.75×10^4
Q_d	5.17×10^5	4.72×10^5
Q_L	8.21×10^4	2.97×10^4

Table 4.1: Q factor of the TM110 mode. Loss of Q is caused by surface current at the cavity face and loss tangent of tuning bar.

	Loss/W (peak)	Q
Q_{ext}	9.71×10^4	3.32×10^5
Q_c	7.19×10^5	4.48×10^4
Q_d	3.00×10^5	1.07×10^5
Q_L	1.12×10^6	2.89×10^4

Table 4.2: Q factor of the TM210 mode. Loss of Q is caused by surface current at the cavity face and loss tangent of tuning bar.

Calibration of Network Analyzer

Network analyzer can be plagued by three types of errors:

1. Systematic errors,
2. Random errors,
3. Drift errors.

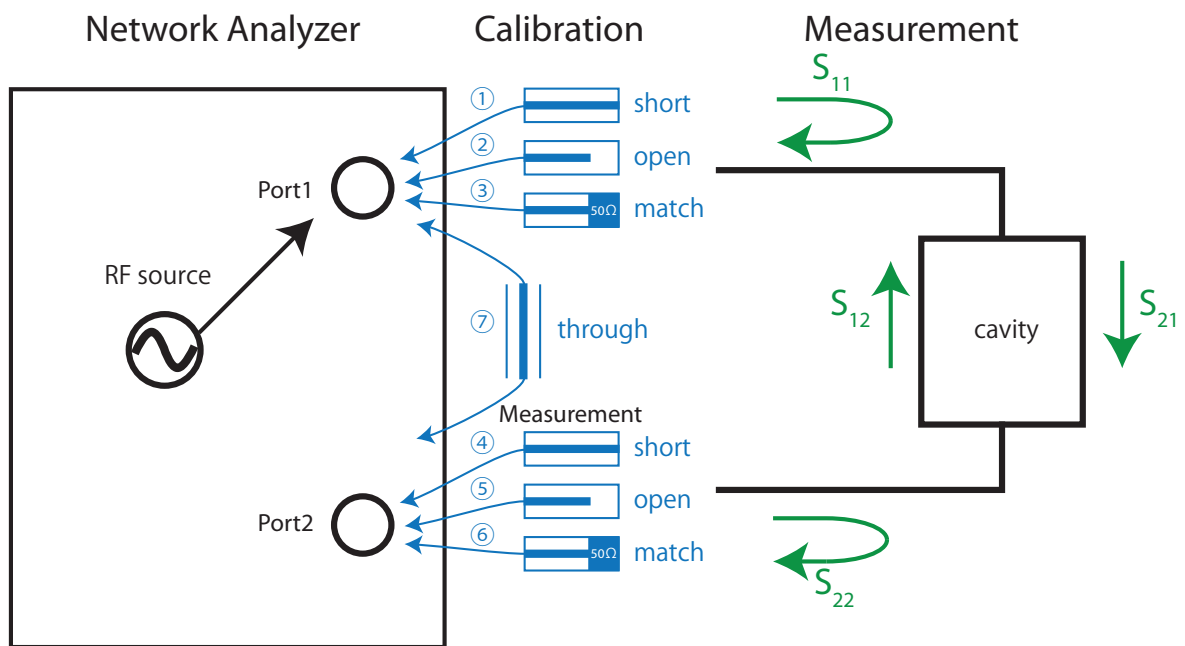


Figure 4.1: A process of TOSM calibration and the measurement of S-parameter using the network analyzer.

And there are 6 types of systematic error:

1. Directivity and crosstalk errors relating to signal leakage ,
2. Source and load impedance mismatches relating to reflections,
3. Frequency response errors caused by reflection and transmission tracking within the test receivers.

For preventing these errors, network analyzer should be calibrated each time measuring condition is changed. Random errors vary randomly as a function of time. Main contributor is noises of instruments. It is not solved by calibration. Drift errors occur mainly by variation of temperature and can be reduced by constant recalibration.

TOSM (Through-Open-Short-Match) calibration is a typical type of calibration to determine the 6 systematic error terms for each signal direction. It measures the open, short, and match one port standard on both ports and the through between them (see Figure 4.1).

1. Open: Transmission line terminated with open. A reflected voltage keeps in phase with a incident voltage.
2. Short: Transmission line terminated with short. A reflected voltage is opposite phase with a incident voltage.
3. Match: Transmission line terminated with reference impedance. All the incident power is absorbed in the load.
4. Through: Transmission line connected port1 and port2 directly. Through is calibrate a amplitude and phase variation of transmission characteristic.

4.1.2 RF ports

In this measurement, coaxial cables are used as substitute for coaxial pipes. Cables are connected to the network analyzer by N connector and to the cavity by SMA connector using converters. Antennas are used a 0.9mm ϕ enameled round copper wire jointed to outer conductor by crimping terminal and solder-mounted to inner conductor. Figure 4.2 are photographs of each RF antenna. Coupling of ports is determined by a planar dimension of loops. Area of input loops is tuned near the 7cm² which is optimum value in simulation. On the other hand, output loop is made as small as possible not to coupled strongly.

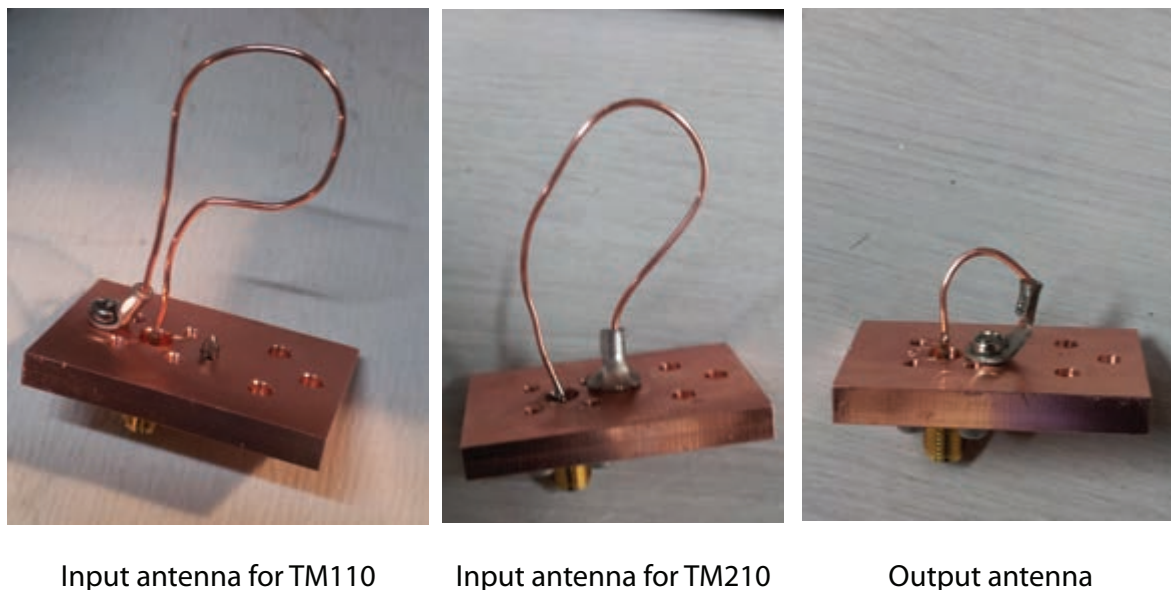


Figure 4.2: A photograph of RF antennas for the measurement.

4.2 Frequency character of the cavity

A characteristic of the cavity without tuning bars is measured. At first, resonance frequencies of the TM₁₁₀ mode and the TM₂₁₀ mode are determined by S_{11} and obtained Q factor of each mode by S_{21} (see Section 4.1.1). Figure 4.3 shows a resonance line shape near the TM₁₁₀ mode. A red arrow indicates the resonance frequencies of the TM₁₁₀ mode in the measurement. Figure 4.4 is a closeup of Figure 4.3. These peaks are determined as the TM₁₁₀ mode by the reason that there should be two degenerated TM₁₁₀ modes. The TM₁₁₀-1 mode is coupled input port for TM₁₁₀ strongly and the the TM₁₁₀-2 mode is coupled weakly as mentioned in 3.1.3. In addition to this, the TM₁₁₀-1 mode should be affected strongly by tuning bar for TM₁₁₀ than the TM₁₁₀-2 mode. This confirmation is described in Section 4.3.

Thus the resonance frequencies of the TM₁₁₀ modes are 1.9532 GHz (TM₁₁₀-1) and 1.9541 GHz (TM₁₁₀-2) in the measurement. It is slightly different from the value obtained by 3.1, 1.9553 GHz. This is because the cavity contained ports for RF antenna and for tuning

bars is not perfect cylinder.

Figure 4.5 shows a resonance line shape nearby the TM210 mode. The determination of the TM210 mode is by same reasons as that of the TM110 mode. The resonance frequencies of the TM210 modes are 2.6423 GHz (TM210-1) and 2.6455 GHz (TM210-2) in the measurement. It is also slightly different from the value obtained by 3.1, 2.6207 GHz.

4.3 Performance evaluation of tuning bars

For performance evaluation of tuning bars,

- define the relationship between displacement of tuning bars and resonance frequencies of the TM110 mode and the TM210 mode (see Section 4.3.2),
- check the difference between several types of tuning bars (see Section 4.3.3).

4.3.1 Q factor of the cavity with tuning bars

Q factor of the cavity was measured in case of the alumina (99.6 %) tuning bar (20 mm × 100 mm × 5 mm) is used (see Figure 4.10). Q factor of the TM110-1 mode is about 8000 and of the TM210-1 mode is about 4000 obtained from FWHM of S_{21} parameter (see Table 4.3.2). These values are far less than the Q factors estimated by the simulation.

One of main possible causes of the Q factor depression is a coupling with input antennas. As mentioned Section 4.1.1, Q_L of the cavity is equivalent to Q_{ext} when the cavity and the input port is coupled. The peak of the S_{11} of the TM110-1 mode is only -15 dB. In this case, 3 % of the RF power is reflected. On the other hand, the peak of the S_{11} of the TM210-1 mode is only -2 dB so that about 63 % of RF power is reflected to the input port. Thus it is not able to said that Q_L is equivalent to Q_{ext} , and optimization of the antennas is needed to estimate accurate Q factor.

modes	Q (in the measurement)	Q (in the simulation)
TM110-1	8000	2.97×10^4
TM210-1	4000	2.89×10^4

Table 4.3: Comparison of Q factor between in the measurmeent and in the simulation.

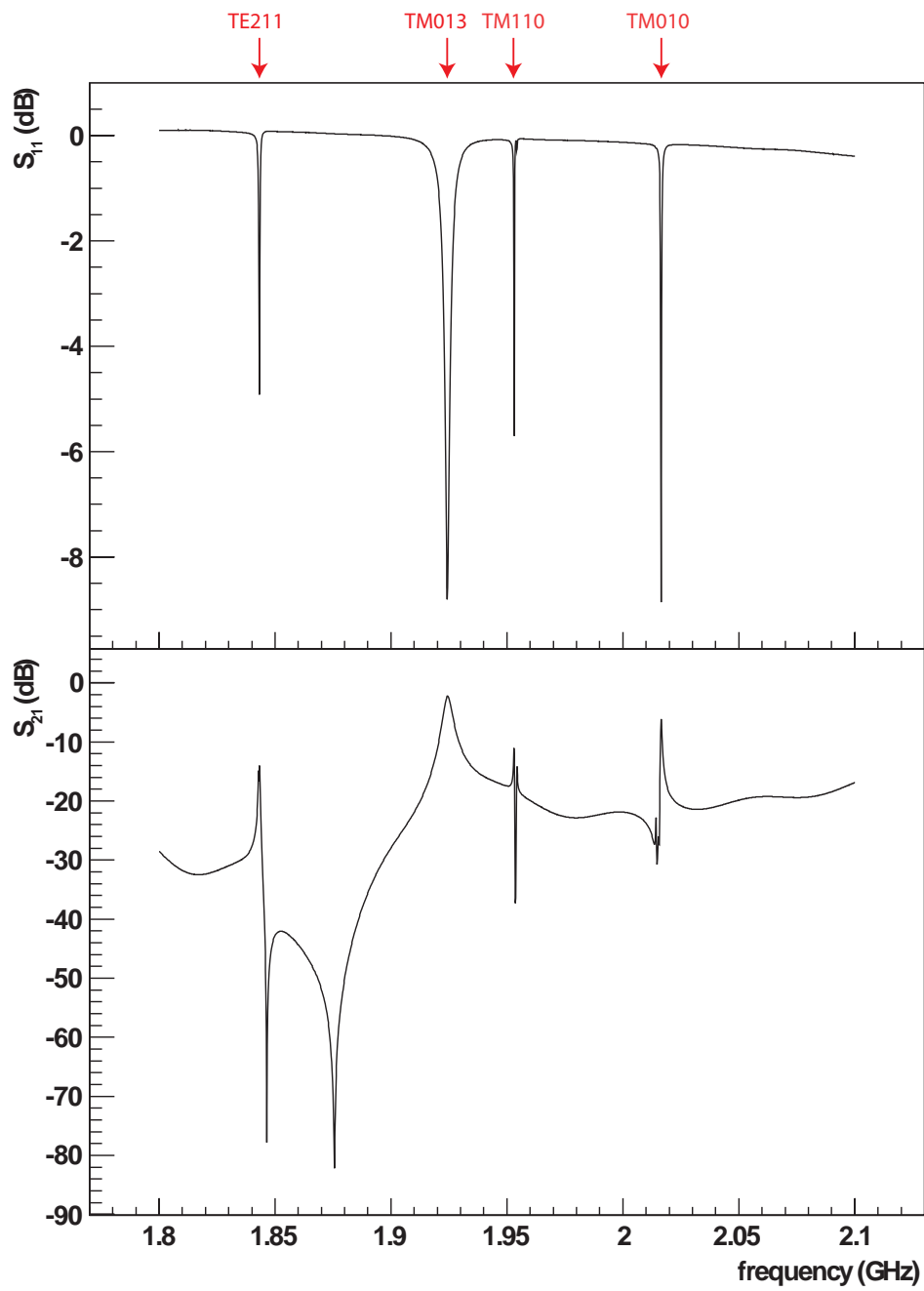


Figure 4.3: (a) S_{11} near the TM110 modes by the measurement. The red arrows show resonance frequencies of each mode. (b) S_{21} by the measurement.

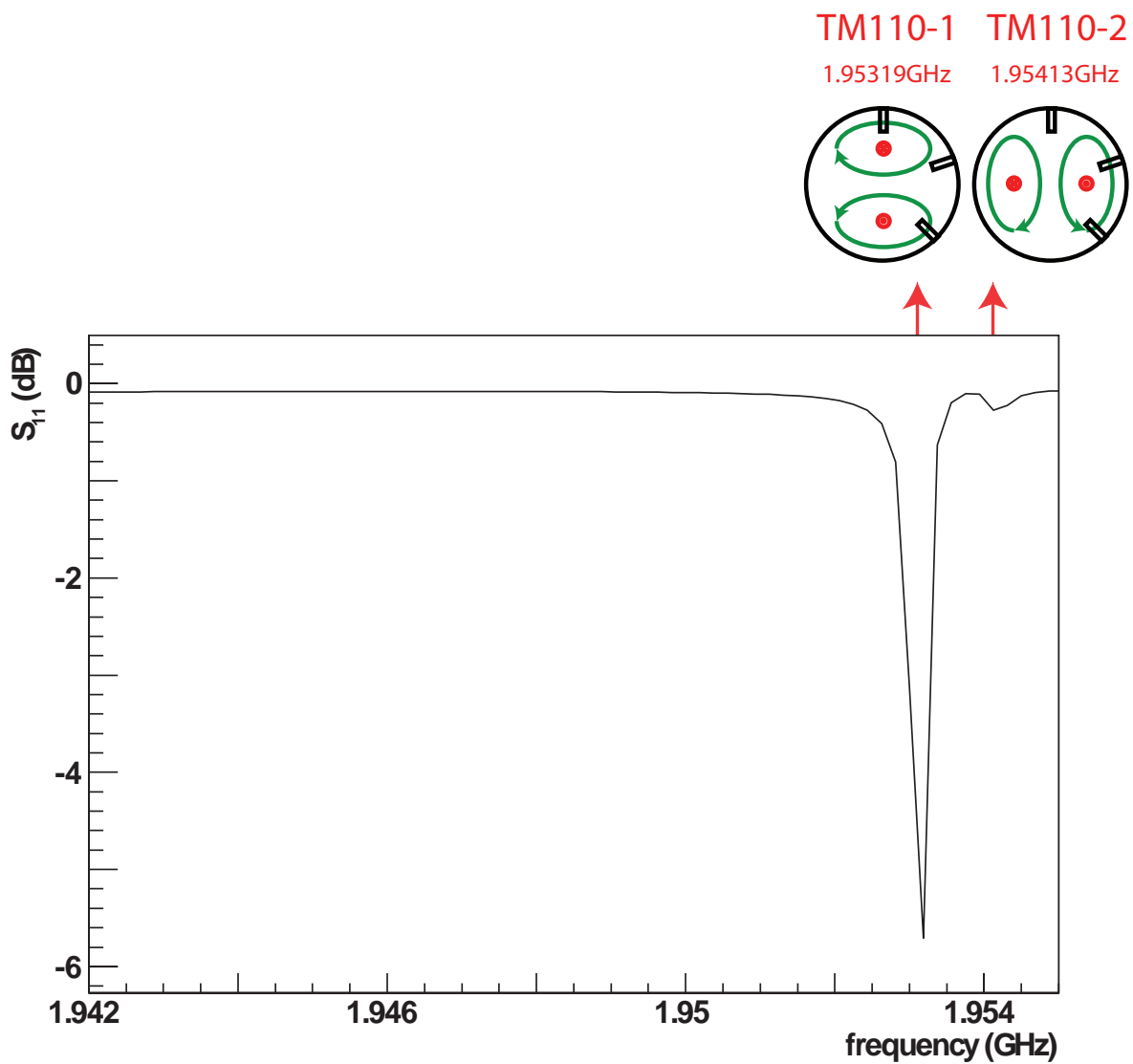


Figure 4.4: A Closeup of Figure 4.3 (a). The red arrows show resonance frequencies of the TM₁₁₀ modes.

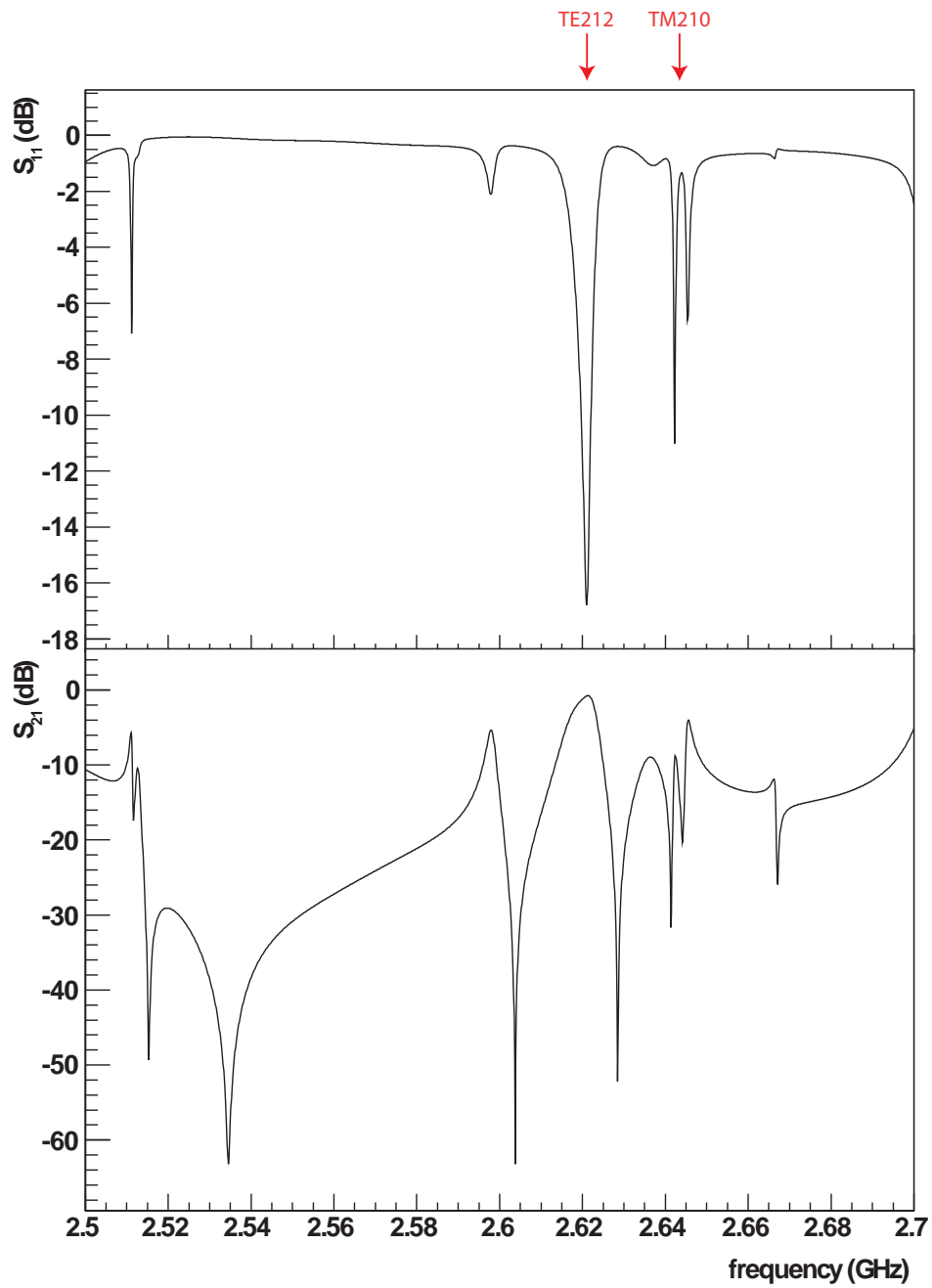


Figure 4.5: (a) S_{11} near the TM210 modes by the measurement. The red arrows show resonance frequencies of each mode. (b) S_{21} by the measurement.

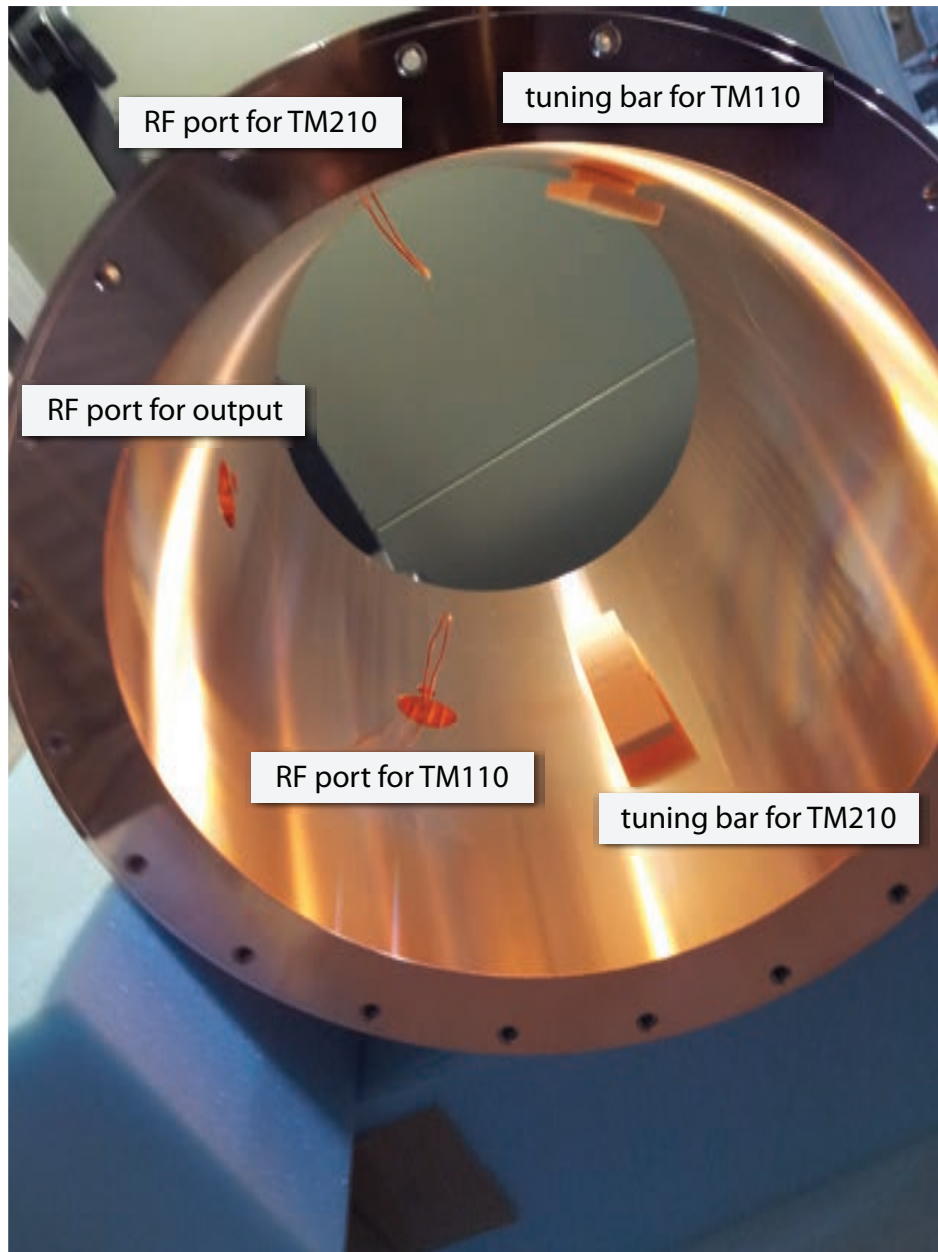


Figure 4.6: A photograph of inner view of the cavity. The RF antennas and the tuning bars are installed.

4.3.2 Relationship between displacement of tuning bars and resonance frequencies

Figure 4.7 and 4.8 show resonance frequency sweeps of the TM110 mode and the TM210 mode. The sweep range of the TM110 mode by the tuning bar1 is 1.948 GHz to 1.934 GHz and that of the TM210 mode is 2.608 GHz to 2.537 GHz. The sweep ranges in the measurement are larger than in the simulation. One of the possible reasons is the difference of geometry. In the simulation, coaxial pipes and rigid antennas which are under designing for the muonium HFS measurement are used, while coaxial cables and thin copper wire antennas are used in this measurement.

Figure 4.9 shows a TM110 resonance frequency sweep by the tuning bar for TM210 which is not used for sweeping the TM110 mode originally. Unlike in the case of using the tuning bar for TM110, the TM110-2 resonance frequency slightly varies with the displacement. This is because the position relationship between the tuning bar and the electric field of TM110-2 is different from the case of using the tuning bar for TM110 (see Figure 3.10). Since the TM110-1 resonance frequency also sweep by the tuning bar for TM210, the sweep range can be larger than using only the tuning bar for TM110.

4.3.3 Difference between several types of tuning bars

Figure 4.10 shows three tuning bars to compare performance. Tuning bar2 is the double long of tuning bar1 and tuning bar3 is the half thickness of the tuning bar1.

Figure 4.11 shows resonance frequency sweeps of the TM110-1 mode by three tuning bars. As mentioned Section 4.1.1, a sweep range is defined by volume of the tuning bar. In addition to this, displacement of tuning bar is defined as a length between inner surface of the cavity and that of tuning bar, a thick tuning bar is inserted deeply at the same displacement. Therefore, the sweep range of tuning bar3 is shorter than other bars and the line shape of tuning bar2 is parallel to the that of tuning bar1. Figure 4.12 shows a same relation of the TM210-1 mode. Since the RF field of the TM210 mode rotates on axis of the cavity (see Figure 4.13), the parallel relationship of the line shape of tuning bar1 and tuning bar2 is not kept.

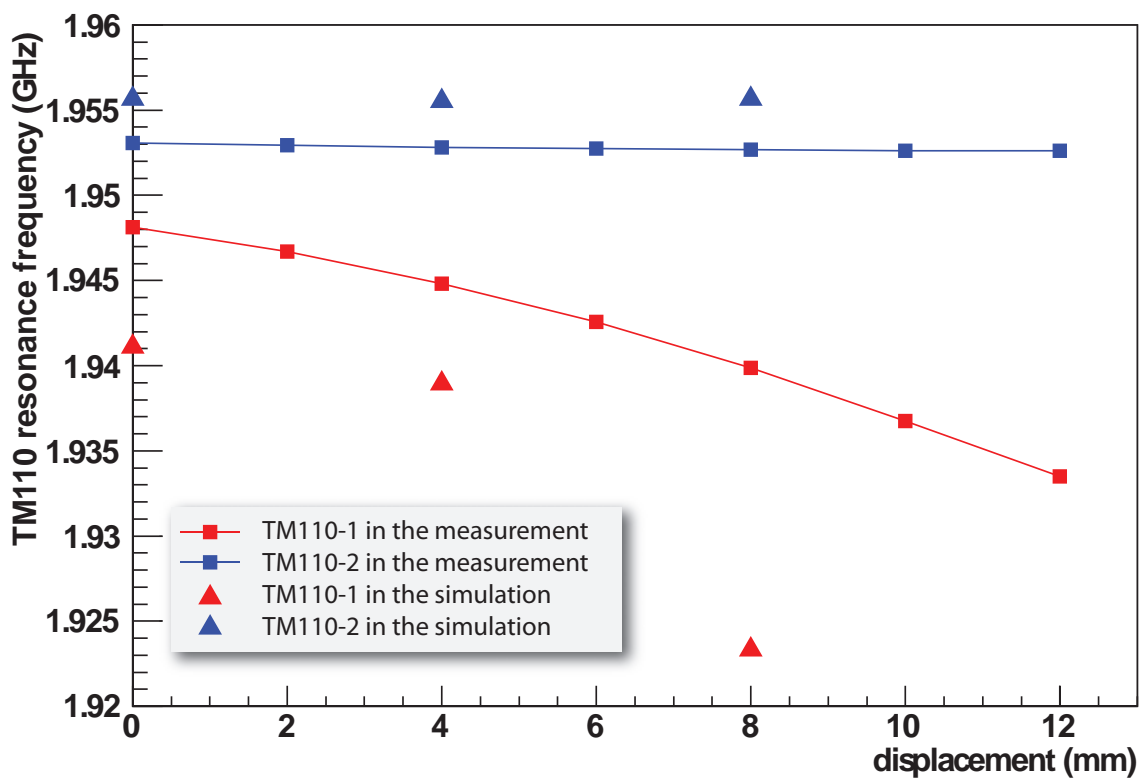


Figure 4.7: A TM110 resonance frequency sweep by the tuning bar for TM110. Square markers are the values obtained in the measurement and triangle markers are the values obtained in the simulation. Red one is a that of the TM110-1 mode and blue one is a that of the TM110-2 mode.

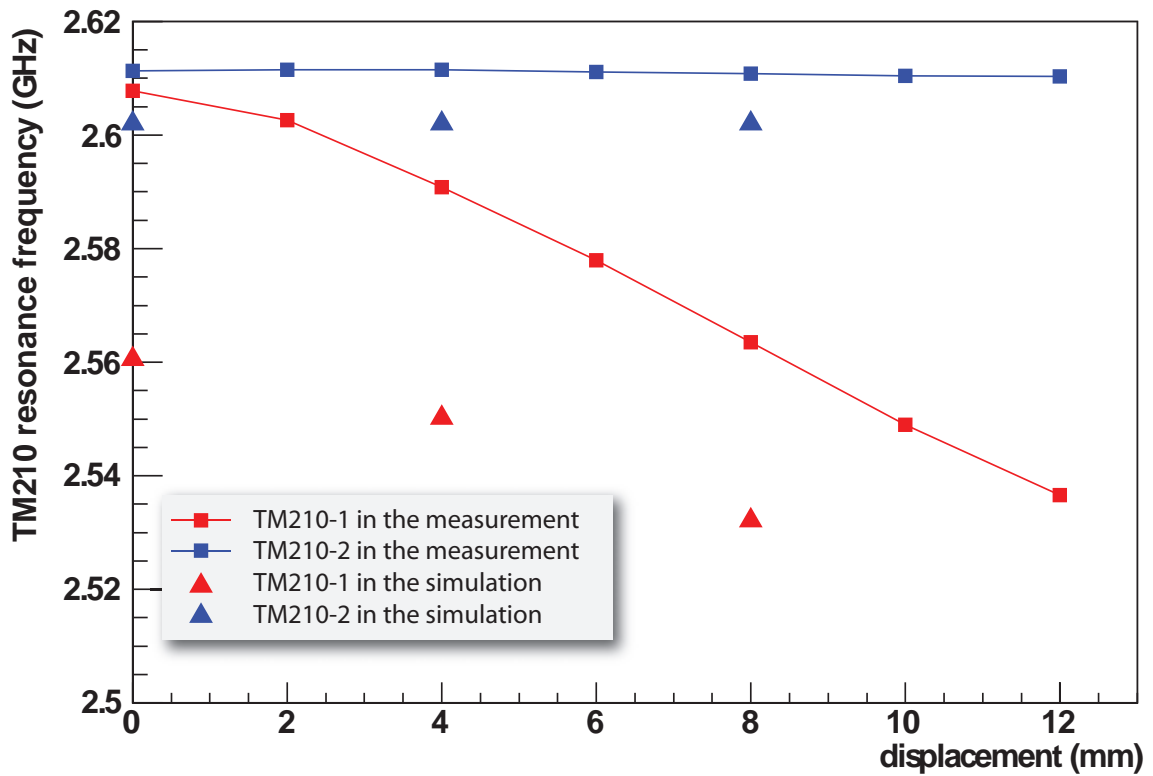


Figure 4.8: A TM210 resonance frequency sweep by the tuning bar for TM210. Square markers are the values obtained in the measurement and triangle markers are the values obtained in the simulation. Red one is a that of TM210-1 and blue one is a that of TM210-2.

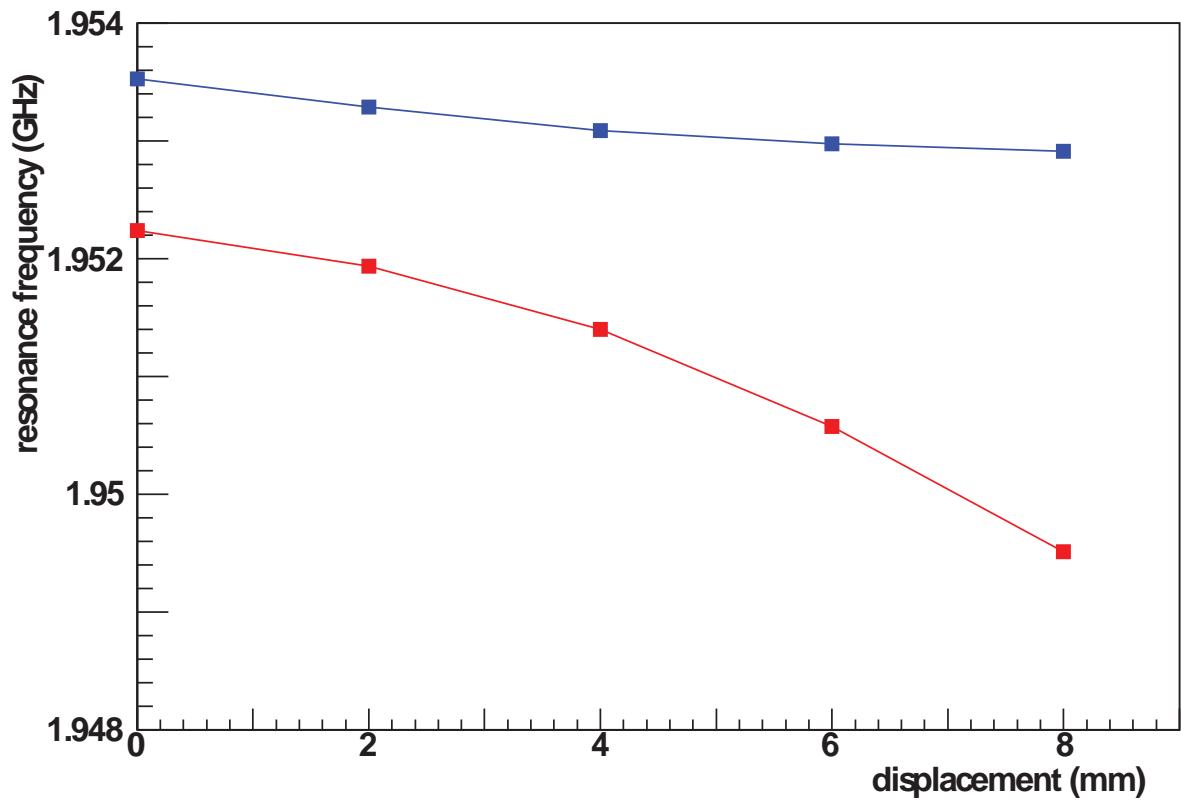


Figure 4.9: A TM110 resonance frequency sweep by the tuning bar for TM210. Red one is a that of TM210-1 and blue one is a that of TM210-2.

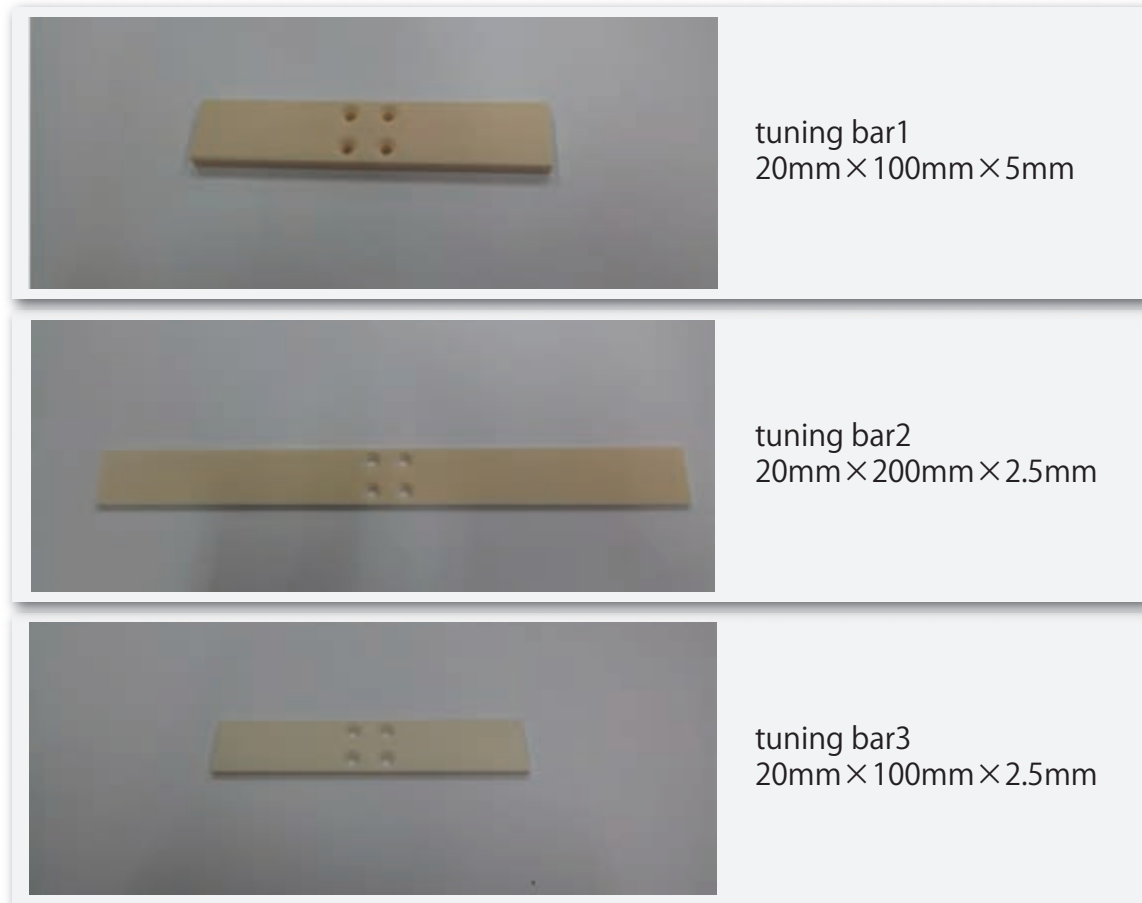


Figure 4.10: Three tuning bars are used for this measurement. The sweep range of tuning bar3 is shorter than other bars and the line shape of tuning bar2 is parallel to the that of tuning bar1.

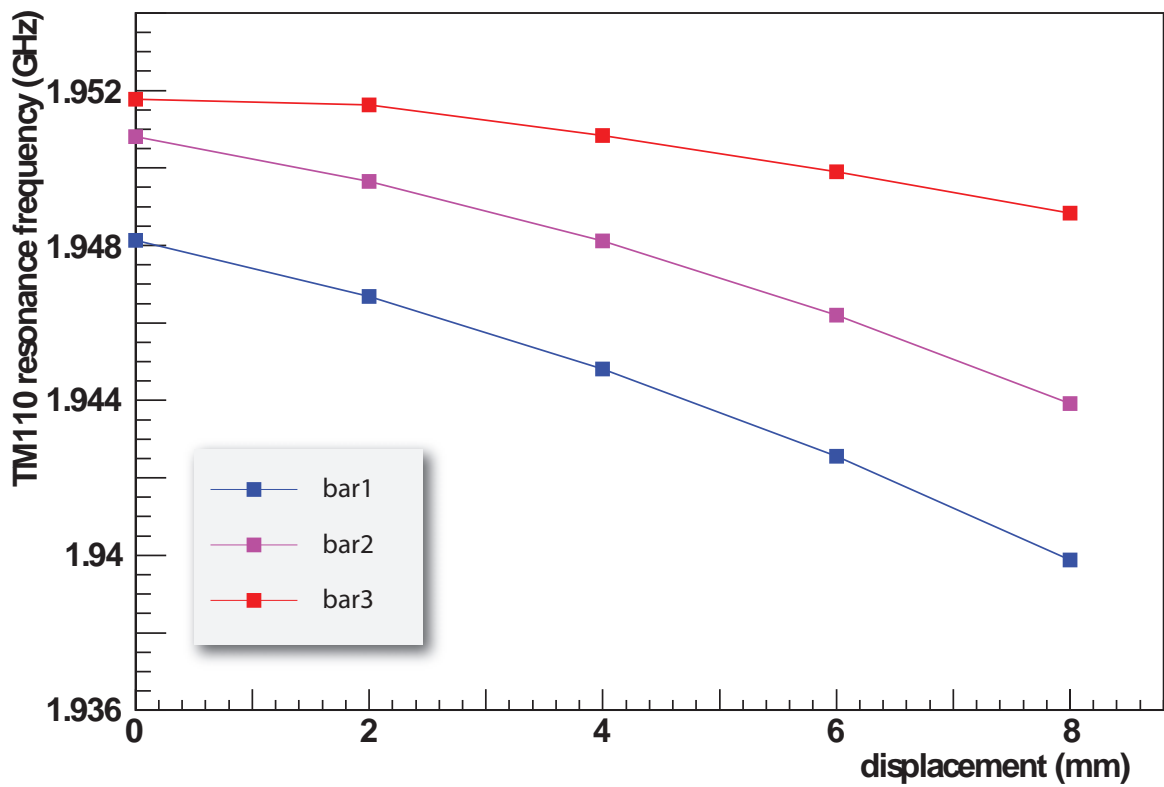


Figure 4.11: A difference of sweep range of the TM110 mode between several tuningbars.

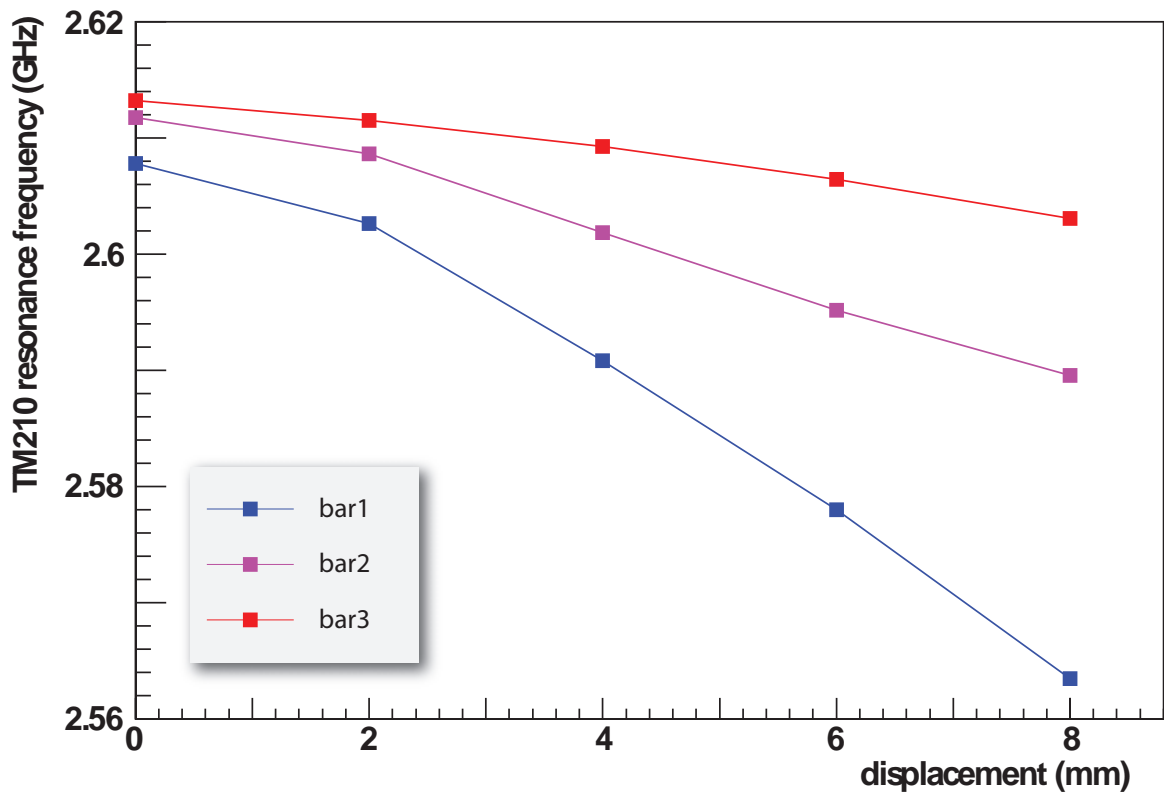


Figure 4.12: A difference of sweep range of TM210 mode between several tuningbars. the parallel relationship of the line shape of tuning bar1 and tuning bar2 is not kept.

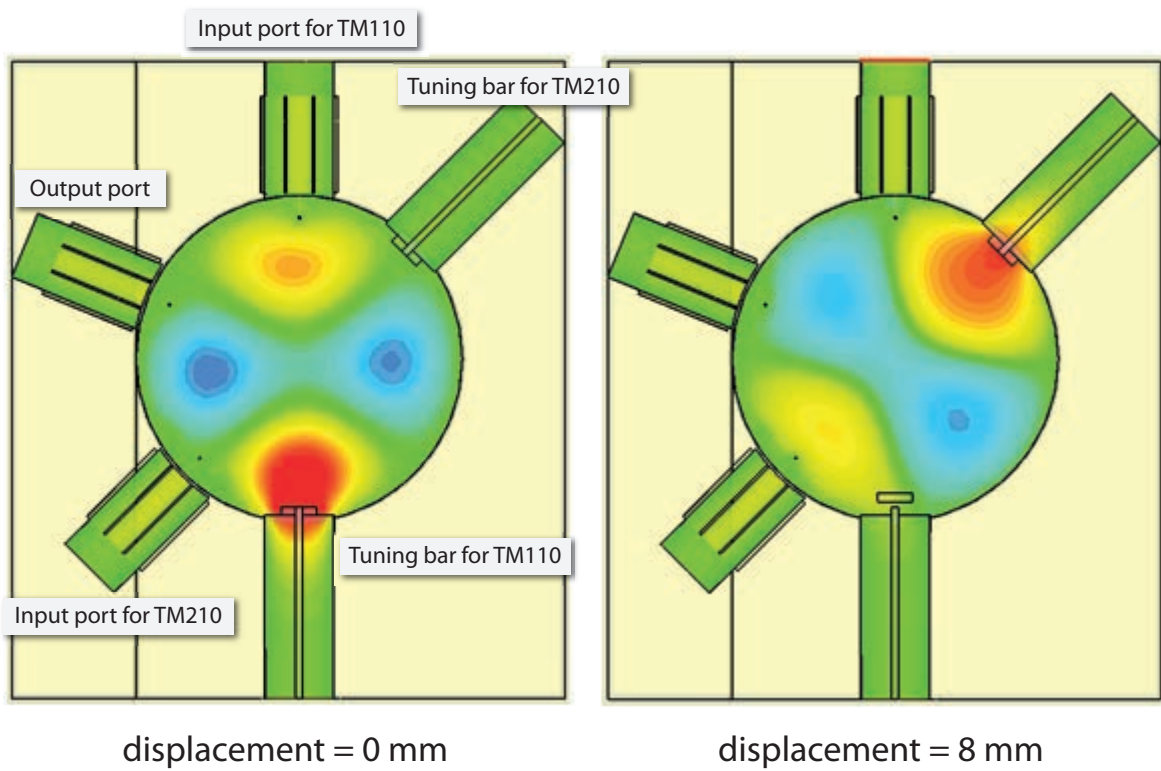


Figure 4.13: A cross-sectional view of the electric fields of the TM₂₁₀ mode. The RF field is rotates on axis of the cavity by inserting the tuning bar.

Chapter 5

Discussion

5.1 Improvement of the uniformity of RF fields

The sweep range of the TM110 mode by tuning bar1 is 1.948 GHz to 1.934 GHz and that of the TM210 mode by tuning bar2 is 2.608 GHz to 2.537 GHz (see Figure 4.7 and 4.8). Compared to transition frequencies of ν_{12} and ν_{34} (see Equation 3.2 and 3.3), transition frequency of ν_{34} is in the sweep range while ν_{12} is out of the range. To reach both transition frequencies, some improvements are needed. Moreover, about 10 mm displacement is needed to reach transition frequencies in the case of ν_{34} . It is not good for uniformity of RF fields. This section describes improvement of the sweep range and uniformity of RF fields.

5.1.1 Widen inner diameter of the cavity

A possible improvement of sweep range is moving the resonance frequencies of the cavity close to the transition frequencies. It is possible by changing the diameter of the cavity. The thickness of the cavity is 15 mm and it is possible to widen inner diameter by several millimeter. Figure 5.1 and 5.2 show relations between diameter of the cavity and the resonance frequencies of the TM110 mode and the TM210 mode by the simulation. The red line shows a resonance frequency without tuning bars and the blue line shows a one with tuning bars (20 mm \times 100 mm \times 5 mm) placed at origin. Since inserting the tuning bar decrease a resonance frequency, the resonance frequencies when tuning bars are placed at origin should be higher than the transition frequencies. Therefore, by widen the diameter of the cavity, the resonance frequencies are close to the transition frequencies. However, there are gaps

between in the simulation and the measurement (see Figure 4.7 and 4.8). To determine the length to be widen, more accurate estimation by simulation is needed.

Widen the diameter of the cavity is also able to contribute the uniformity of RF field. If the resonance frequencies are close to transition frequencies, smaller tuning bars or smaller displacement of the tuning bars are sufficient to reach the transition frequencies (Also the distance between the tuning bars and inner surface of the cavity at the origin point defined as 5 mm are able to be closer by changing the size of the tuning bar supports.) Since the tuning bars mainly cause the nonuniformity of the RF field, this optimization acts as a improvement of uniformity of RF field.

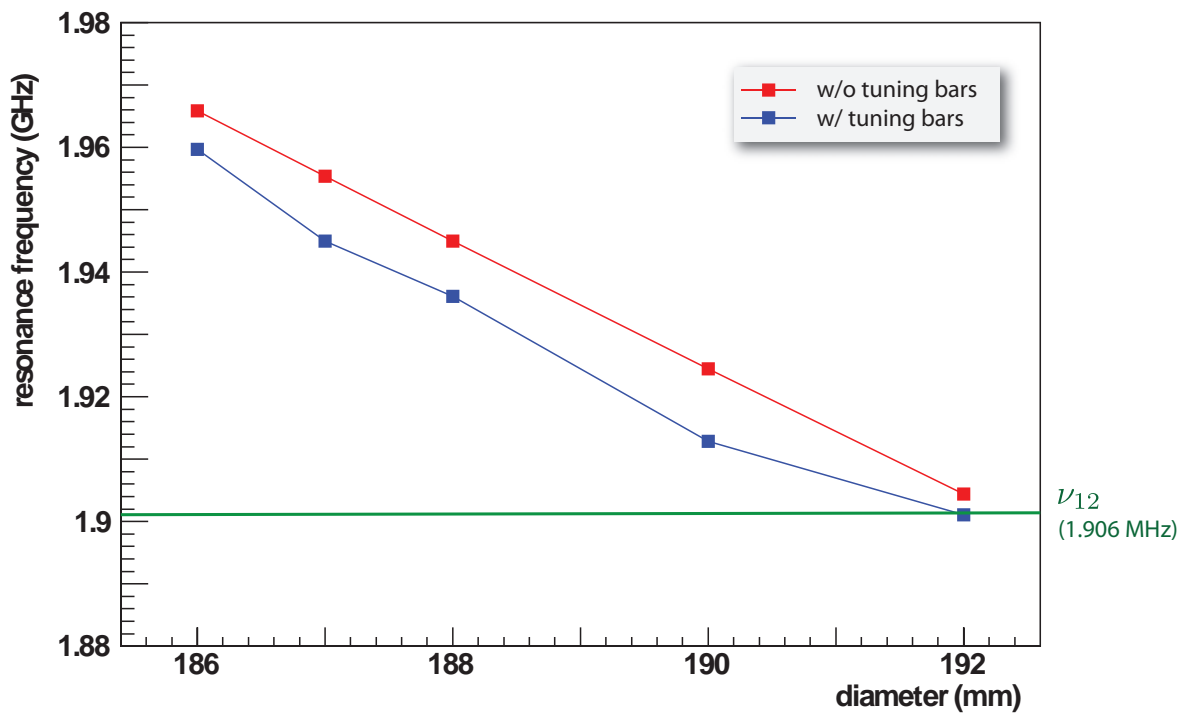


Figure 5.1: A relation between the diameter of the cavity and the resonance frequency of the TM110 mode by simulation. The red line shows a resonance frequency without tuning bars and the blue line shows a with tuning bars put are placed at origin. The green line is the ν_{34} transition frequency.

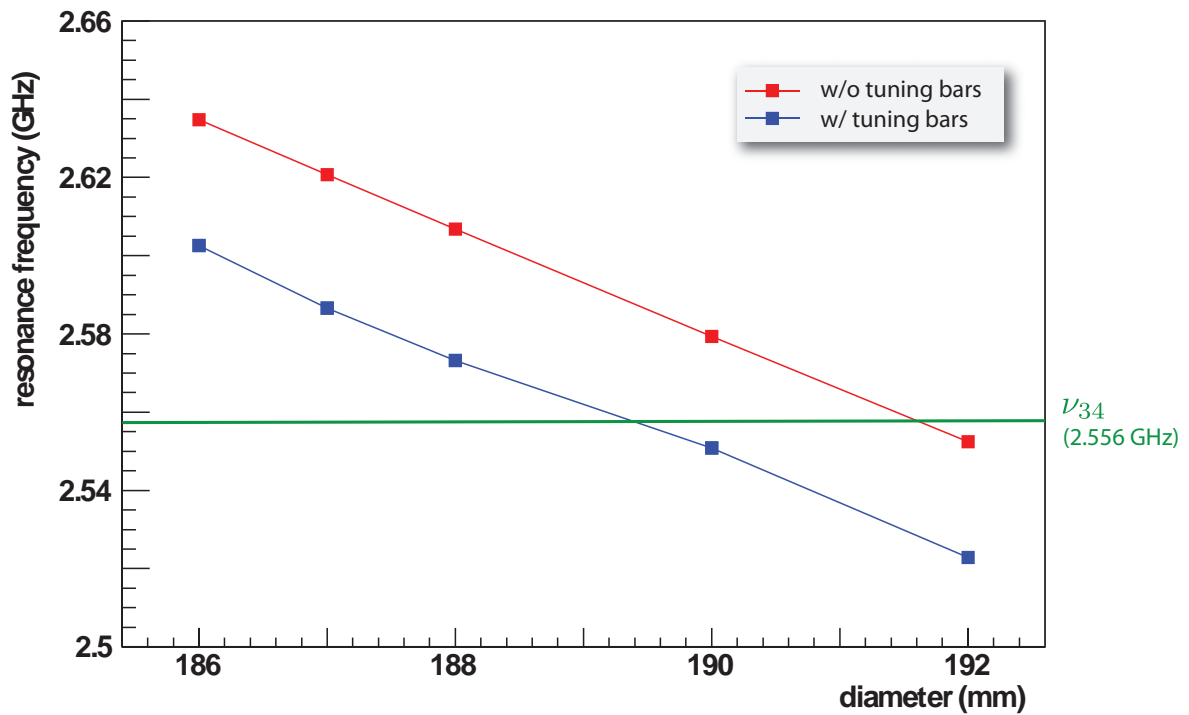


Figure 5.2: A relation between the diameter of the cavity and the resonance frequency of the TM₂₁₀ mode by simulation. The red line shows a resonance frequency without tuning bars and the blue line shows a with tuning bars are placed at origin. The green line is the ν_{34} transition frequency.

5.1.2 Optimization of the shape of tuning bars

Optimization of the shape of the tuning bars is also related to the uniformity of RF fields. Figure 5.3 shows a comparison of electric fields of the TM₁₁₀ mode between tuning bar1 and tuning bar2. Since length of the tuning bar1 is one-third of cavity length, the electric field with tuning bar1 has two nodes on the axis. Thus there is a difference from shape of the tuning bar at same volume and displacement, large but thin tuning bar is better for uniformity of RF field.

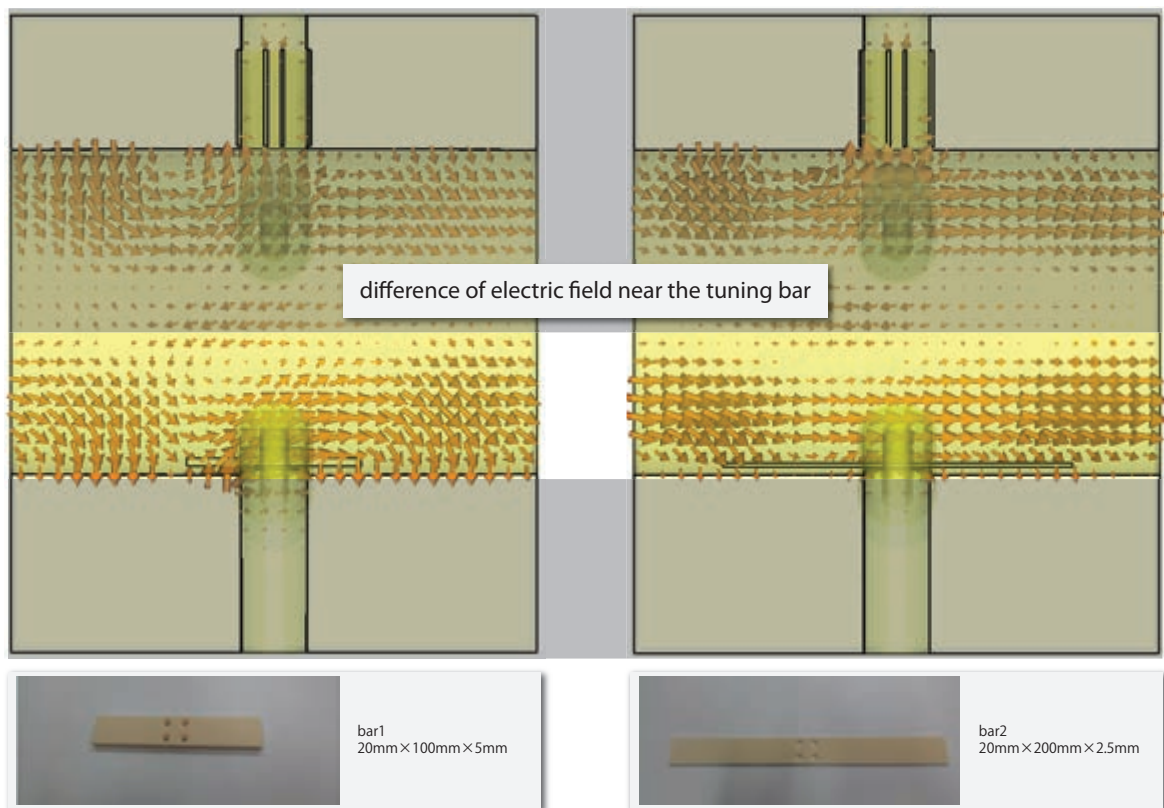


Figure 5.3: A difference of RF field of TM₂₁₀ mode between tuning bar1 and tuning bar2.

5.2 Schedule of development of the cavity

The cavity and the gas chamber should be ready until starting of the experiment. There are following improvements and developments remained.

Improvement of the cavity

As mentioned in Section 5.1, redesigning of the cavity is required In order to optimize the sweep range and for uniformity of RF field.

Temperature control system

For stability of a temperature in the cavity, cooling tube and thermometer should be ready (see Section 3.3).

Gas handling

In order to seal Kr gas at the outer side of the cavity, the gas chamber should be ready (see Section 3.5).

5.3 Schedule of muonium HFS experiment

Figure 5.4 shows the schedule of preparation of apparatus for this experiment. Whole apparatus are ready and we can start the experiment until the end of 2012.

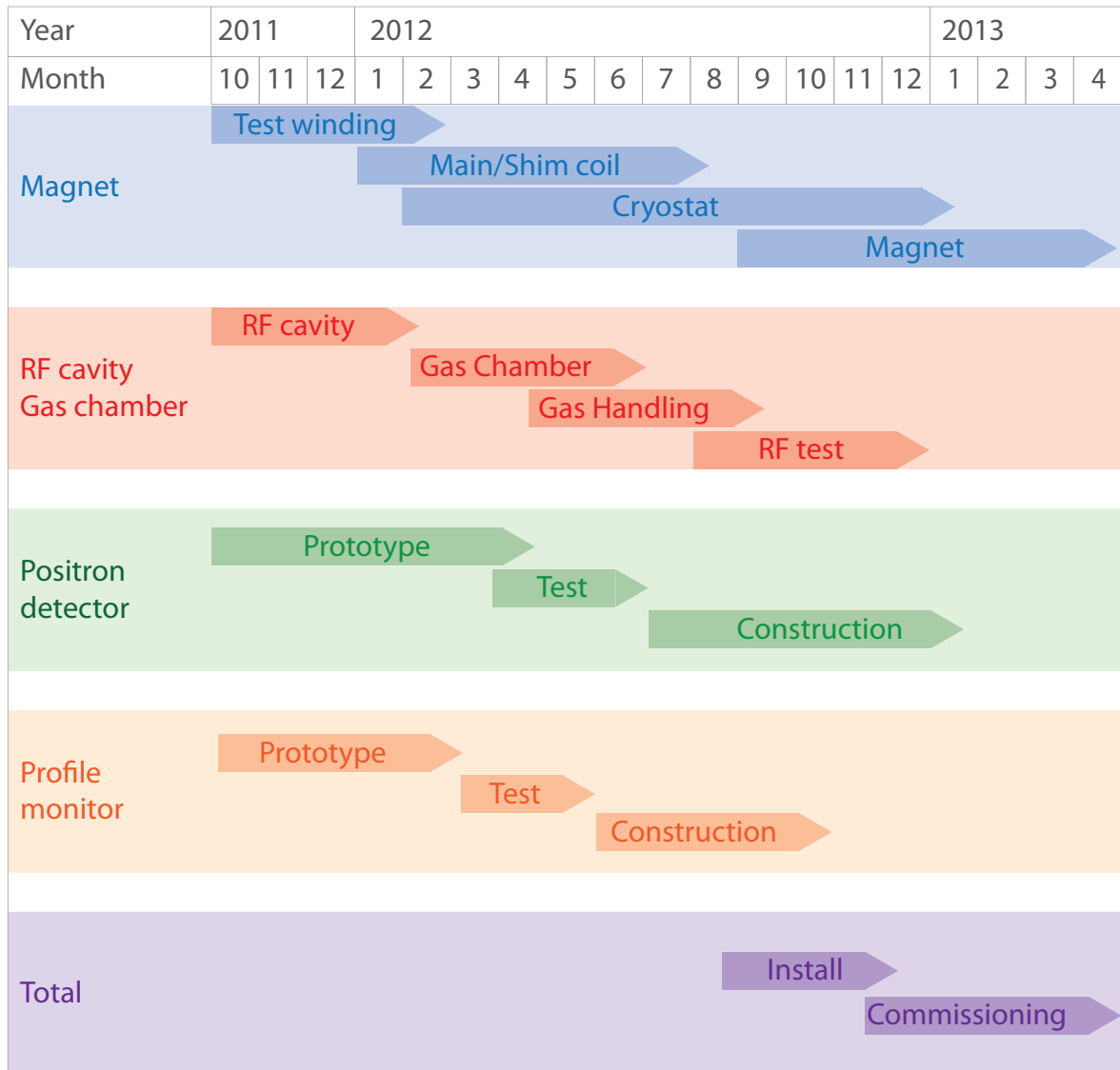


Figure 5.4: A schedule of a preparation of this experiment. we can start this experiment until the end of 2012.

Appendix A

Drawings

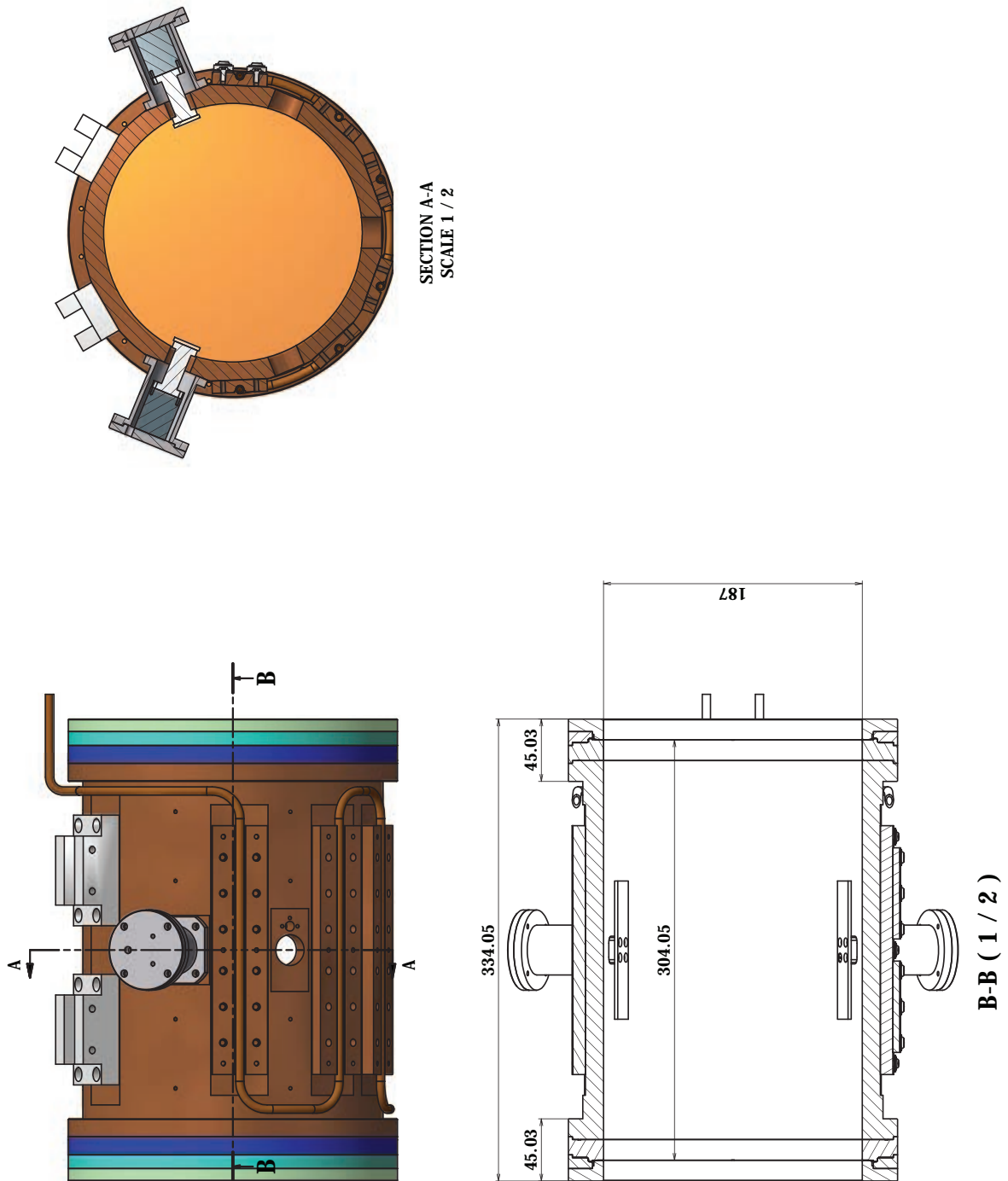


Figure A.1: A drawing of the cavity.

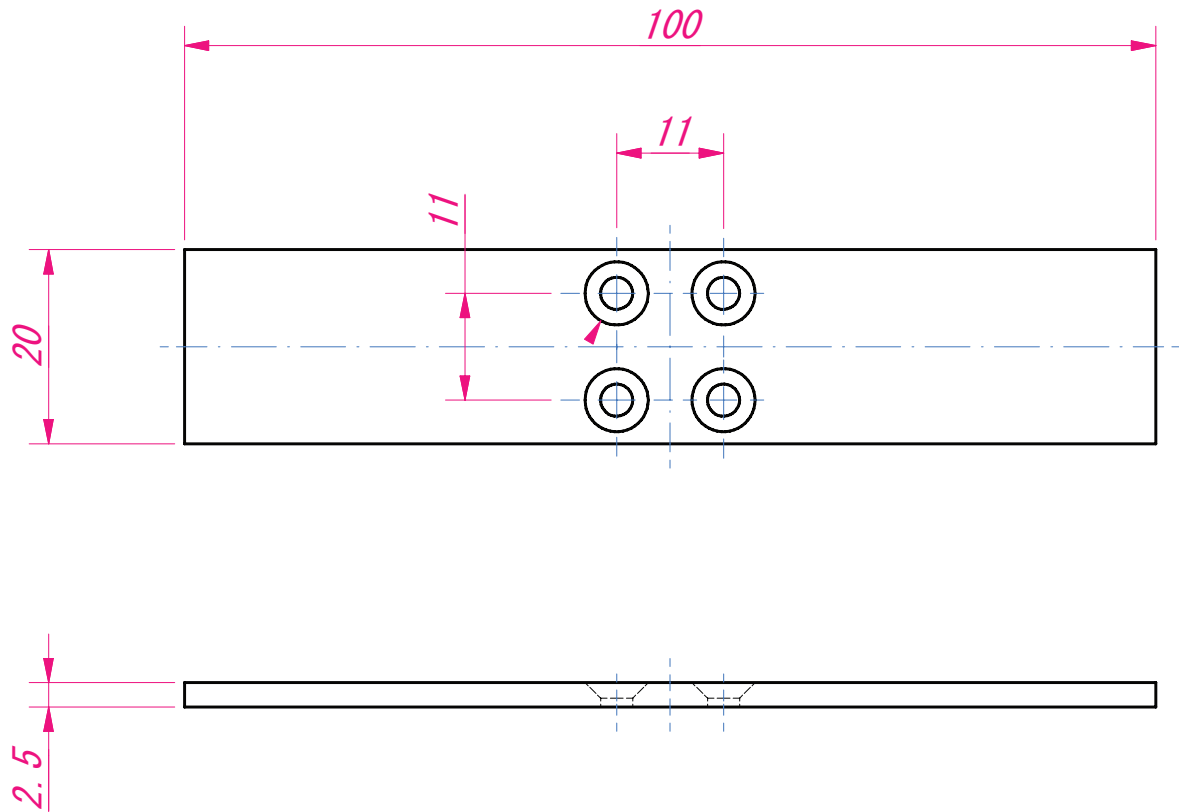


Figure A.2: A drawing of the tuning bar.

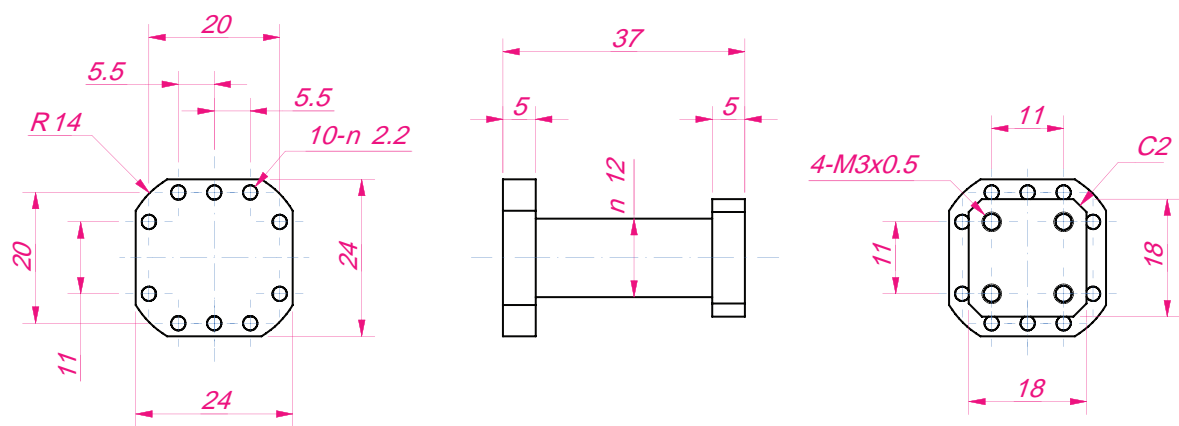


Figure A.3: A drawing of the tuning bar support.

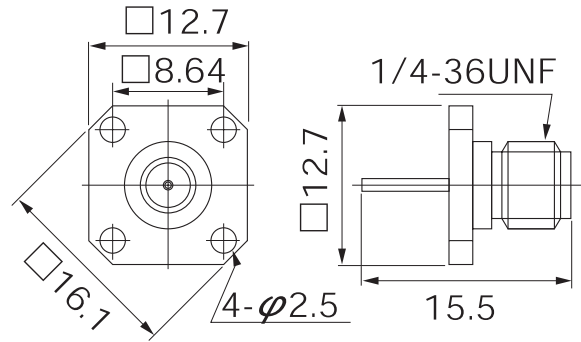


Figure A.6: Adrawing of the SMA connector.

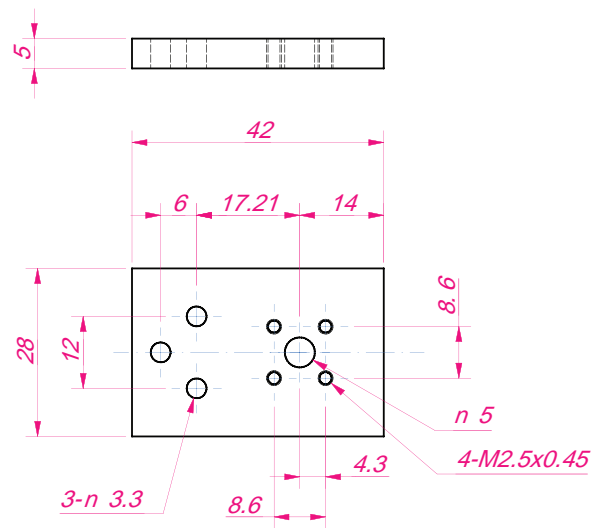


Figure A.7: Adrawing of the SMA support.

Appendix B

Muon beamline

Muonium HFS experiment is planned at J-PARC/MUSE facility. J-PARC consists of a 400 MeV linac, 3 GeV and 50 GeV synchrotron rings, which provide an intense proton beam. A 1 MW proton beam is transported from the 3 GeV synchrotron ring to Material and Life Science Facility (MLF). There are four muon beamlines for several purposes including under construction.

B.1 How to provide a muon beam

A 3 GeV proton beam from the J-PARC Rapid Cycle Synchrotron passes through a carbon target of 2 cm thickness produce pions. Different schemes are known to collect muons (see Figure B.2).

Decay muon

Pions produced at the carbon target which have some energy distribution guided to a large superconducting solenoid magnet. They decay into muons in the magnet. Muon beam is focused and collected again and dedicate to muon beam line.

Surface muon

As is seen in Equation 2.1, one can in principle get a monoenergetic muon from a stopped pion.

Muons which are produced by pions stopped near the surface of the carbon target are collected. Surface muon beam line can provide slow muons of 4 MeV.

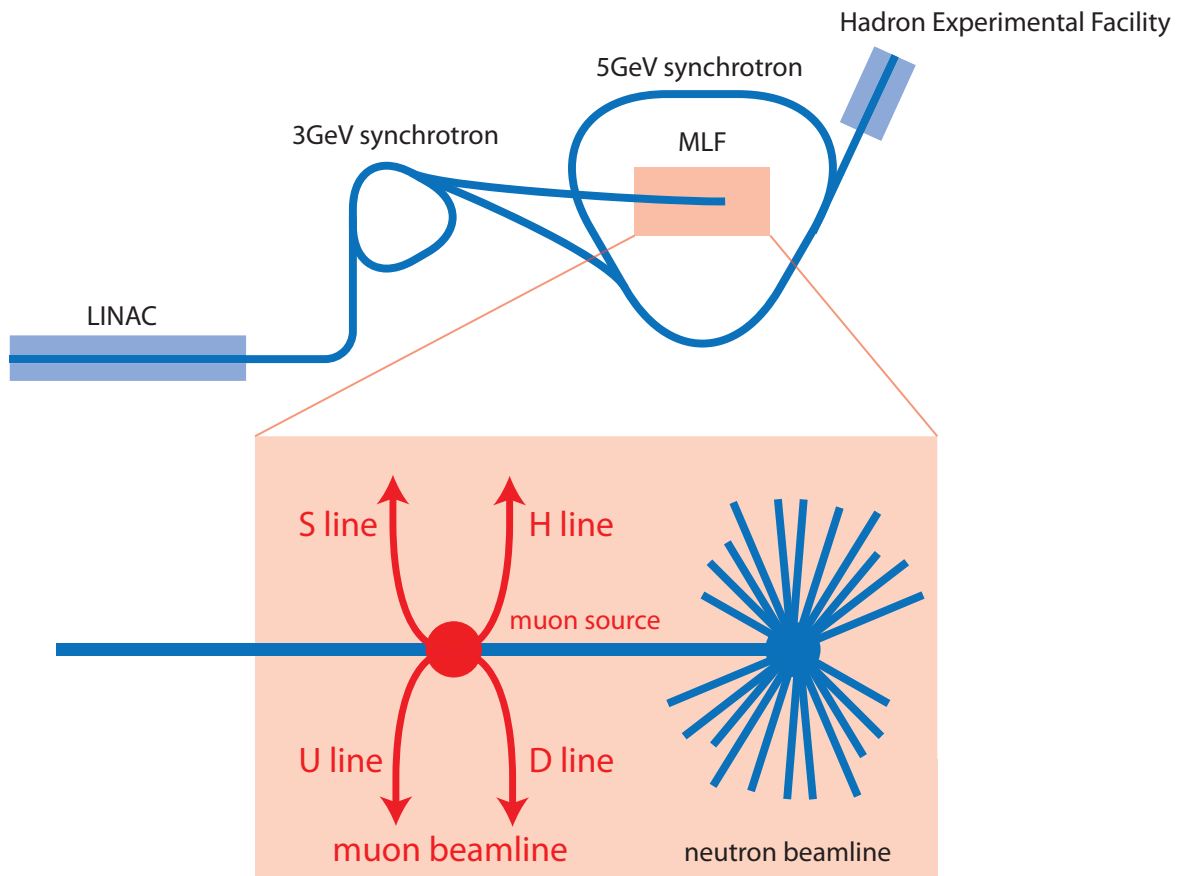


Figure B.1: A drawing of a overview of facilities at J-PARC and muon beamline at MLF. MLF has a four muon beamlines including under constructing.

J-PARC/MLF (Material and Life Science Experimental Facility) has two decay muon beam lines and two surface muon beam lines, some of which are under construction.

Ultra slow muon

Ultra slow muon is a technique of producing cold muon beam ($0 \sim 30$ KeV). The process of producing ultra slow muons is

1. muons stop at rear side of foil,
2. muons diffuse and reach to foil surface,
3. muoniums are formed by electron capture and evaporate,
4. ionize muoniums and produce ultra slow muons.

B.2 Muon beam lines

D line (operating)

Decay/Surface muon beam using a superconducting solenoid beam channel. The intensity of beam is $3 \times 10^7 \mu^+/\text{sec}$.

U line (under construction)

Dedicated beam line to produce Ultra Slow muon ($E = 0.05 \sim 30$ KeV) with high intensity (4×10^8) and high luminosity.

S line (under construction)

Dedicate beam line to extract surface muon for Materials Science. Highest intensity pulsed 4 MeV μ^+ for materials science.

H line (under construction)

High Momentum muon beam line. It is a candidate for g-2.

One of a candidate is the D-line which is the only beam line currently operational. It provides $3 \times 10^7 \mu^+/\text{sec}$ and it enough to outdo the previous experiment. The second candidate is the H-line. In this case the expected surface muon yield is $4 \times 10^8 \mu^+/\text{sec}$. Beam energy is 4 MeV.

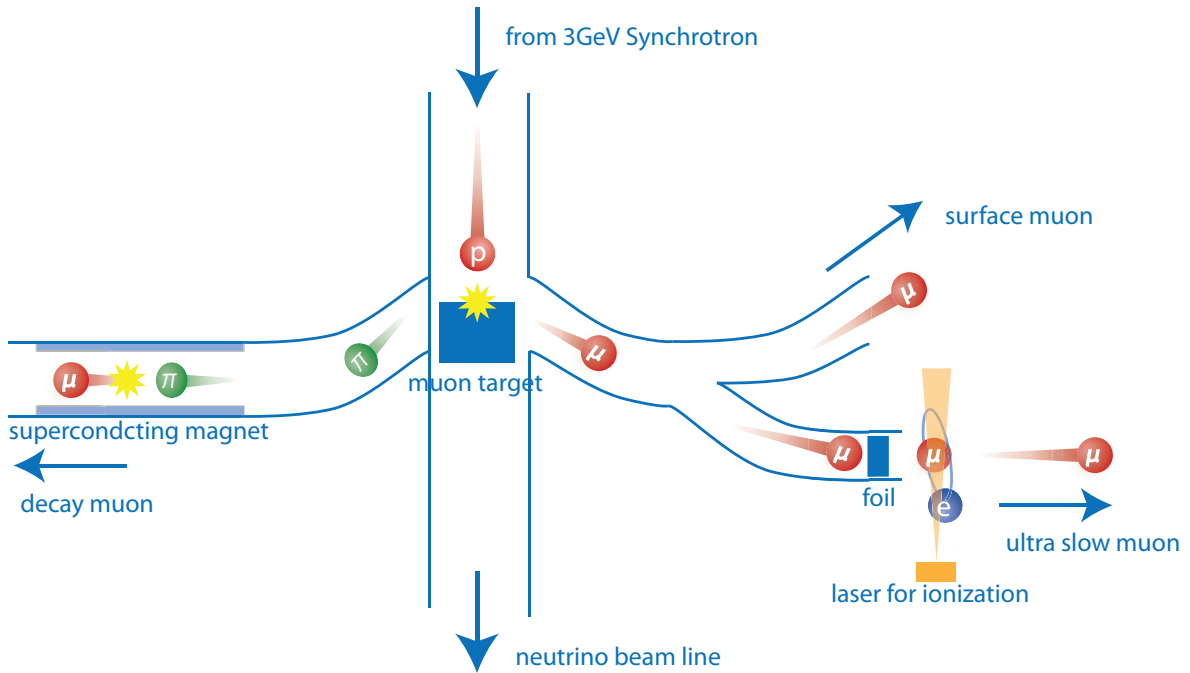


Figure B.2: Schemes of providing muons. Pions produced at the carbon target which have some energy distribution guided to a large superconducting solenoid magnet and decay into muons in the magnet (Decay muon). Collect muons which is produced by pions stopped near the surface of the carbon target (Surface muon). ultra slow muons ($0 \sim 30$ KeV) are produced by a ionization of muonium.

	status	momentum	muon yield
D line	operating	5 ~ 120 MeV/c	3×10^7 /s
U line	under construction	~ 30 MeV/c	4×10^8 /s
		a few eV (Ultra slow)	10^6 /s (Ultra slow)
S line	under construction	~ 30 MeV/c	1×10^7 /s
H line	under construction	30 MeV/c ~ 120MeV/c	1×10^8 /s

Table B.1: Spec of MLF muon beamline

Appendix C

RF fields of the TM110 mode and the TM210 mode

The amplitudes of the microwave electromagnetic field in the cavity are

$$H_r = -H_{110} \frac{J_1(x_{11} \frac{2r}{D})}{x_{11} \frac{2r}{D}} \sin \phi, \quad (\text{C.1})$$

$$H_\phi = -H_{110} J_1'(x_{11} \frac{2r}{D}) \cos \phi, \quad (\text{C.2})$$

$$E_z = E_{110} J_1(x_{11} \frac{2r}{D}) \cos \phi. \quad (\text{C.3})$$

for the TM110 mode and

$$H_{1r} = -H_{210} \frac{2J_2(x_{21} \frac{2r}{D})}{x_{21} \frac{2r}{D}} \sin 2\phi, \quad (\text{C.4})$$

$$H_{1\phi} = -H_{210} J_2'(x_{21} \frac{2r}{D}) \cos 2\phi, \quad (\text{C.5})$$

$$E_z = E_{210} J_2(x_{21} \frac{2r}{D}) \cos 2\phi. \quad (\text{C.6})$$

for the TM210 mode, in which H_{mnp} and E_{mnp} are amplitude, r is the radial coordinate and ϕ is the azimuthal angle measured with respect to the position of the input loop.

The microwave power spatial distribution is proportional to

$$H_1^2(r, \phi) = H_{1r}^2(r, \phi) + H_{1\phi}^2(r, \phi). \quad (\text{C.7})$$

Appendix D

Evaluation of a input RF power

One of the way to obtain a resonance line is counting a number of decay positrons from $t = 0$ to $t = \infty$. We consider muonium formed at $t = 0$. The signal is defined as [6]

$$S = \frac{\Delta N}{N_{\text{OFF}}}. \quad (\text{D.1})$$

$$\Delta N = N_{\text{ON}} - N_{\text{OFF}}. \quad (\text{D.2})$$

where N_{OFF} (N_{ON}) is the number of positrons observed when microwaves off (on). Approximately, the signal is

$$S_{\text{max}} \approx \frac{2|b|^2}{4|b|^2 + \gamma^2}, \quad (\text{D.3})$$

in which $|b|$ is proportional to the amplitude of the magnetic field and γ is muon decay rate. Following D.1, required RF magnetic field for transition is about 0.005 G at muonium formed. Max magnetic field of the TM110 mode is approximately equivalent to this value when RF input power is about 10 W.

Another way to obtain a resonance line is “old muonium” method. we consider the time dependence of the signal observed over time interval t_1 to t_2 . The approximate expression for the line shape which gives in dominant features is

$$S \approx \frac{(2|b|^2)/\Gamma \gamma e^{-\gamma t_1} (1 - \cos \Gamma t_1) \delta t}{e^{-\gamma t_1} - e^{-\gamma t_2}}, \quad (\text{D.4})$$

where

$$\Gamma^2 = (\omega_{12} - \omega)^2 + 4|b|^2. \quad (\text{D.5})$$

ω_{12} is transition frequency of ν_{12} and ω is the microwave frequency. And the denominator in

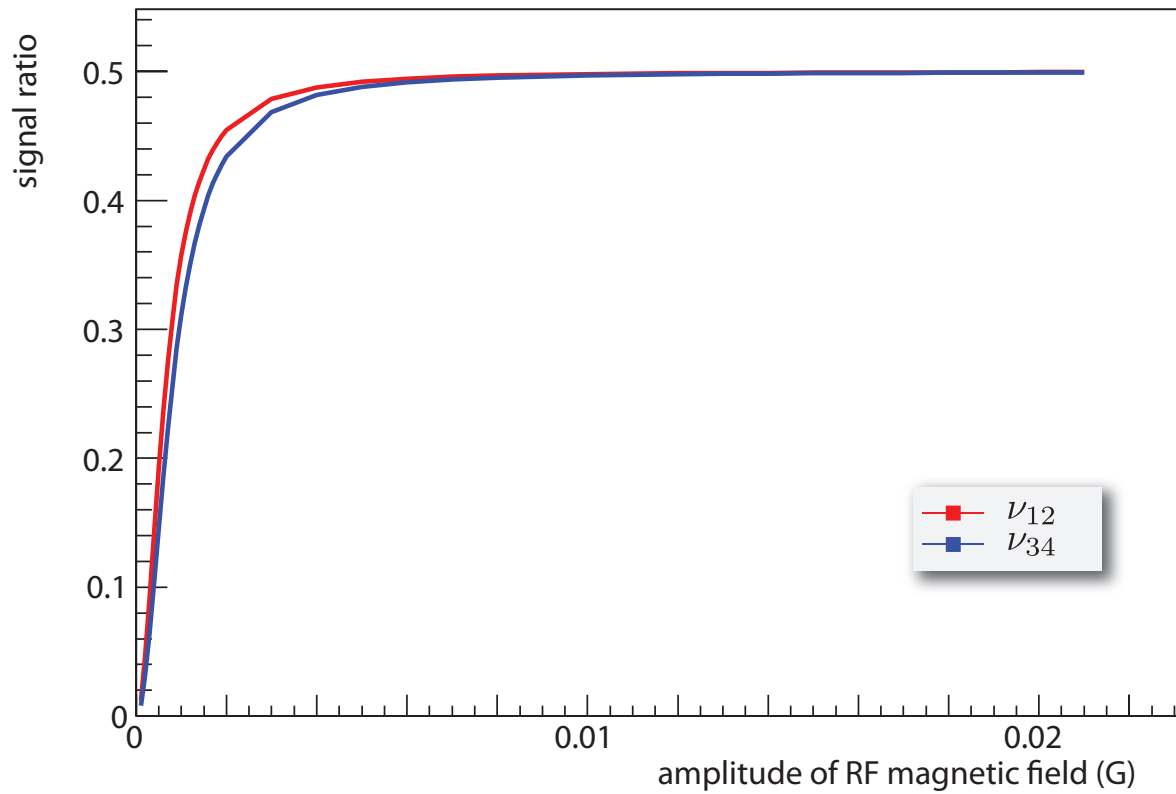


Figure D.1: A relation between signal ratio of microwaves on to off and amplitude of RF magnetic field. The red line represents that of ν_{12} and the blue line represents that of ν_{34} .

equation D.4 is :

$$e^{-\gamma t_1} - e^{-\gamma t_2} \approx \gamma e^{-\gamma t_1} \delta t. \quad (\text{D.6})$$

Then D.4 becomes

$$S \approx 2|b|^2 \frac{1 - \cos \Gamma t_1}{\Gamma^2}. \quad (\text{D.7})$$

Thus maximum of signal ratio is determined by t_1 and maximum of the signal occur in times [6]

$$t_1(\text{max}) = \frac{(n + 1/2)\pi}{|b|}. \quad (\text{D.8})$$

Bibliography

- [1] Peter J. Mohr, Barry N. Taylor, and David B. Newell. Codata recommended values of the fundamental physical constants: 2006. *Journal of Physical and Chemical Reference Data*, 37(3):1187–1284, 2008.
- [2] Kaoru Hagiwara, Ruofan Liao, Alan D. Martin, Daisuke Nomura, and Thomas Teubner. $(g - 2)_\mu$ and $\alpha(m_Z^2)$ re-evaluated using new precise data. *J. Phys.*, G38:085003, 2011.
- [3] V. W. Hughes, M. Grosse Perdekamp, D. Kawall, W. Liu, K. Jungmann, and G. zu Puttlitz. Test of cpt and lorentz invariance from muonium spectroscopy. *Phys. Rev. Lett.*, 87:111804, Aug 2001.
- [4] J. R. Musser, R. Bayes, Yu. I. Davydov, P. Depommier, J. Doornbos, W. Faszer, C. A. Gagliardi, A. Gaponenko, D. R. Gill, P. Green, P. Gumplinger, M. D. Hasinoff, R. S. Henderson, J. Hu, B. Jamieson, P. Kitching, D. D. Koetke, A. A. Krushinsky, Yu. Yu. Lachin, J. A. Macdonald, R. P. MacDonald, G. M. Marshall, E. L. Mathie, L. V. Miasoedov, R. E. Mischke, P. M. Nord, K. Olchanski, A. Olin, R. Openshaw, T. A. Porcelli, J.-M. Poutissou, R. Poutissou, M. A. Quraan, N. L. Rodning, V. Selivanov, G. Sheffer, B. Shin, F. Sobratee, T. D. S. Stanislaus, R. Tacik, V. D. Torokhov, R. E. Tribble, M. A. Vasiliev, and D. H. Wright. Measurement of the michel parameter ρ in muon decay. *Phys. Rev. Lett.*, 94:101805, Mar 2005.
- [5] <http://www.cobham.com/>.
- [6] Weiwen Liu. *HIGH PRECISION MEASUREMENT OF MUONIUM GROUND STATE HYPERFINE INTERVAL AND MUON MAGNETIC MOMENT*. PhD thesis, Yale University, 1997.

- [7] Savely G. and Karshenboim. Precision physics of simple atoms: Qed tests, nuclear structure and fundamental constants. *Physics Reports*, 422(1-2):1 – 63, 2005.
- [8] V.W.Hughes and G.zu Putlitz. *Quantum electrodynamics*. Advanced series on directions in high energy physics. World Scientific, 1990.
- [9] Donald G. Fleming, Randall J. Mikula, and David M. Garner. μ^+ charge exchange and muonium formation in low-pressure gases. *Phys. Rev. A*, 26:2527–2544, Nov 1982.
- [10] R. M. Mobley, J. J. Amato, V. W. Hughes, J. E. Rothberg, and P. A. Thompson. Muonium chemistry ii. *The Journal of Chemical Physics*, 47(8):3074–3075, 1967.
- [11] R. M. Mobley, J. M. Bailey, W. E. Cleland, V. W. Hughes, and J. E. Rothberg. Muonium chemistry. *The Journal of Chemical Physics*, 44(11):4354–4355, 1966.
- [12] Christian G. Parthey, Arthur Matveev, Janis Alnis, Birgitta Bernhardt, Axel Beyer, Ronald Holzwarth, Aliaksei Maistrou, Randolf Pohl, Katharina Predehl, Thomas Udem, Tobias Wilken, Nikolai Kolachevsky, Michel Abgrall, Daniele Rovera, Christophe Salomon, Philippe Laurent, and Theodor W. Hänsch. Improved measurement of the hydrogen $1s\sim 2s$ transition frequency. *Phys. Rev. Lett.*, 107:203001, Nov 2011.
- [13] Helmut Hellwig, Robert F. C. Vessot, Martin W. Levine, Paul W. Zitzewitz, David W. Allan, and David J. Glaze. Measurement of the unperturbed hydrogen hyperfine transition frequency. *Instrumentation and Measurement, IEEE Transactions on*, 19(4):200–209, nov. 1970.
- [14] Norman F. Ramsey. Experiments with trapped hydrogen atoms and neutrons. *Hyperfine Interactions*, 81:97–103, 1993. 10.1007/BF00567253.
- [15] M.I. Eides, H. Grotch, and V.A. Shelyuto. *Theory of light hydrogenic bound states*. Springer tracts in modern physics. Springer, 2007.
- [16] M. W. Ritter, P. O. Egan, V. W. Hughes, and K. A. Woodle. Precision determination of the hyperfine-structure interval in the ground state of positronium. v. *Phys. Rev. A*, 30(3):1331–1338, Sep 1984.
- [17] Bernd A. Kniehl and Alexander A. Penin. Order $\alpha^7 \ln(1/\alpha)$ contribution to positronium hyperfine splitting. *Phys. Rev. Lett.*, 85(24):5094–5097, Dec 2000.

- [18] W Liu, M G Boshier, S Dhawan, O Van Dyck, P Egan, X Fei, M Grosse Perdekamp, V W Hughes, M Janousch, K Jungmann, and et al. High precision measurements of the ground state hyperfine structure interval of muonium and of the muon magnetic moment. *Physical Review Letters*, 82(4):711–714, 1999.
- [19] S G Karshenboim, S I Eidelman, P Fendel, V G Ivanov, N N Kolachevsky, V A Shelyuto, and T W Hansch. Study of hyperfine structure in simple atoms and precision tests of the bound state qed. *Nucl. Phys. B, Proc. Suppl.*, 162(hep-ph/0608236):260–263, Aug 2006.
- [20] V. W. Hughes, D. W. McColm, K. Ziock, and R. Prepost. Formation of muonium and observation of its larmor precession. *Phys. Rev. Lett.*, 5(2):63–65, Jul 1960.
- [21] R. Prepost, V. W. Hughes, and K. Ziock. Observation of the hyperfine structure splitting of muonium by use of a static magnetic field. *Phys. Rev. Lett.*, 6(1):19–21, Jan 1961.
- [22] J. M. Bailey, W. E. Cleland, V. W. Hughes, R. Prepost, and K. Ziock. Muonium. ii. observation of the muonium hyperfine-structure interval. *Phys. Rev. A*, 3(3):871–884, Mar 1971.
- [23] R. D. Ehrlich, H. Hofer, A. Magnon, D. Stowell, R. A. Swanson, and V. L. Telegdi. Determination of the muonium hyperfine splitting at low pressure from a field-independent zeeman transition. *Phys. Rev. Lett.*, 23(10):513–517, Sep 1969.
- [24] W. E. Cleland, J. M. Bailey, M. Eckhause, V. W. Hughes, R. M. Mobley, R. Prepost, and J. E. Rothberg. New value for the fine-structure constant α from muonium hyperfine structure interval. *Phys. Rev. Lett.*, 13(6):202–205, Aug 1964.
- [25] W. E. Cleland, J. M. Bailey, M. Eckhause, V. W. Hughes, R. Prepost, J. E. Rothberg, and R. M. Mobley. Muonium. iii. precision measurement of the muonium hyperfine-structure interval at strong magnetic field. *Phys. Rev. A*, 5(6):2338–2356, Jun 1972.
- [26] V W Hughes. Muonium. *Annual Review of Nuclear Science*, 16(1):445–470, 1966.
- [27] P. A. Thompson, J. J. Amato, P. Crane, V. W. Hughes, R. M. Mobley, G. zu Putlitz, and J. E. Rothberg. Determination of muonium hyperfine structure interval through measurements at low magnetic fields. *Phys. Rev. Lett.*, 22(5):163–167, Feb 1969.

- [28] R. D. Ehrlich, H. Hofer, A. Magnon, D. Y. Stowell, R. A. Swanson, and V. L. Telegdi. Precision experiments on muonium. i. determination of the muonium hyperfine splitting in low-pressure argon from a field-independent zeeman transition. *Phys. Rev. A*, 5(6):2357–2375, Jun 1972.
- [29] R. De Voe, P. M. McIntyre, A. Magnon, D. Y. Stowell, R. A. Swanson, and V. L. Telegdi. Measurement of the muonium hfs splitting and of the muon moment by "double resonance," and a new value of α . *Phys. Rev. Lett.*, 25(26):1779–1783, Dec 1970.
- [30] P. A. Thompson, P. Crane, T. Crane, J. J. Amato, V. W. Hughes, G. zu Putlitz, and J. E. Rothberg. Muonium. iv. precision measurement of the muonium hyperfine-structure interval at weak and very weak magnetic fields. *Phys. Rev. A*, 8(1):86, Jul 1973.
- [31] D. Favart, P. M. McIntyre, D. Y. Stowell, V. L. Telegdi, R. DeVoe, and R. A. Swanson. Quadratic hfs pressure shifts of muonium in argon and krypton. *Phys. Rev. Lett.*, 27(20):1340–1342, Nov 1971.
- [32] H. G. E. Kobrak, R. A. Swanson, D. Favart, W. Kells, A. Magnon, P. M. McIntyre, J. Roehrig, D. Y. Stowell, V. L. Telegdi, and M. Eckhause. A new precision measurement of the muonium hyperfine interval in argon. *Physics Letters B*, 43(6):526 – 528, 1973.
- [33] D. E. Casperson, T. W. Crane, V. W. Hughes, P. A. Souder, R. D. Stambaugh, P. A. Thompson, H. Orth, G. Zu Putlitz, H. F. Kaspar, H. W. Reist, and A. B. Denison. A new high precision measurement of the muonium hyperfine structure interval Δv^1 . *Physics Letters B*, 59:397–400, November 1975.
- [34] D. E. Casperson, T. W. Crane, A. B. Denison, P. O. Egan, V. W. Hughes, F. G. Mariam, H. Orth, H. W. Reist, P. A. Souder, R. D. Stambaugh, P. A. Thompson, and G. zu Putlitz. New precise value for the muon magnetic moment and sensitive test of the theory of the hfs interval in muonium. *Phys. Rev. Lett.*, 38(17):956–959, Apr 1977.
- [35] D. E. Casperson, T. W. Crane, A. B. Denison, P. O. Egan, V. W. Hughes, F. G. Mariam, H. Orth, H. W. Reist, P. A. Souder, R. D. Stambaugh, P. A. Thompson, and G. zu Putlitz. New precise value for the muon magnetic moment and sensitive test of the theory of the hfs interval in muonium. *Phys. Rev. Lett.*, 38(25):1504, Jun 1977.

- [36] F. G. Mariam, W. Beer, P. R. Bolton, P. O. Egan, C. J. Gardner, V. W. Hughes, D. C. Lu, P. A. Souder, H. Orth, J. Vetter, U. Moser, and G. zu Putlitz. Higher precision measurement of the hfs interval of muonium and of the muon magnetic moment. *Phys. Rev. Lett.*, 49(14):993–996, Oct 1982.
- [37] Michael I. Eides. Weak-interaction contributions to hyperfine splitting and lamb shift. *Phys. Rev. A*, 53:2953–2957, May 1996.
- [38] S. G. Karshenboim. Leading logarithmic corrections and uncertainty of muonium hyperfine splitting calculations. *Zeitschrift fur Physik D Atoms, Molecules and Clusters*, 36:11–15, 1996. 10.1007/BF01437414.
- [39] Andrzej Czarnecki, Simon I. Eidelman, and Savely G. Karshenboim. Muonium hyperfine structure and hadronic effects. *Phys. Rev. D*, 65:053004, Jan 2002.
- [40] Robert S. Van Dyck, Paul B. Schwinberg, and Hans G. Dehmelt. New high-precision comparison of electron and positron g factors. *Phys. Rev. Lett.*, 59:26–29, Jul 1987.
- [41] Peter J. Mohr, Barry N. Taylor, and David B. Newell. CODATA recommended values of the fundamental physical constants: 2006. *Rev. Mod. Phys.*, 80:633–730, Jun 2008.
- [42] C. Amsler. Particle data group. *Physics Letters B667, 1 (2008) and 2009 partial update for the 2010 edition*, 2010.
- [43] Klaus P. Jungmann. Past, present and future of muonium, 2004.
- [44] S.G. Karshenboim. *The Hydrogen Atom: Precision Physics of Simple Atomic Systems (Lecture Notes in Physics)*. Springer, 2001.
- [45] A. Badertscher, S. Dhawan, P. O. Egan, V. W. Hughes, D. C. Lu, M. W. Ritter, K. A. Woodle, M. Gladisch, H. Orth, G. zu Putlitz, M. Eckhause, J. Kane, F. G. Mariam, and J. Reidy. Formation of muonium in the $2s$ state and observation of the lamb shift transition. *Phys. Rev. Lett.*, 52:914–917, Mar 1984.
- [46] A. P. Mills, J. Imazato, S. Saitoh, A. Uedono, Y. Kawashima, and K. Nagamine. Generation of thermal muonium in vacuum. *Phys. Rev. Lett.*, 56:1463–1466, Apr 1986.

- [47] A. C. Janissen, G. A. Beer, G. R. Mason, A. Olin, T. M. Huber, A. R. Kunselman, T. Bowen, P. G. Halverson, C. A. Fry, K. R. Kendall, G. M. Marshall, and J. B. Warren. Muonium production from fine silica powder. *Phys. Rev. A*, 42:161–169, Jul 1990.
- [48] V.W. Hughes and C. Wu. *Muon physics*. Number v. 2 in Muon Physics. Academic Press, 1977.
- [49] D.M. Pozar. *Microwave engineering*. J. Wiley, 2005.
- [50] <http://www.cst.com/>.
- [51] WILLIAM HAPPER. Optical pumping. *Rev. Mod. Phys.*, 44:169–249, Apr 1972.
- [52] S. Ray and S. L. Kaufman. Theoretical interpretation of the quadratic hyperfine pressure shift. *Phys. Rev. Lett.*, 29:895–898, Oct 1972.
- [53] D.E. Casperson, T.W. Crane, V.W. Hughes, P.A. Souder, R.D. Stambaugh, P.A. Thompson, H. Orth, G. zu Putlitz, H.F. Kaspar, H.W. Reist, and A.B. Denison. A new high precision measurement of the muonium hyperfine structure interval. *Physics Letters B*, 59(4):397 – 400, 1975.
- [54] <http://www.srim.org/>.
- [55] C. L. Morgan and E. S. Ensberg. Precise hyperfine pressure-shift measurements for hydrogen isotopes in argon. *Phys. Rev. A*, 7:1494–1502, May 1973.
- [56] Industrial platinum resistance thermometers and platinum temperature sensors, 2008.
- [57] O. Kamigaito. Circuit-model representation of external- q calculation. *Phys. Rev. ST Accel. Beams*, 9:062003, Jun 2006.
- [58] M. Niering, R. Holzwarth, J. Reichert, P. Pokasov, Th. Udem, M. Weitz, T. W. Hänsch, P. Lemonde, G. Santarelli, M. Abgrall, P. Laurent, C. Salomon, and A. Clairon. Measurement of the hydrogen $1s$ - $2s$ transition frequency by phase coherent comparison with a microwave cesium fountain clock. *Phys. Rev. Lett.*, 84(24):5496–5499, Jun 2000.
- [59] M. Fischer, N. Kolachevsky, M. Zimmermann, R. Holzwarth, Th. Udem, T. W. Hänsch, M. Abgrall, J. Grünert, I. Maksimovic, S. Bize, H. Marion, F. Pereira Dos Santos, P. Lemonde, G. Santarelli, P. Laurent, A. Clairon, C. Salomon, M. Haas, U. D.

- Jentschura, and C. H. Keitel. New limits on the drift of fundamental constants from laboratory measurements. *Phys. Rev. Lett.*, 92(23):230802, Jun 2004.
- [60] Savely G. Karshenboim. Nuclear structure-dependent radiative corrections to the hydrogen hyperfine splitting. *Physics Letters A*, 225(1-3):97 – 106, 1997.
- [61] Savely Karshenboim. Simple atoms, quantum electrodynamics, and fundamental constants. In *Precision Physics of Simple Atomic Systems*, volume 627 of *Lecture Notes in Physics*, pages 141–162. Springer Berlin / Heidelberg, 2003. 10.1007/978-3-540-45059-7-8.
- [62] Fred Jegerlehner and Andreas Nyffeler. The muon. *Physics Reports*, 477(1-3):1 – 110, 2009.

Acknowledement

2年間の修士課程の中で、お忙しい中様々な機会に相談に乗ってくださった山崎泰規特任教授に感謝致します。本研究テーマの他に CERN における反水素実験等の機会を与えて頂き、貴重な経験となりました。松田恭幸准教授は今回の本研究テーマとなるキャビティ設計という大変魅力的なテーマを与えてくださいました。2年次からのテーマ変更で短い準備期間の中で測定まで行うことができたのも先生のお陰です。高エネルギー加速器研究所の下村浩一郎准教授、豊田晃久助教は予備知識のない私に今回の設計に関わる様々な助言をくださいました。理化学研究所仁科センターの上垣外修一さん、坂本 成彦さん、須田健嗣さんには CST microwave studio を使わせていただき、また今回の測定においてネットワークアナライザ及び実験室をお貸ししていただきました。このようなご支援がなければ今回の測定まで漕ぎつけることができなかったでしょう。研究室の鳥居寛之助教には、普段の研究生活を含めたあらゆる面においてご指導いただき、本論文執筆にあたって貴重な助言を多くいただきました。黒田直史助教には修士1年次の CERN における実験において実験から生活面に関してご指導いただきました。同じく CERN での実験において、榎本嘉範さんにはコイル製作においてあらゆるサポートをしていただき完成させることができました。檜垣浩之准教授、永田祐吾博士、満汐孝治さんには MUSASHI のビームタイムにおいて実験に関わるあらゆることを教えて頂きました。研究室の大塚未来さん、藤居甲基君、高木聡君、田島美里さんには普段の研究生活の中の様々な場面で助けてもらいました。また、東京大学総合文化研究科山崎松田研究室の皆さま、高エネルギー加速器研究所の皆さま、理化学研究所の皆さまの他、多くの人々の助けによってこのように修士論文をまとめることができました。厚くお礼申し上げます。